CRANFIELD UNIVERSITY

Alejandro Valverde López

BENDING-TWIST SHAPE ADAPTATION BY COMPLIANT CHIRAL SPAR DESIGN

SCHOOL OF AEROSPACE, TRANSPORT AND MANUFACTURING

MSc THESIS

CRANFIELD UNIVERSITY

SCHOOL OF AEROSPACE, TRANSPORT AND MANUFACTURING

MSc THESIS

Academic Year 2016-17

Alejandro Valverde López

Bending-twist Shape Adaptation By Compliant Chiral Spar Design

Supervisor: Dr. Simon Prince (Cranfield University)

Prof. Dr. P. Ermanni (ETH Zürich)

August 2017

This thesis is submitted in partial (45%) fulfillment of the requirements for the degree of Master of Science in Aerospace Dynamics

Abstract

This thesis presents a novel purely passive mechanism of twist morphing for application on aerospace structures, such as wings. During certain flight conditions such as gust encountering, the aircraft may experience critical loads that threaten the structural integrity. To counteract this situation, a time-bounded modification of the lift distribution to achieve a reduction in the aerodynamic load is needed. The proposed method aims to control the bending-twist coupling of the wing-box affecting its torsional stiffness. The design of this wing-box incorporates a variable-stiffness adaptive spar implementation. This element is comprised of a lattice of chiral elements that undergo elastic instabilities on its ligaments under certain load, originating a sudden reduction of the shear modulus in the adaptive spar. The modification of the effective shear modulus in this element provokes the wing-box shear center shifting, a consequent modification of the torsional stiffness and, ultimately, a buckling-induced sectional twist in the wing-box. The mechanism therefore consist on a highly nonlinear variation of the wing twist passively triggered by the onset of buckling on the chiral structure. An analytical model of the wing-box is developed to provide information related to the changes in mechanical properties through modifications in shear modulus on the variable-stiffness spar. A fully parametrized computational model of the whole assembly is built to provide insight of the buckling phenomena and the nonlinear twist response of the structure. An extensive analysis of the influence of each of the main parameters in the buckling appearance and evolution, and in final twist response is also presented. Numeric results show that the snap-buckling instabilities indeed provide an effective method of changing the torsional stiffness of a wing-box and therefore affecting the twist and the lift distribution over the wing. Also, results show that parameters such as the wing-box thickness or the ligament eccentricity provide tailorability capabilities over the mechanism activation and the response evolution.

This project was realized within the Laboratory of Composite Materials and Adaptive Structures of the Eidgenössische Technische Hochschule Zürich (Swiss Federal Institute of Technology Zurich), under the supervision of Prof. Dr. P. Ermanni and the advisory of F. Runkel, K. Dominic and U. Fasel.

All research students must complete the details on this form before signing at the bottom. This form must then be attached by the student as a cover sheet to the 9 month, 21 month and final thesis.

Reports submitted without this form as the cover sheet will not be marked.

Student Name	Alejandro Valverde López
MSc Course	MSc in Aerospace Dynamics
Title of Work	Bending-twist Shape Adaptation By Compliant Chiral Spar Design
	MSc Thesis
Due Date	21/08/2017
Cranfield Supervisor	Dr. Simon Prince

Cranfield University defines plagiarism as follows:

Plagiarism is the use, without acknowledgement, of the intellectual work of other people, and the act of representing the ideas or discoveries of others as one's own in any work submitted for assessment or presented for publication. To copy sentences, phrases or even striking expressions without acknowledgement of the source (either by inadequate citation or failure to indicate verbatim quotations) is plagiarism; to paraphrase without acknowledgement is also plagiarism.

I confirm that:

- I understand the above definition of plagiarism
- that the work contained in the attached report is all my own work except where it has been referenced accordingly
- all electronic and hard copy versions of my reports are identical
- I have given the Turnitin output summary of my report to my Supervisor(s)

Signed A Valverde

Date 20/08/2017

Acknowledgments

First of all, I would like to thanks Dr. Simon Prince from Cranfield University for offering himself to remotely supervise this thesis.

Secondly, I would like to thank to Prof. Dr. Paolo Ermanni for the opportunity offered to conduct my master thesis at the Laboratory of Composite Materials and Adaptive Structures at ETH Zürich.

Furthermore, I would like to thank my advisor at ETH Zürich, Falk Runkel, for his kindness and continuous help and support. His inestimable aid put my work into the right path so I could feel proud of it.

Special thanks to Theofanis Tsiantas who provided an enormous help throughout the whole project. His suggestions and support helped me to gain fundamental understanding of the structures mechanics.

Finally, I would like to give my eternal gratitude to my family, for their full and unconditional support throughout all this years of my education.

Contents

List of Figures

List of Tables

Chapter 1

Introduction

Aircraft morphing is a very broad term that can be understood as the modification of the geometry of the aerodynamic surfaces to enhance the performance through the adaptation to the current flight condition. The interest in morphing of aerodynamic surfaces has accompany aerospace history since the beginning. In 1903, the Wright Brothers successfully completed the first heavier-than-air flight when they designed and build a powered aircraft that achieved a controlled and sustained flight. Their design incorporated a mechanism that provided lateral control by manually changing the twist of the wing. Since then, the necessity of enhanced performance and higher airspeed brought the requirement of stiffer wing structures that would provide increased load carrying capabilities and improved protection against aeroelastic instabilities, among other benefits. As a result, research focused on improving the design of structures that did not exploit the elastic capabilities of the materials used.

On conventional transonic airliners, the need to modify the airflow around the airfoil at different flight conditions is achieved through discrete hinged mechanics such as flaps and ailerons. These mechanisms fulfill its mission in a limited range around the design point while, outside this range, they have a negative influence in the aerodynamics. The necessary discontinuities that these elements produce on the surface advance the boundary layer transition point from laminar to turbulent regime and therefore increase the wing aerodynamic parasite drag.

Being able to modify the airflow without discontinuities on the surface would come along with notable reductions in drag and consequently in fuel consumption. Furthermore, these benefits could be applied to diverse flight conditions or flight path alteration requirements. For example, the modification of the wing swept angle as a common practice to obtain an aircraft able to efficiently fly at a wide range of Mach numbers. Another application of wing morphing is the counteracting of the excessive aerodynamic load originated after gust encountering. This is a flight condition under which aircraft experience critical loads that mark the design point for the airframe due to its structural integrity threat. In such a event, an aircraft is flying in turbulent air and a component of the air velocity, normal to the flight path, changes the effective angle of incidence of the aerodynamic surfaces increasing its aerodynamic load. In Figure **??**, the case of an aircraft encountering a vertical gust is shown. Several mechanisms, which usually add structural mass, have been developed to withstand this rare but critical scenarios. Such solutions require a rapid modification of the lift distribution that mitigate the increment in aerodynamic load. In some modern transonic aircraft, after a gust encountering, the ailerons of both wings are deflected in such a way that they reduce the local airfoil chamber, reducing as well the lift generated at the wing tip.

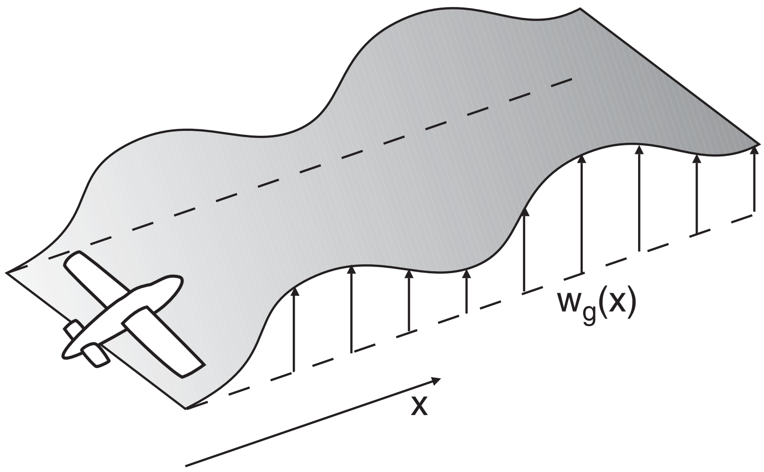

Figure 1.1: Aircraft encountering a vertical gust. [**?**]

For the particular objective of load alleviation, a wing morphing design needs to show compliance with a time bounded response. Having achieved this requirement, the advantages of using such an approach include weight reduction and/or the no alteration of the aerodynamic surfaces continuity with hinges, which provide reduced operation costs and aerodynamic performance enhancement, respectively.

The present work is a proposal of a novel wing morphing technology. Through wing twist modifications, it is possible to reduce the angle of attack and limit the aerodynamic load on the wings. The presented concept consists on a mechanism able to modify the torsional stiffness of the wing-box through the inclusion of a variable-stiffness spar. The modification of the effective shear modulus in this element provokes the wing-box shear center shifting and the consequent modification in wing-box torsional stiffness.

The activation of the adaptive spar is an event fully passive and its based on the appearance of elastic controlled instabilities in the structure of the spar. This element is constituted of a lattice of chiral structures, which consists on a network of interconnected nodes and ligaments. Under certain load, some of the ligaments in the lattice start to buckle eventually causing the collapse of the structure due to the sudden reduction of the shear stiffness in the spar. This event induces a sudden variation in the wing-box twist as its torsional stiffness is altered.

The objectives for the work presented in this thesis include the evaluation of the buckling mechanism as a valid trigger for the variable-stiffness spar adaptation and consequent variation of the wing-box twist. In other words, to show how local buckling can affect the global morphing behavior. Also, the elastic instability or buckling that undergoes in the spar is aimed to be characterized by qualitative means. Finally, the possibility of tailoring the deformation response by varying structure parameters is intended to be evaluated.

This thesis is organized as follows: succeeding this introduction, the state-of-the-art of the technologies related to the one proposed in this work are presented. Then, the wing-box model, developed to investigate the proposed morphing mechanism, is described in the third chapter, following a characterization of its mechanical properties in the subsequent chapter. The fifth chapter shows the results obtained from the simulations performed on the computational model of the wing-box. The conclusion and outlook complete this thesis.

Chapter 2

State-of-the-art

This chapter presents a review of the current technologies in aircraft morphing in general and in wing twist morphing in particular. Also, a focus on the state-of-the-art of the chiral structures applications is presented.

2.1 Morphing aircraft

Aircraft morphing is a technology that has been part of the history of aviation since the Wright Brothers completed the first controlled and sustained flight of a heavier-than-air powered aircraft in 1903. Their concept of aircraft did not provide importance to built-in stability but absolute control of the aircraft by the pilot. For this reason, they deliberatively designed the aircraft with anhedral wing that make it dynamically unstable to perturbations in sideslip but more maneuverable in the lateral direction. In order to achieve roll control, they decided to incorporate a mechanism that allowed the change the wings twist by pulling from cables, as it can be seen in Figure **??**. This was the first ever use of morphing of an aerodynamic surface for aircraft control.

New interest has raised in the recent years in aircraft morphing, mainly due to the appearance of new smart materials that allow more efficient mechanical design and that do not necessarily incur in weight increments [**?**]. Another reason that is pushing forward new aircraft morphing technologies is that missions today are in need of higher aircraft versatility to decrease operational costs in the commercial aviation field. For example, Airbus has recently patented a design of a downwardly foldable wing tip device applicable for a large passenger aircraft [**?**].

A general classification of different wing morphing concepts can be seen in Figure **??**: planform modification through variation of sweep angle, span or chord; out-of-plane alteration involving twist, dihedral angle and spanwise bending, and airfoil adjustment achieved by modifications of the airfoil chamber and/or thickness. Under this classification, the morphing technology that is the focus of the work presented in this thesis is located under the out-of-plane branch and twist modification.

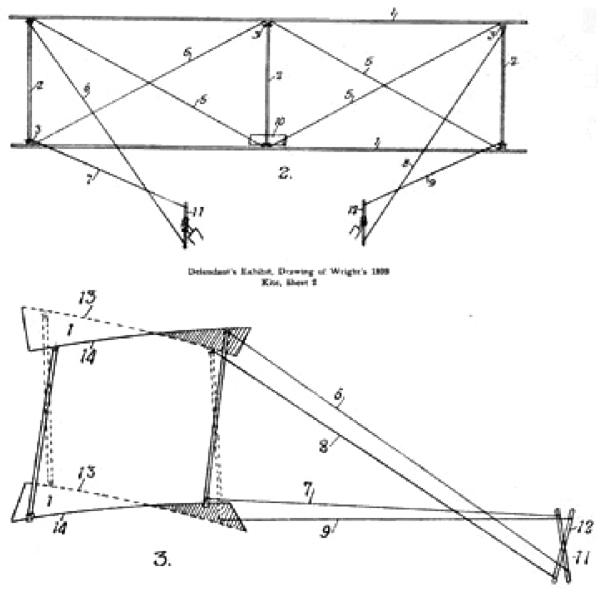

Figure 2.1: Wright Brothers 1899 kite: front and side views, with control sticks. Wing-warping is shown in lower view. [?]

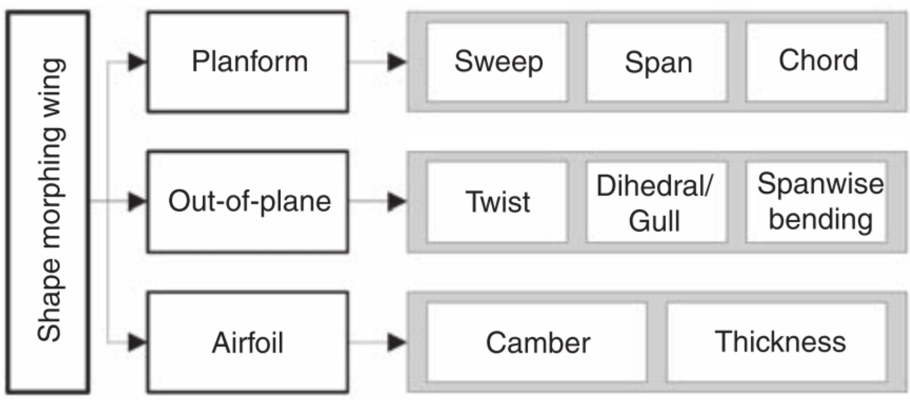

Figure 2.2: Shape morphing wing classification. [?]

In the field of wing morphing through active aeroelastic concepts, the pioneer program of the Active Flexible Wing (AFW) was developed by Rockwell International in the 1980s [?]. Under this program, a design of an aircraft where the wing aeroelastic twist was used to produce the required roll moments for control was presented. This enabled the aircraft to operate at dynamic pressures beyond those where convectional ailerons suffer from the appearance of reversal aeroelastic instabilities. Later, NASA continued with the AFW concept within their Active Aeroelastic Wing (AAW) project which used a modified F-18 fighter named X-53 to perform flight test and assess the viability of the proposed concept. A picture showing this aircraft can be seen in Figure **??**. The X-53 had its wings modified to reduce the torsional stiffness and had additional actuators added to operate the outboard leading-edge flaps separately from the inboard leading-edge surfaces [?]. Rolling moment was obtained by aeroelastic twist of the wing using trailing-edge control surfaces and leading-edge flaps.

Figure 2.3: The X-53 performing a 360° roll to prove AAW technology. [?]

Following those initial attempts, many additional research literature can be found for other approaches to achieve wing morphing. Many of those, consisted in modifying the wing properties by active means, i.e.: incorporating actuators that introduce energy into the system. Among the vast available literature in this field, it is worth mentioning the advances made in [?] to develop a variable stiffness spar (VSS) concept to control the torsional stiffness as a function of the Mach number and the altitude. Also, in the investigation presented in [?], the adaptive torsional stiffness for a vertical tail was achieved by means of a variable attachment point position. The work presented in [?] showed how roll control of a small aircraft could be achieved by actively twisting its flexible wing. The technology of the shape memory alloys (SMA) has been also exploit in the field of active wing twist morphing, as seen in [?] and [?].

However, wing twist morphing designs may also benefit from geometrically flexible structures if the aeroelastic energy from the airstream can be used to activate the shape changing mechanics. Such an approach may lead to passive morphings strategies that are always preferred since no additional energy is necessary to be introduced into the system and the usual weight penalties of morphing may be avoided if no additional actuators are needed.

In [**?**], a passively triggered system to reduce the lift increment that follows a gust encounter using multi-stable elements that are embedded into the airfoil is presented. Other examples of wing twist morphing by passive means are those presented in [**?**], [**?**] and [**?**]. In particular, the technology proposed in these works exploits the capabilities of the chiral structures that feature a negative Poisson's ratio for in-plane strains. A network of these chiral structure is embedded in the rib of the airfoil constituting the deformable part. These chiral structures will be extensively discussed in the next section of the present state-of-the-art review.

Also in the field of passive approaches to achieve wing twist morphing, W. Raither proposed in [**?**] a novel concept of adaptive aeroelastic tailoring by means of wing-box torsional stiffness modification. In order to achieve this, the shear stiffness of one of the webs that conform the wing-box beam is modified. This induces the section shear centre shifting, which provides an additional torsional deformation for a constant load. This concept is later explained in Section **??**, as the same working principle is used for the technology presented in this work.

Implementation of the principle proposed by W. Raither in [**?**], requires a material with controllable in-plane shear modulus. A possible solution is proposed in [**?**] and consisted in the use of electro-bonded laminates that vary its bending stiffness by means of electrostatic forces applied different at points of the structure. Another approach is presented in [**?**], and exploits the variable elastic modulus of a polymer web due to temperature changes. This characteristic is provided by the temperature dependence of the elastic modulus of polymers in proximity of their glass transition. Therefore, the proposed concept consists on a semi-passive approach since some energy needs to be spent for the activation of the adaptive interfaces. In [**?**] the demonstrator shown in Figure **??** was built to show the viability of this last technology.

Finally, in [**?**] the variation of in-plane shear modulus is proposed that can be achieved by inducing elastic instabilities in one of the webs of the wing-box. The component is manufactured with a particular material anisotropy utilizing unidirectional CFRP. The appearance of plate buckling at the root on the specially designed web, as shown in Figure **??**, induces the shear centre location shifting and the torsional stiffness adaptation, thus leading to a purely passive bending-twist coupling. In [**?**], the mechanical response was investigated using FE simulations and experimental testing on a manufactured demonstrator of the concept.

Figure 2.4: Inner structure of the experimental wing build to test the concept of adaptive wing-box. [**?**]

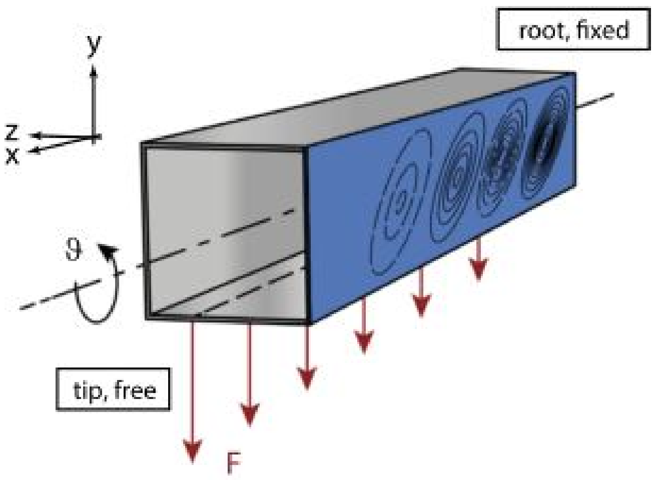

Figure 2.5: Plate bucking on one of the webs of the wing-box beam. The drawing shows a qualitative view of the buckling field. [**?**]

2.2 Compliant chiral structure

As mentioned in the introduction to this thesis, the proposed technology exploits structures that have recently been of used in various research works due to its capabilities as materials with negative Poisson's ratio. Such structures expand laterally when stretched and contract laterally when compressed. In [**?**], R. Lakes proposed that negative Poisson's ratios can result from a hexagonal microstructure of rotable nodes and bendable ligaments such as the one shown in Figure **??**. Such structures are known as non-centrosymmetric, hemitropic, or chiral; they are distinguishable from their mirror image; that is, they cannot be superposed onto them and they are not isotropic.

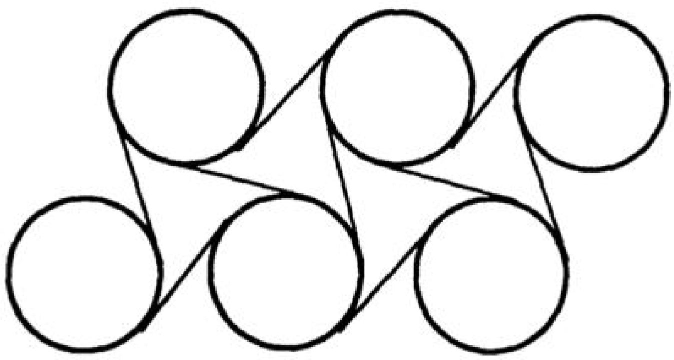

Figure 2.6: Chiral (noncentrosymmetric) hexagonal microstructure of rotable nodes and bendable ligaments. Poisson's ratio is negative. [**?**]

In [**?**], experimental results showed that a honeycomb chiral structure exhibited a Poisson's ratio of -1 for deformations in-plane. Indeed, this behavior was maintained over a significant range of strain, as shown in Figure **??**, verifying that its Poisson's ratio is independent upon the strain, in agreement with theory.

In [**?**] the properties of a chiral honeycomb are investigated, a manufacturing process using composite materials is proposed and the increase in the performance of using such materials is shown. Also, the experiments carried out allowed to characterize the possible failure modes of these structures and the nonlinear response when large displacements occur.

Until that moment, most of the work was concentrated in studying the in-plane behavior of the chiral structures. Then, in [**?**] the flatwise compression behavior of the chiral structures is investigated through FE modeling and simply analytical relations. This is the first consideration of buckling in a chiral structure in some way, in this case it was the out-of-plane buckling behavior based on the similar works presented in [**?**] and [**?**] for honeycomb structures. This research was extended by experimental studies in [**?**] and an anelastic characterization of the buckling phenomena is presented in [**?**]. The buckling response of chiral honeycombs under a general macroscopic in-plane stress state was more recently investigated from a theoretical point of view in [**?**].

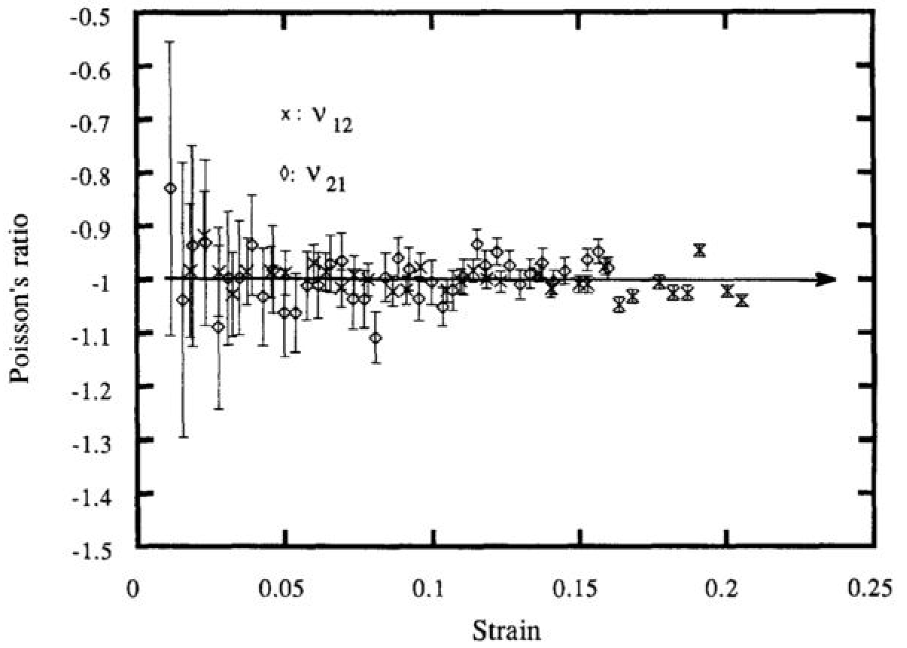

Figure 2.7: Experimental Poisson's ratio ν as a function of axial compressive strain on a chiral honeycomb. The error bars represent inaccuracies due to the measurement resolution. [**?**]

Within the research undertaken at the Laboratory for Composite Materials and Adaptive Structures (CMAS) of the ETH Zürich in the field of variable stiffness structures, a novel chiral topology has recently been proposed. The chiral unit cell is modified by introducing transverse curvature into the ligaments, as shown in Figure **??**. Such design increases the bending stiffness of the ligament and thus of the entire periodic structure. Each ligament posses double eccentricity which changes orientation at the centerline of it, in compliance with an equivalent connection with the cylinders located at the extremes. In [**?**], preliminary investigations of such structures were experimentally conducted on a conceptual level for a basic triangular chiral structure, as shown in Figure **??**.

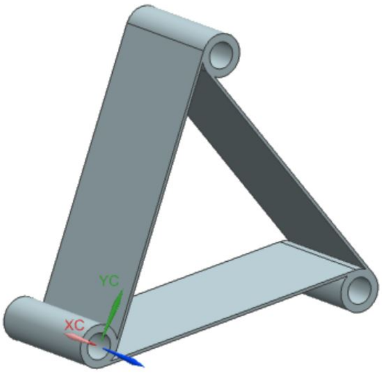

(a) Flat ligaments.

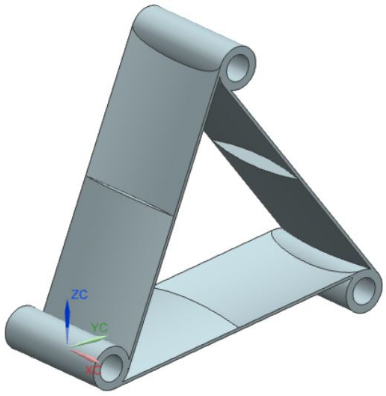

(b) Curved ligaments.

Figure 2.8: Chiral cell elements showing different ligaments curvatures. [**?**]

This new design of the ligaments is expected to provide additional tailorability over the buckling phenomena occurring on the lattice ligaments. This configuration is the one chosen for the chiral structure that is used in the concept presented in this work.

Different approaches has been followed to exploit the particular characteristics of chiral structures under in-plane strain on aerodynamic elements such as airfoils. In [**?**], a truss-core configuration with chiral topology, identical to the one shown in Figure **??**(a), was utilized to design an airfoil for automotive competitions. The concept exploits the elastic deformation of the chiral lattice to alter the airfoil mean chamber line and thus modify the pressure distribution as required for the current desired performance of the car. In [**?**], a similar configuration was investigated by weakly coupled structural and CFD models, and the local and global deformations were characterized by considerations of the macroscopic chiral configuration. A prototype of the proposed design, shown in Figure **??**, was manufactured and tested in [**?**]. Results showed a remarkable tailoring of the chamber morphing performance by means of a limited number of parameters which define the core geometry. The dynamic properties of such chiral truss-core assemblies were investigated in [**?**].

Recently, A. Airoldi developed the "chiral sail" concept in [**?**] which exploits the chiral topology of a chiral network embedded into the airfoil rib. The pressure difference between the upper and lower parts of the airfoil promotes the chamber variation as shown in Figure **??** and amplifies the lift when the angle

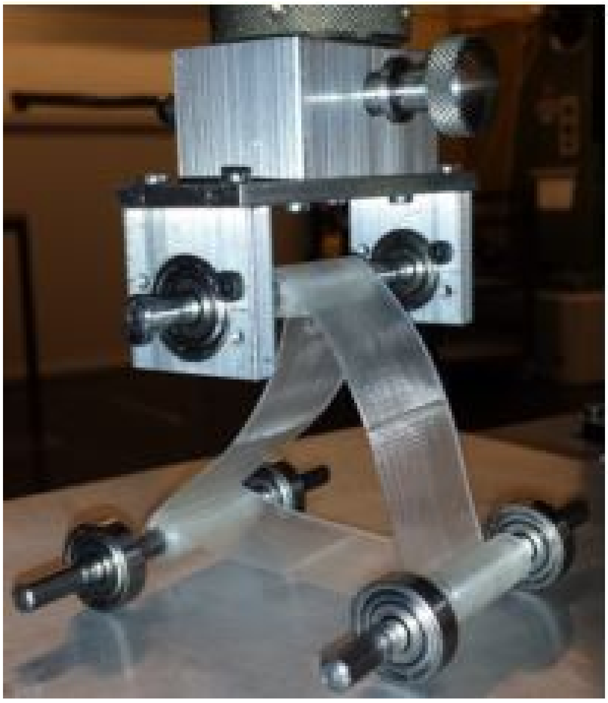

Figure 2.9: Compression load test on a basic triangular chiral structure. [**?**]

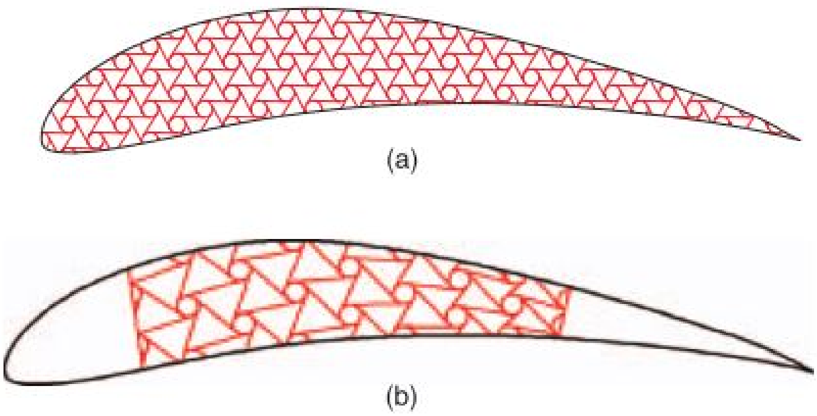

Figure 2.10: Investigated configurations for the truss-core of chiral topology. [**?**]

Figure 2.11: Manufactured prototype of a truss-core airfoil with chiral topology. They were manufacture in aluminum, using water-jet cutting techniques. [**?**]

of attack increases. This concept was implemented and validated by testing a demonstrator in [**?**]. The experimental side of this work showed the difficulties of manufacturing such complex structures.

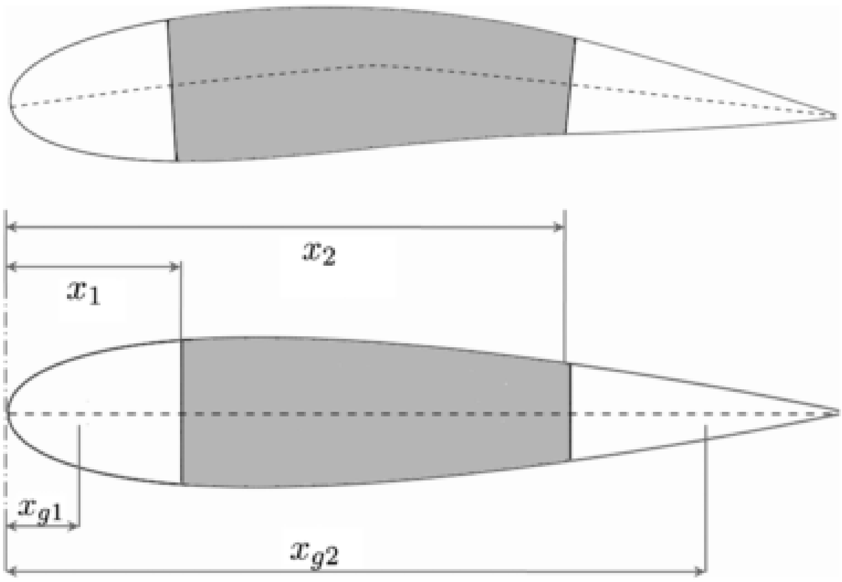

Figure 2.12: Chiral sail concept. The rib of the airfoil is constituted of a network of chiral unit cells. [**?**]

2.3 Rationale for the thesis

This thesis is part of the current research that it is been carried out at CMAS in seek of wing twist morphing achieved through variable stiffness wing-box structures that acquire this property undergoing elastic instabilities.

As shown in the topic review presented in [**?**] and [**?**], the use of buckling-induced technologies is a promising technique to achieve the desired behavior in recent developments of smart structures. Traditionally, elastic instabilities were avoided in the structural designs due to the significant loss of load-carrying capacity and the large deformations occurring as a consequence of such an event. However, in the scope of the so called motion-related applications of buckling-induced technologies, the capability of small perturbations to generate sudden snapping behavior in elastic elements, enables the structure to dynamically change its configuration, being this beneficial for applications such the one considered in the present work. Also, the possibility of minimizing the actuation force required during shape recovery due to the elastic state of the structure becomes interesting.

In parallel, when it comes to the bending-twist shape adaptation by compliant structural designs, some of the solutions already introduced in this chapter are able to modify the wing-box torsional stiffness for a pre-defined shape variation or are optimized for a given actuation lay-out, whereas the adoption of a structural concept such as a chiral lattice offers a wide range of possibilities in terms of tailoring. In particular, the chiral structures that posses curved ligaments are the design option for the concept proposed in this work. This novel characteristic is expected to provide additional control over the buckling appearance and evolution. This design of chiral structure was already manufactured and tested in another project completed at CMAS [**?**].

Thereby, for the approach presented in this work, the working principle introduced by [**?**] is combined with the buckling capabilities of the chiral structures exposed in Section **??** to conform the proposed principle.

In the scope of this thesis, a full model of the whole wing-box with the compliant variable-stiffness spar is studied. It is the intention to look at the buckling characteristics of the lattice of chiral structures that conforms the spar and the response in twist of the whole assembly. It is expected to see buckling occurring at the same time on several ligaments located close to the root of the wing-box since this is the region that experiences higher shear strain when imposing a force at the tip in the transversal plane. Also, it is envisioned that the buckling phenomena activates a sudden change in the twist of the wing-box. Finally, the modification of internal parameters of the chiral structure is expected to show promising tailorability capabilities on the displacement-force curve.

It is expected that the proposed technology is suitable for environments where a rapid shape adaptation is required. Such applications may include to increase the critical speed for load alleviation purposes.

In order to achieve verification of the previous premises, two models of the wing-box are developed, one numerical and another one analytical. The evolution of the buckling phenomena in the structure is characterized and the effect of the different design parameters on the structure pre-buckling and post-buckling response is assessed. The aim is to provided a suitable computational environment to achieve in-deep understanding of the proposed working principle and assist the manufacture of a future demonstrator.

Chapter 3

Wing-box model

A model of the whole wing-box including the variable-stiffness spar is developed to study the buckling characteristics of the chiral lattice, the response in twist of wing-box and the tailorability possibilities of that response. In the present chapter the model is presented, which in fact consists in two models one analytical and another one computational.

On first place, the working principle that lays under the proposed technology is presented. Next, the two different models developed to provide fully understanding of the structure response are presented. Firstly, a simple analytical model of a beam with a web featuring variable stiffness properties is presented. This is used to provide fast insight of the role of each of the design parameters on the final mechanical properties of the beam. Important relevance is given to the section's shear centre y_{SC} shifting. This variable determines the magnitude of the resulting torsional moment that acts on the beam as a result of a load applied on the beam's transversal plane, and that induces the beam twist.

Secondly, the computational model is introduced. The different constituting elements are explained together with the boundary conditions, loads and mesh that are used in the simulations.

Finally, the program used to carry out automatic parametric studies is presented, together with its methodology.

3.1 Concept

As it was already introduced in last chapter, the proposed technology to achieve twist morphing through a variable torsional stiffness wing-box is based on the working principle presented in [**?**] and exploits the buckling characteristics of a lattice of chiral ligaments as a way of varying the effective shear modulus G_{eff} of the adaptive spar of the wing-box.

The basic working principle can be understood considering a closed profile adaptive beam in which the shear centre is shifted as a result of the variable-stiffness capability of one of the webs. An schematic view of the working principle is shown in Figure **??** where an adaptive beam is displayed. In Figure **??**(a), the four webs that constitute the rectangular profile of the beam have the same shear stiffness $G_1t_1 = G_2t_2$. The double symmetry characteristic of such a configuration indicates that the shear centre is located at the point where the two symmetry axes intersect. For this case, under a load applied on the shear centre, the beam experiences bending deformation with zero twist. On the other hand, when considering the situation shown in Figure **??**(b) where $G_1t_1 > G_2t_2$, the reduced shear stiffness of the adaptive web produces that shear centre moves along the y direction and towards positive values of y. In this case, if the load is maintained in the same application point as before, the beam experiences bending deformation and negative twist. Correspondingly, for the case shown in Figure **??**(c) where $G_1t_1 < G_2t_2$, the shifting of the shear centre is towards negative values of y and the beam experiences a positive twisting under the prescribed load.

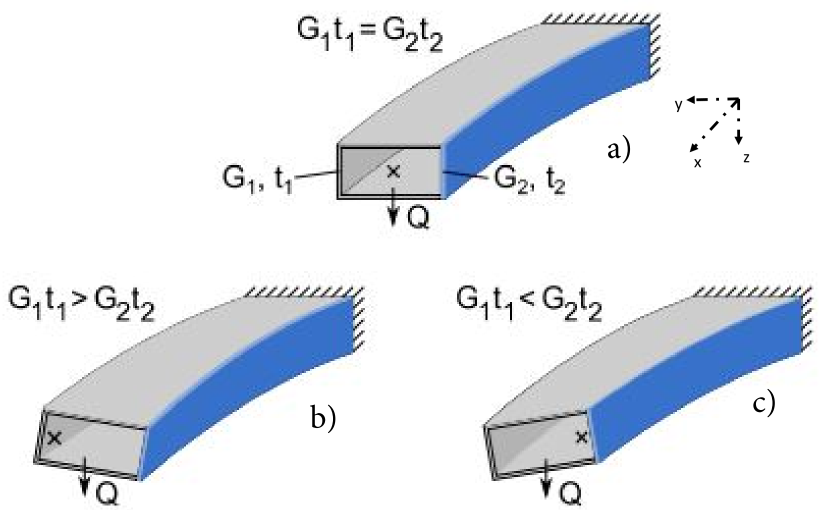

Figure 3.1: Working principle for the adaptive beam. [**?**]

The bending-twist coupling of the beam can therefore be controlled by the variable-stiffness web. The properties of the web can be modified by either adjusting the shear modulus G_2 or the thickness t_2 of the adaptive web.

In the technology presented in this work, the adaptive web is constituted of a lattice of chiral structures. On these elements, elastic buckling is intentionally induced and the resulting consequence is the reduction of the overall shear modulus G_2 effectively introducing an effective shear modulus $G_{2,\text{eff}} < G_1$. An example of the chiral structure undergoing buckling instabilities on some of the ligaments located at the wing-box root can be seen in Figure **??**.

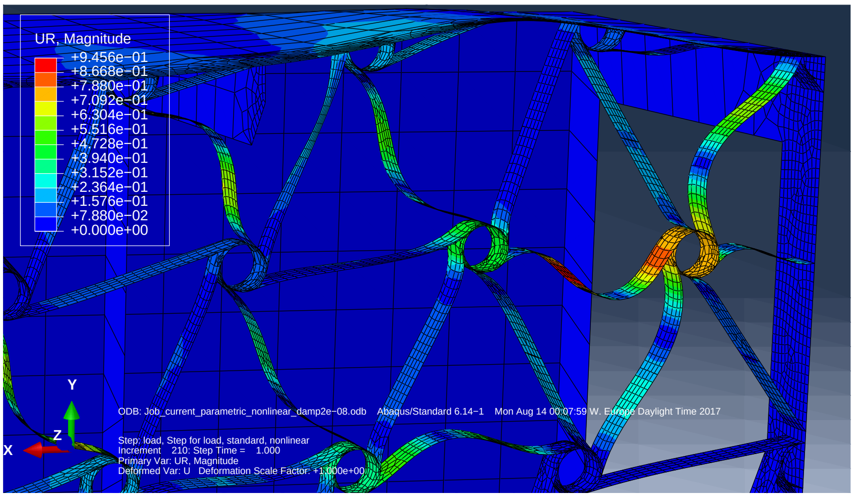

Figure 3.2: Set of chiral ligaments undergoing elastic instabilities at the root of the wing-box.

3.2 Analytical model

The analytical model of the wing-box is described in the present section. An schematic view of the section of the beam can be seen in Figure **??**. The main dimensions for the section are given by the height H and the width B. Such a structure is characterized by having three elements with identical thickness t_1, shear modulus G_1 and Young's modulus E_1. For the element on the right, the adaptive web, the same parameters are t_2, G_2 and E_2, respectively.

As explained in Section **??**, the shear stiffness $G_2 t_2$ of the adaptive web can be modified by varying either thickness t_2 or shear modulus G_2. For the remaining, it is assumed that $t_1 = t_2 = t$ and therefore the thickness t_2 is not be considered as a modifiable parameter on the adaptive web.

Now, the bending-twisting coupling of the structure is investigated using well-known equations to describe the elastic behavior of thin-wall beam elements. Based on the analytical approach to the problem of a beam bending-twisting coupling followed in [**?**], it is known that warping can be neglected for a configuration like the one presented in this section.

The bending displacement of the structure is therefore given by Equation **??**, which a solution of the Bernoulli-Euler equation for a beam:

$$w_b = \frac{QL^3}{6\Phi_y}\left(-\frac{x^3}{L^3} + \frac{3x^2}{L^2}\right), \tag{3.1}$$

where w_b is the displacement along the z direction and Φ_y is the flexural stiffness which is given by Equation **??**:

$$\Phi_y = \int\int E(y,z) z^2 \mathrm{d}y\mathrm{d}z. \tag{3.2}$$

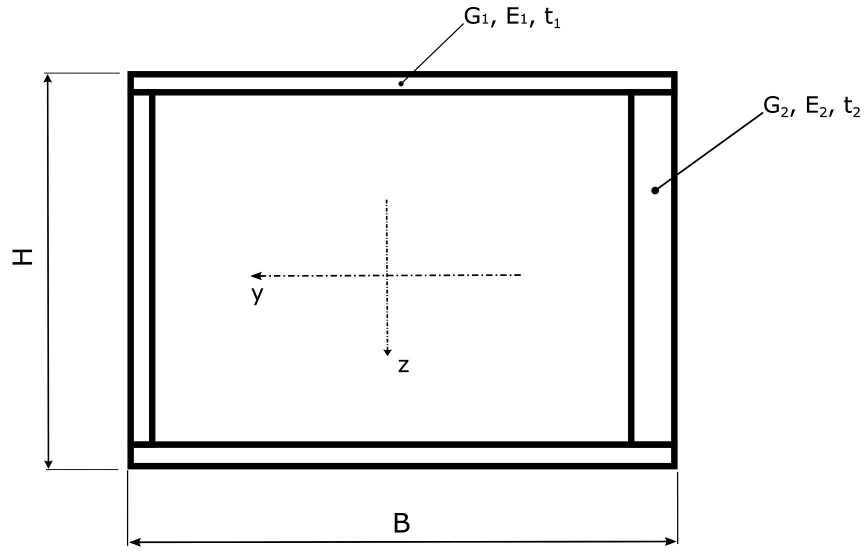

Figure 3.3: Schematic view of the beam closed section. The dimensions are given by the width B and the height H. For the upper, lower and left elements, the wall thickness, shear modulus and the Young's modulus are given by t_1, G_1 and E_1, respectively. For the right element, the same parameters are given by t_2, G_2 and E_2.

On the other hand, the twist of a beam with closed section can be obtained from the St. Venant expression for the specific twist ϑ, which is shown in Equation **??**:

$$\vartheta = \frac{\mathrm{d}\phi}{\mathrm{d}x} = \frac{M_t}{4A_0^2} \oint \frac{\mathrm{d}s}{Gt}, \tag{3.3}$$

where A_0 represent the area enclosed by the profile's wall midline, ϕ is the twist of the beam and M_t is the torsional moment applied. Additionally, the torsional stiffness GI_t for the closed section under study is given by the Equation **??**:

$$GI_t = \frac{4A_0^2}{\oint \frac{\mathrm{d}s}{G(s)t(s)}}. \tag{3.4}$$

In order to calculate the specific twist ϑ , it is necessary to evaluate the shear centre position y_{SC} for a given configuration. In order to achieve this, the calculation of the shear flow distribution in the section also needs to be done. To obtain the shear flow $q(s)$, the profile can be considered to be cut at one point, resulting on a opened section. The shear flow $q_{||}(s)$ for this open section case can be calculated using Equation **??**. The corresponding shear flow for a closed section q_{C} can be obtained using the Equation **??**:

$$q_{||}(s) = -\frac{Q_z}{\Phi_y} S_{E_y}(s), \tag{3.5}$$

$$q_{\mathrm{C}}(s) = q_{||}(s) + q_0, \tag{3.6}$$

where Q_z is the force applied in the z direction and S_{E_y} is the so called static moment or first moment of area, which is calculated through the integral shown in Equation **??**. Also, the variable q_0 represents the shear flow at the boundary that results from the torsion of the beam and can be calculated using the Equation **??**:

$$S_{E_y}(s) = \int_0^s E(s)t(s)z(s)\mathrm{d}s, \tag{3.7}$$

$$q_0 = \frac{Q_z}{\Phi_y} \frac{\oint_s \frac{S_{E_y}(s)}{G(s)t(s)}\mathrm{d}s}{\oint_s \frac{1}{G(s)t(s)}\mathrm{d}s}. \tag{3.8}$$

Now, the shear centre position in the beam transversal section is calculated for the case of open section. Given that the beam mechanical properties and geometrical dimensions are symmetric around y axis, the shear centre position in the z axis is $z_{\mathrm{SC}} = 0$. On the other hand, the shear centre position in the y axis is given by the Equation **??**:

$$y_{\mathrm{SC,open}} = \frac{1}{Q_z} \oint_s q_{\mathrm{C}}(s)r(s)\mathrm{d}s, \tag{3.9}$$

where r represents the perpendicular distance to the coordinate origin.

Now, it is necessary that equilibrium exists between the torsional moment due to the shift of the shear centre (caused during the opening of the profile) and the moment due to the torsional shear flow of the closed profile. This condition can be mathematically expressed through Equation **??**:

$$\begin{aligned} M_{\mathrm{t}} &= Q_{\mathrm{z}}(y_{\mathrm{SC,open}} - y_{\mathrm{SC,closed}}) \\ &= 2A_0 q_0. \end{aligned} \tag{3.10}$$

The above equality enables on one hand the calculation of the closed section shear centre position $y_{\mathrm{SC,closed}}$ using Equation **??**:

$$y_{\mathrm{SC,closed}} = y_{\mathrm{SC,open}} - \frac{2q_0 A0}{Q_z}, \tag{3.11}$$

and the the calculation of the torsional moment M_t acting on the beam on the other hand using Equation **??**:

$$M_t = Q_z(y_{\mathrm{load}} - y_{\mathrm{SC,closed}}), \tag{3.12}$$

that considers the coordinate y_{load} of the point where the load is applied.

Finally, once the torsional moment M_t acting on the beam is known, it is possible to calculate the beam twist $\phi(x)$ using Equation **??** and considering that $\phi(x) = \vartheta x$.

3.3 Computational model

The computational model of the wing box is built using Abaqus CAE commercial software. It consists on three main elements: the wing-box with C-profile, the lattice constituted of the chiral elements and a set of ribs. A general overview of the assembly of the different parts can be seen in Figure **??**.

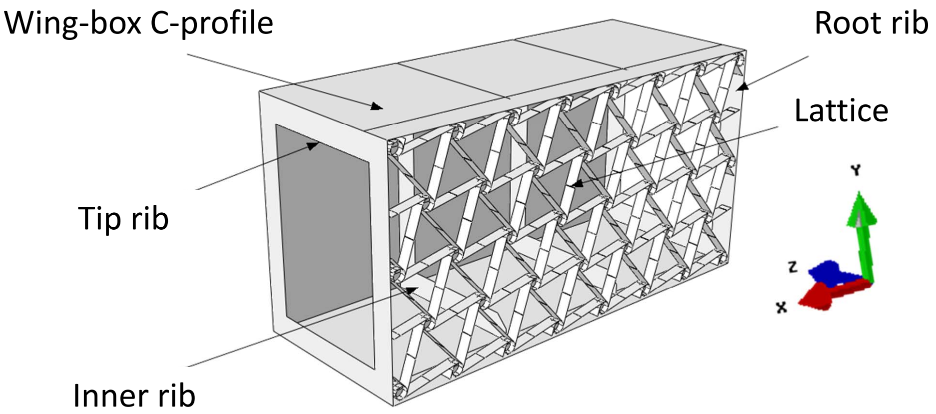

Figure 3.4: General assembly configuration for the computational model. The different parts for the general configuration include the wing-box profile, the lattice of chiral elements and a set of ribs that can be located at the tip, at the root or in between this borders.

The discretization of the structural element was done using continuum shell elements as the basic constituting part. An sketch of a continuum shell element as defined in Abaqus can be seen in Figure **??**.

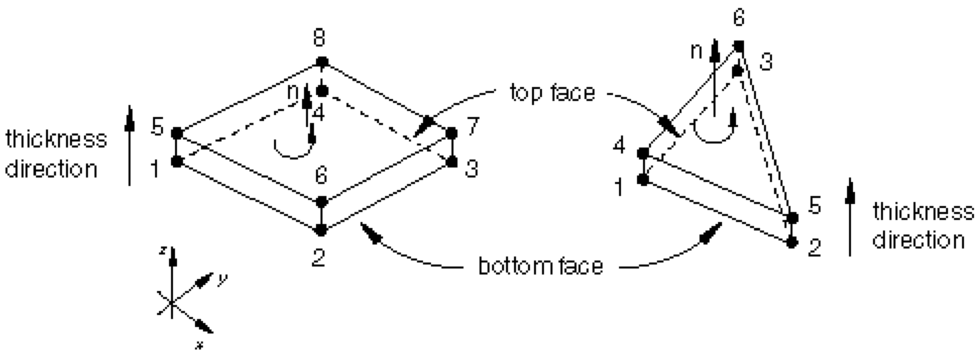

Figure 3.5: Default normals and thickness direction for continuum shell elements in Abaqus. [**?**]

3.3.1 Sub-parts and parametrization of the model

Lattice of chiral elements

The model of the lattice structure is constituted of a network of rigid nodes interconnected by ligaments. At each node, there are six ligaments attached in a uniform distribution that leaves an angular separation of 60° between consecutive attachment points. This network constitutes a lattice of chiral elements. An overview of this part can be seen in Figure **??**. The lattice structure is divided in an integer number of unit cells in the longitudinal (spanwise) and transversal directions. These parameters are identified with the variables N and M for the longitudinal and transversal directions, respectively. In Figure **??**, an sketch of the internal division for $N = 8$ and $M = 3$ is shown. It displays a set of horizontal rectangles that represent each of the transversal M divisions while the set of vertical rectangles correspond to each of the N longitudinal divisions.

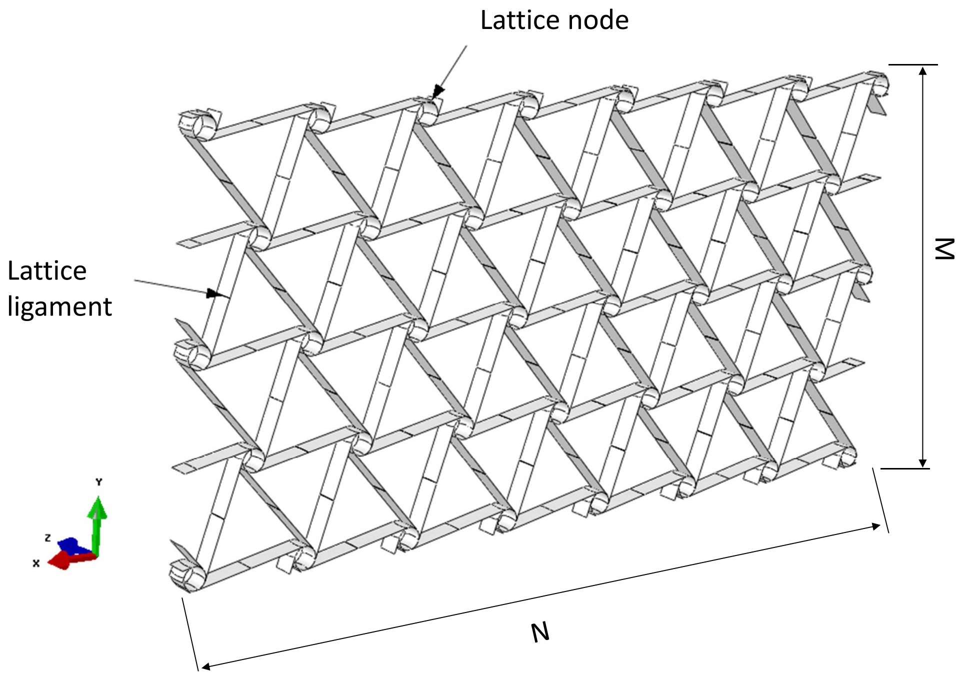

Figure 3.6: Overview of the lattice of chiral elements part. The parameters N and M represent the number of unit cells in the longitudinal (spanwise) and transversal directions, respectively.

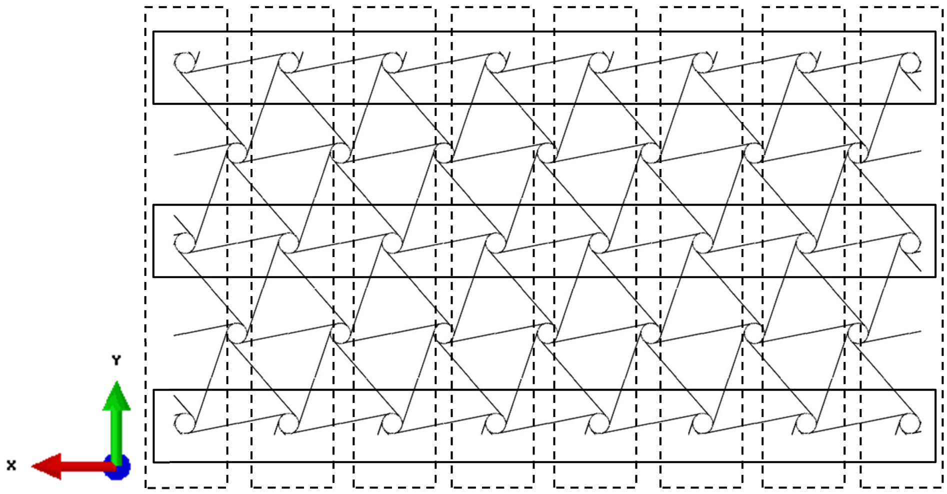

Figure 3.7: Division of the lattice structure in cell units. The sketch shows a lattice with $N = 8$ and $M = 3$. The set of horizontal rectangles represent each of the transversal M divisions while the set of vertical rectangles correspond to each of the N longitudinal divisions.

Furthermore, the internal geometry in the chiral structure is determined by a number of parameters: the thickness t_{chi}, the ligament eccentricity e_{chi}, the ligament half length L_{chi}, the lattice node depth B_{chi} and the lattice node radius r_{chi}. The geometrical meaning of these variables can be seen in the sketch shown in Figure **??**. The thickness t_{chi} applies for both the ligaments and the lattice nodes geometries. The eccentricity e_{chi} is expressed as the dimensionless parameter $\varepsilon_{\mathrm{chi}}$ which is obtained from $\varepsilon_{\mathrm{chi}} = e_{\mathrm{chi}}/B_{\mathrm{chi}}$.

In the sketch shown in Figure **??** an additional dimension variable appears, the ligament eccentricity radius R_{chi} which is dependent on the ligament eccentricity e_{chi} and the lattice node depth B_{chi} as shown in Equation **??**.

A summary of all the parameters introduced to characterize the chiral lattice structure together with their units and nominal values is shown in Table **??**.

$$R = \frac{e_{\mathrm{chi}}^2 + \frac{B_{\mathrm{chi}}^2}{4}}{2e_{\mathrm{chi}}} \tag{3.13}$$

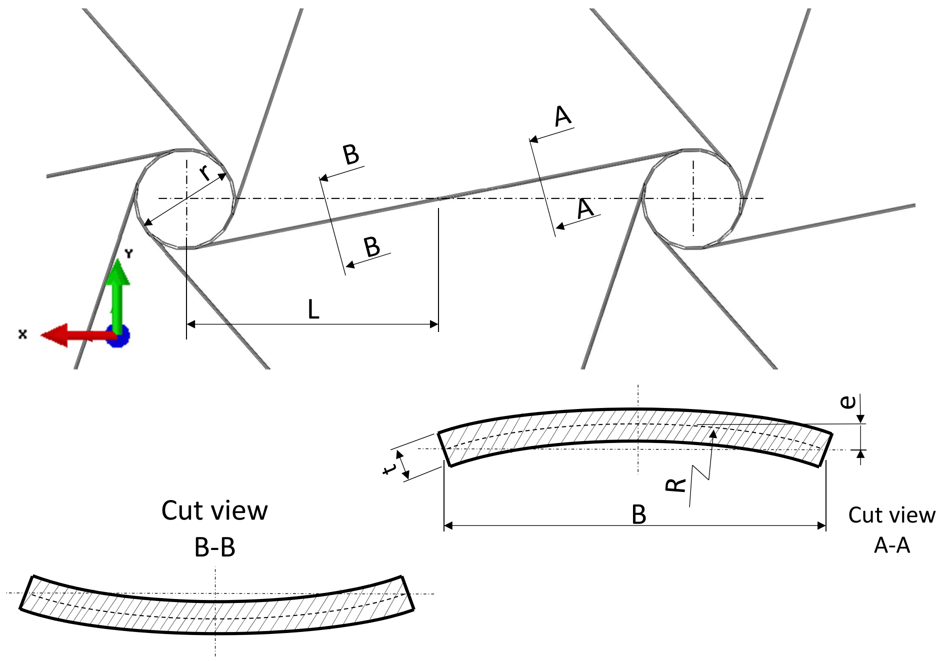

Figure 3.8: Internal parameters of the chiral structure in the lattice. The geometry is characterized by the the ligament eccentricity e_{chi}, the ligament half length L_{chi}, the lattice node depth B_{chi}, the lattice node radius r_{chi} and the thickness t_{chi}. The ligament eccentricity radius R_{chi} which is dependent on the ligament eccentricity e_{chi} and the lattice node depth B_{chi}, as shown in Equation **??**

Parameter	**Symbol**	**Units**	**Nominal value**
Dimensions			
Number of unit cells in spanwise direction	N		8
Number of unit cells in transversal direction	M		3
Dimensionless ligament eccentricity (e/B)	ε_{chi}		0.01
Node radius	r_{chi}	mm	10
Node depth	B_{chi}	mm	20
Ligament eccentricity radius	R_{chi}	mm	250.1
Ligament half length	L_{chi}	mm	50
Thickness	t_{chi}	mm	0.5
Material (ABS)			
Young's modulus	E_{chi}	N/mm^2	3100
Poisson's ratio	ν_{chi}		0.3

Table 3.1: Parameters used for the lattice model. The mechanical properties of the material used correspond to ABS, which is a common thermoplastic polymer.

Wing-box in C-profile

The model of the wing-box consists on a beam with open C profile. The length L_{box} and height H_{box} of the part are determined from those of the lattice of chiral elements. Therefore, the tailorable parameters for this part are the width W_{box}, the thickness t_{box} and the mechanical properties E_{box} and ν_{box} of the material used.

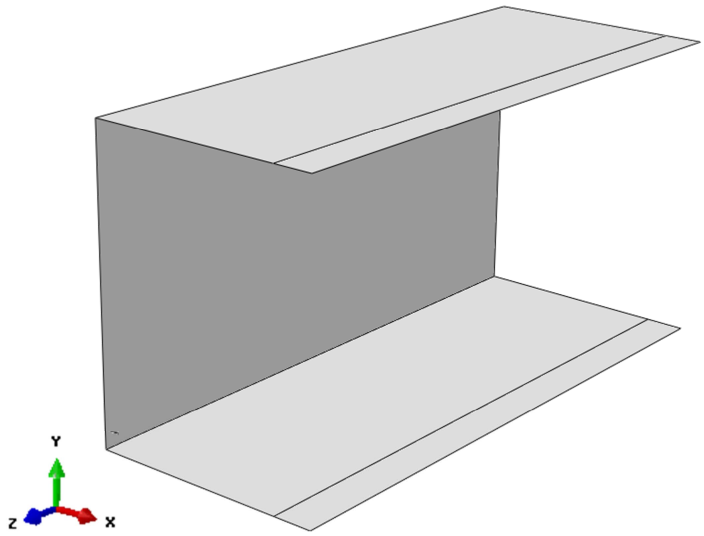

Figure 3.9: Overview of the wing-box in C-profile part

In the sketch shown in Figure **??** it is possible see the geometrical meaning of the parameters introduced in the previous paragraph. Additionally, the Table **??** shows its units and nominal values.

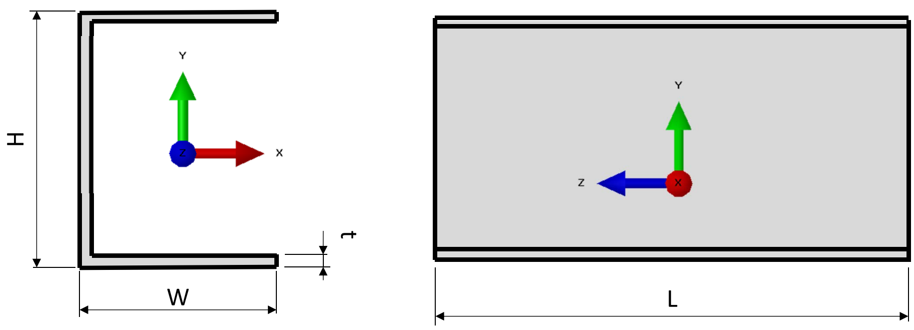

Figure 3.10: Internal parameters of the wing-box C-profile part. The geometry of the part is determined by the length L_{box}, height H_{box}, the width W_{box} and the thickness t_{box}.

Parameter	**Symbol**	**Units**	**Nominal value**
Dimensions			
Wing-box height	H_{box}	mm	383.27
Wing-box length	L_{box}	mm	743.86
Wing-box width	W_{box}	mm	300
Wing-box thickness	t_{box}	mm	0.8
Material (Aluminum)			
Young's modulus	E_{box}	N/mm^2	69000
Poisson's ratio	ν_{box}		0.3269

Table 3.2: Parameters used for the wing-box in C-profile model. The mechanical properties of the material used correspond to standard aluminum. The value of the wing-box height H_{box} and the wing-box length L_{box} are not independent but are calculated based on the transversal and longitudinal dimensions of the chiral lattice structure, respectively.

Ribs

In order to provide the wing-box with additional stiffness in the transversal direction, the addition of ribs is considered. For its design, two different approaches are studied. One considers a open profile design while the other considers a close profile design, as shown in Figure **??**. These could be installed at the tip and/or root of the wing box; and also, in the interior of the wing-box. For those ribs located in this last position, the open section design is preferred to avoid interferences with the lattice of chiral structures. For the ribs located in an outer position, considerations regarding the optimal design choice will be presented in Subsection **??**.

The ribs design is characterized by the widths $W_{\text{rib,close}}$ and $W_{\text{rib,open}}$, and the height H_{rib}. The height H_{rib} and the width of the closed section design $W_{\text{rib,close}}$ are set to be equal to those of the wing-box: $H_{\text{rib}} = H_{\text{box}}$ and $W_{\text{rib}} = W_{\text{rib,close}}$, respectively. The value of $W_{\text{rib,open}}$ is calculated as follows:

$$W_{\text{rib,open}} = B_{\text{chi}} + W_{\text{rib,close}} + d_{\text{chi-rib}}$$

where $d_{\text{chi-rib}}$ represents the gap between the right edges of the inner rib and the lattice chiral structure. This gap ensures that there are not any interferences in between the rib and the lattice chiral structure. The value of this parameter was set to a fix value of $d_{\text{chi-rib}} = 20\text{mm}$. Additionally, the frame width A_{rib} and the thickness t_{rib} allow design modifications.

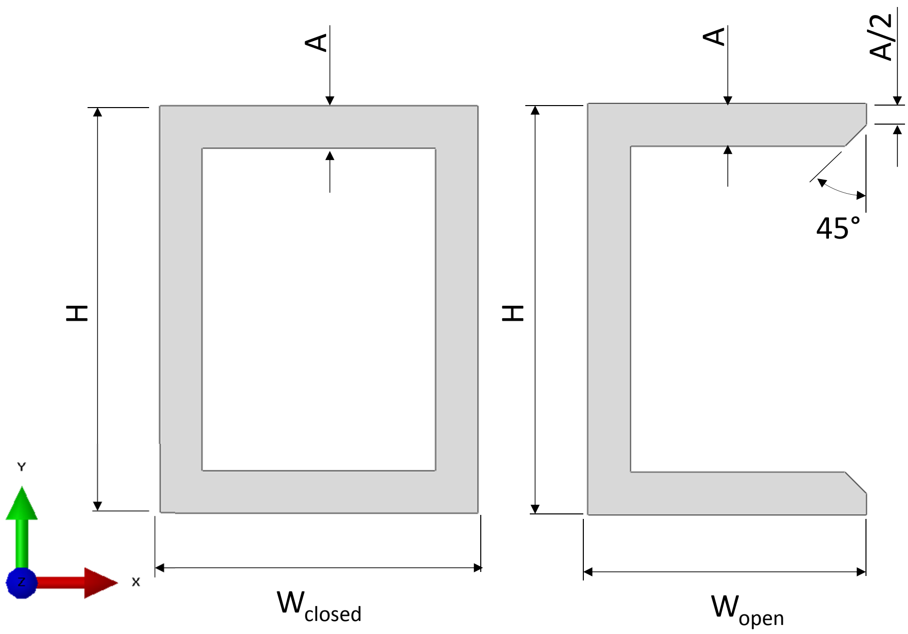

Figure 3.11: Internal parameters of the two different ribs parts. The angle edge for the open section configuration is set to a fix value of 45° to simplify the design and assuming this area of the rib is not critical for the rib duty.

The nominal values of all the parameters involved in the ribs design can be read in Table **??**. The material choice aimed for a configuration stiffer than the wing-box to ensure no out-of-plane deformation of the rib. For this reason, the material chosen is steel.

Parameter	**Symbol**	**Units**	**Nominal value**
Dimensions			
Rib height	H_{rib}	mm	383.27
Closed rib width	$W_{\mathrm{rib,close}}$	mm	300
Frame width	A_{rib}	mm	30
Rib thickness	t_{rib}	mm	2
Material (Steel)			
Young's modulus	E_{rib}	N/mm^2	200000
Poisson's ratio	ν_{rib}		0.25

Table 3.3: Parameters used for the ribs model. The material of choice is steel. The value of the rib width $W_{\mathrm{rib,close}}$ and the height H_{rib} will be equal to the wing-box width W_{box} and to the chiral lattice structure height, respectively.

3.3.2 Computational model mesh characteristics

In the present section, the characteristics of the model spatial discretization are presented. The mesh is unstructured and it is auto-generated by Abaqus CAE for the whole assembly. The elements are a combination of quadratic and tetrahedral with 4 and 3 nodes, respectively. Different mesh elements size are assigned to different parts of the model depending of the geometrical complexity of the area.

In Figure **??**, it is possible to distinguish the two regions that are assigned with different mesh element size: the lattice of chiral structures and the close region of the wing-box skin are assigned with a fine mesh size while the remaining model is assigned with a course mesh size, typically one order of magnitude greater. This introduces two new parameters that are used to modify the mesh size of the different regions:

- S_f: Fine mesh size, typically equal to 3 mm.
- S_c: Course mesh size, typically equal to 30 mm

The selection of this typical values for S_f and S_c are obtained after a number of trial-error attempts to achieve convergence in the nonlinear simulations. As part of the program built to execute the nonlinear simulations, the mesh size is automatically changed if convergence is now achieve. The methodology followed by this program is explained in detail in Subsection **??**.

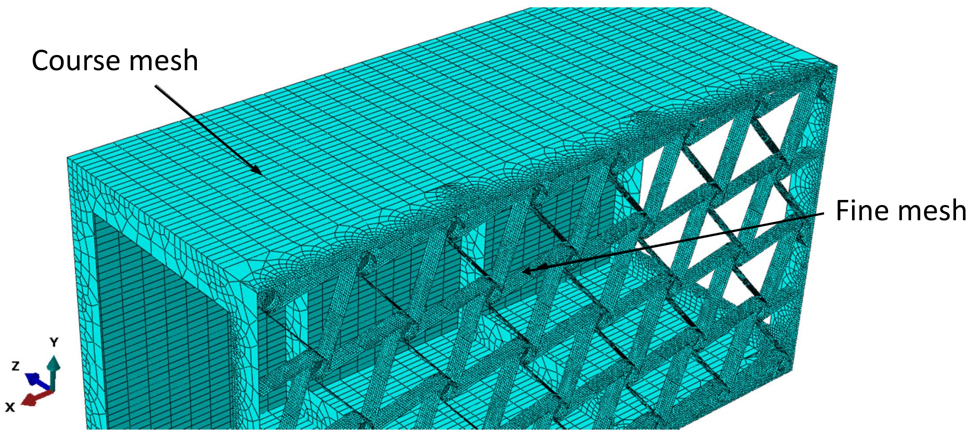

Figure 3.12: Internal parameters of the two different ribs parts. Different mesh element size are assigned to different parts of the model. The lattice structure is assigned with a fine mesh element size while the wing-box is assigned with a course mesh element size.

3.3.3 Load definition

The computational model allowed different possibilities in terms of the load introduction. Among all of them, it was decided to locate the load introduction points on the upper flange of the ribs. The reason for this is the replicate how the load will be introduced in a future manufactured demonstrator of the wing-box.

Therefore, the number of load introduction points had an upper bound equal to the number of ribs available. For the baseline configuration, this number equals to three, one close rib at the tip of the wing-box and two open ribs in the inner part of the wing-box. Another possibility is to vary the position in the chordwise direction of load introduction point or points. In Figure **??** it can be seen the location of the load introduction points when they are distributed among the three available ribs and their position in the chordwise direction is equal to $z/ = 0.8$.

In Subsection **??**, the differences in the response of the structure depending on the number of load introduction points that their position in the chordwise direction are discussed.

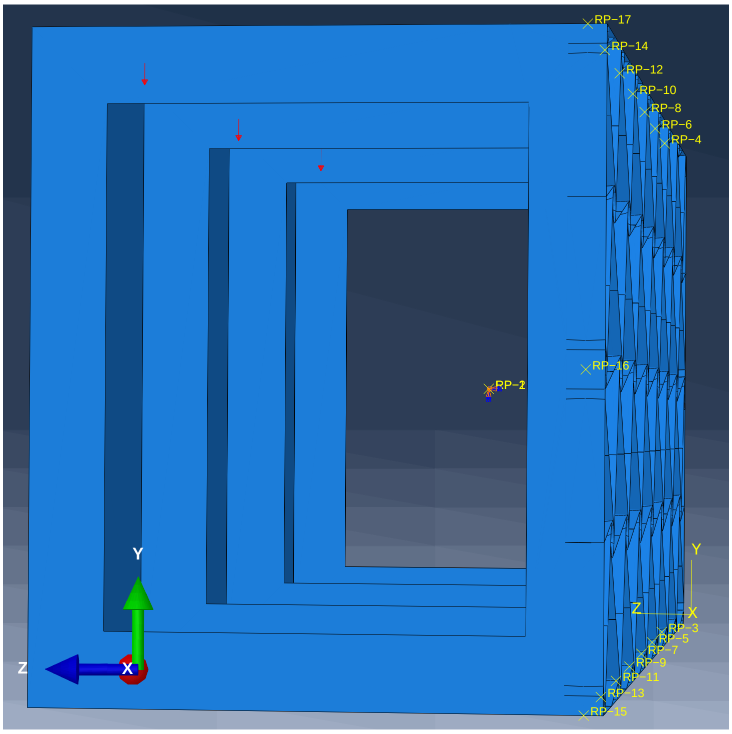

Figure 3.13: Load introduction points located on the upper flange of the tip rib and the two inner ribs.

3.3.4 Boundary condition

The boundary condition for the whole assembly is the one shown in Figure **??**. It consisted in a kinematic coupling similar to the one introduced in Section **??** to model the rigid body behavior of the lattice nodes. In this case, the kinematic coupling is establish between a reference point located approximately at the centre of the root rib and the faces of this mentioned rib. The reference point acts as a master node while the mesh nodes located at the faces of the rib are the slave nodes. The reference point is next fixed in all its degrees of freedom using the corresponding boundary condition Abaqus module.

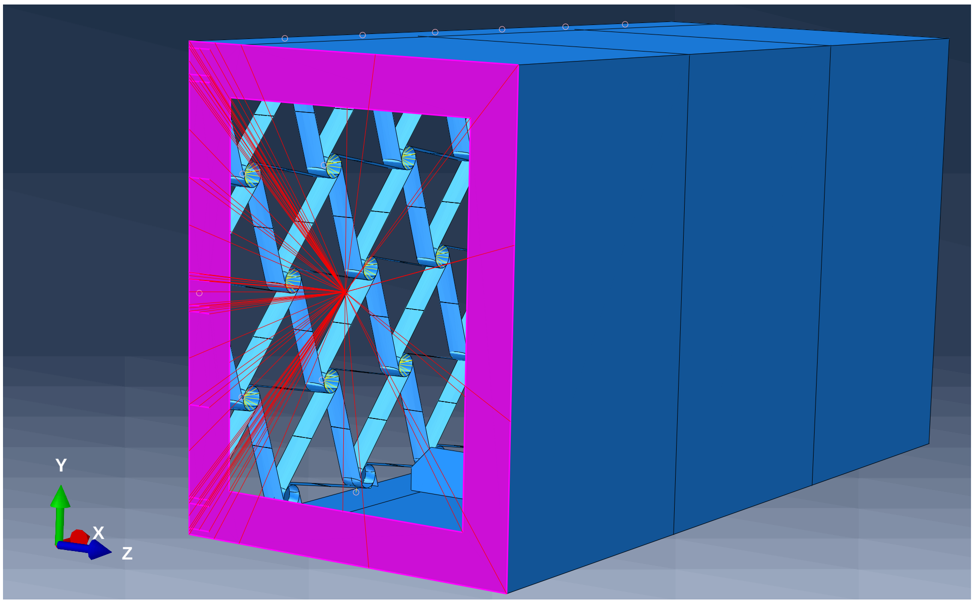

Figure 3.14: Boundary condition for the model. The condition is establish through a coupling interaction between a reference point and the faces of the rib at the root. The reference point is fixed in all its degrees of freedom using the corresponding boundary condition Abaqus module.

3.3.5 Lattice nodes rigid body modeling

The lattice nodes is one of the essential parts of the lattice of chiral elements. These are only constrained in the rotation around its own axis by the ligaments connected to them. For the modeling, they are assumed to behave like a rigid body. In Figure **??**, a closer look to the chiral nodes can be seen, showing two different approaches to manufacture a node that would behave like a rigid body compared with the rest of the structure.

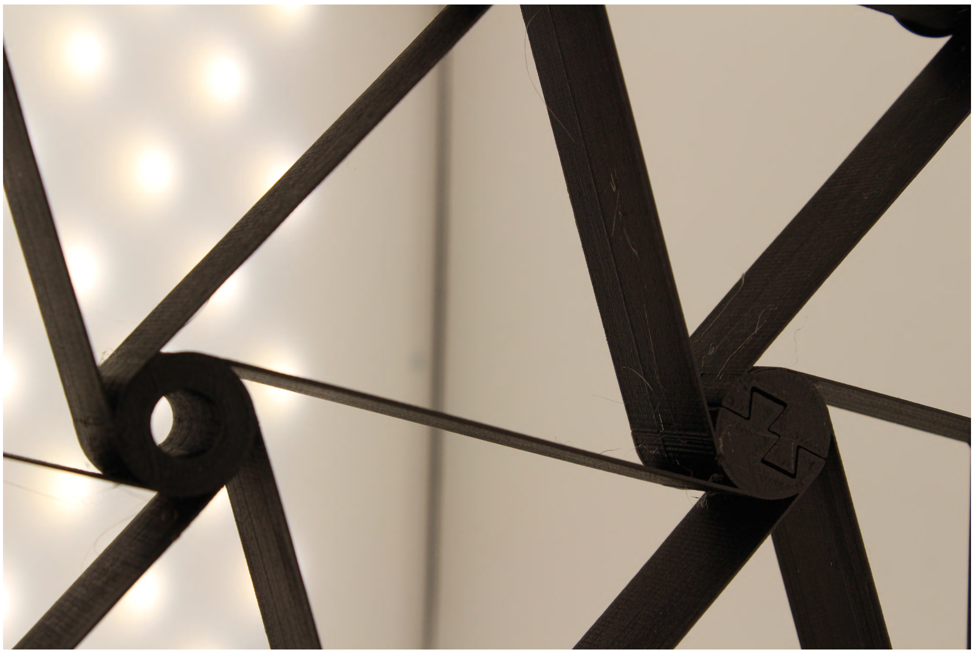

Figure 3.15: Picture of the manufactured chiral lattice nodes. The figure shows two different approaches followed to manufacture the nodes. The one on the right was the standard one showing a cylinder with a thickness bigger than the thickness of the chiral ligaments $t_{\text{node}} \gg t_{\text{ligaments}}$. On the left, an alternative approach is followed in order to allow the assembly of the chiral lattice that is not manufactured as a unique piece. The photography was taken from the demonstrator built by [**?**].

In the Abaqus model, different approaches were followed to model the chiral nodes together with its rigid body feature. The first one was to create a coupling condition using Abaqus corresponding module. In particular, a kinematic coupling is enabled. A kinematic coupling constrains the motion of one or more coupling nodes, also called slave node or nodes, to the rigid body motion of a reference node, also called master node. It is imposed by eliminating degrees of freedom at the coupling nodes. In Figure **??**, an example of a kinematic coupling can be seen.

For the considered case, the coupling nodes are those mesh nodes located at the faces of the lattice nodes and the master node is the reference point located in the center of the lattice node. In order to achieve the rigid solid behavior, all the degrees of freedom translational and rotational are coupled. In Figure **??**, an overview of this coupling condition can be viewed.

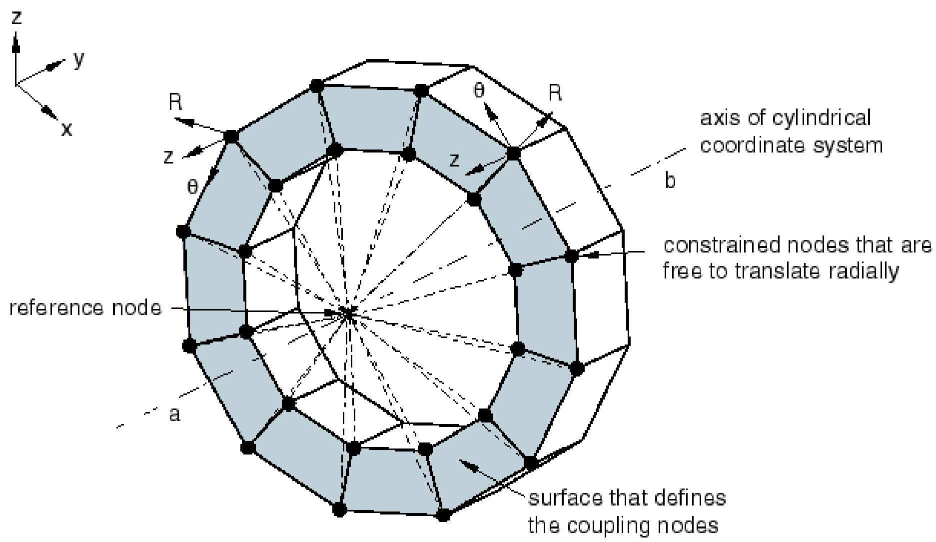

Figure 3.16: Kinematic coupling constraint. The sketch illustrates the use of a kinematic coupling constraint to prescribe a twisting motion to a model without constraining the radial motion. In this case, a local cylindrical reference system is used and the constrained nodes have two degrees of freedom coupled to those of the reference node, the angular position θ and the position along the z axis. The coupling nodes are therefore free to translate radially, varying R. [**?**]

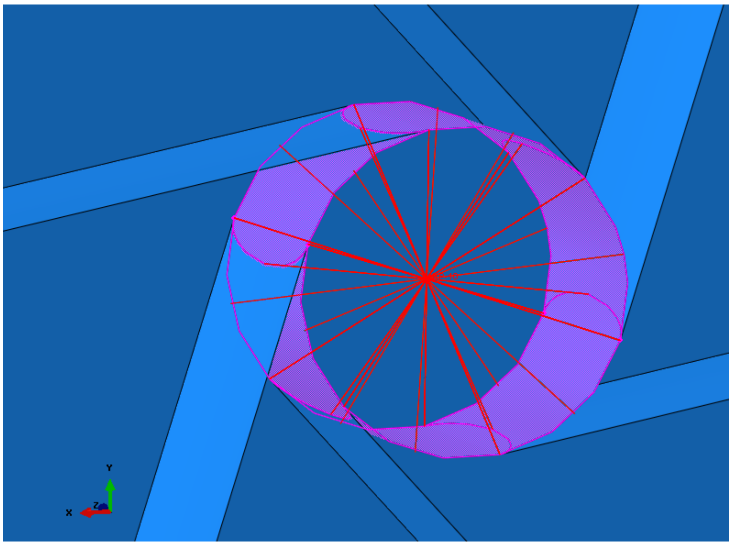

Figure 3.17: Overview of the elements that are involved in the coupling condition at the lattice nodes. The coupling condition was defined in between the mesh nodes located in the faces of the lattice node and a reference point located in the middle. All the degrees of freedom translational and rotational are linked.

Another approach consisted in embedding an additional part inside the lattice nodes to add rigidity to the element. The proposed design of such a part, which is referred as tyre from now on, can be seen in Figure **??**. The internal dimensions of this element are shown in Figure **??**. Its dimensions are dependent on parameters of the chiral lattice, that is, the thickness of the tyre is equal to that of the chiral lattice $r_{\text{tyre}} = r_{\text{chi}}$ and the same occurred for the height B_{tyre} and the radius r_{tyre} which were $r_{\text{tyre}} = r_{\text{chi}}$ and $B_{\text{tyre}} = B_{\text{chi}}$. The added rigidity was obtained as a result of considering a different material for the tyre such that the Young's modulus of the two parts verify the condition $E_{\text{tyre}} \gg E_{\text{chi}}$. Once, the connection is completed, the resulting merged part looked as shown in Figure **??**.

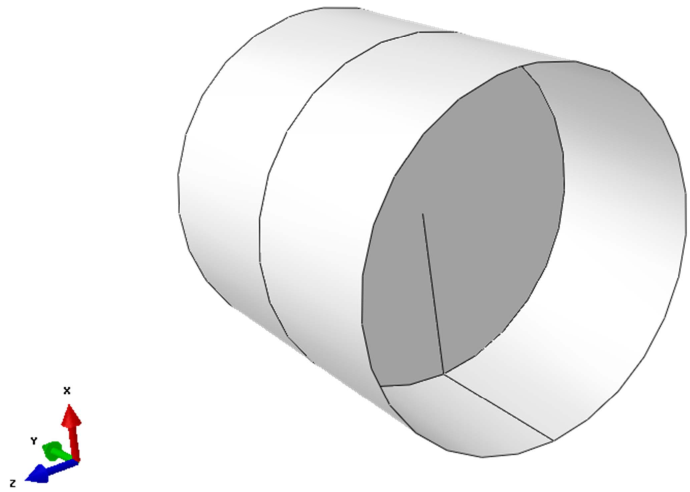

Figure 3.18: Overview of the tyre part.

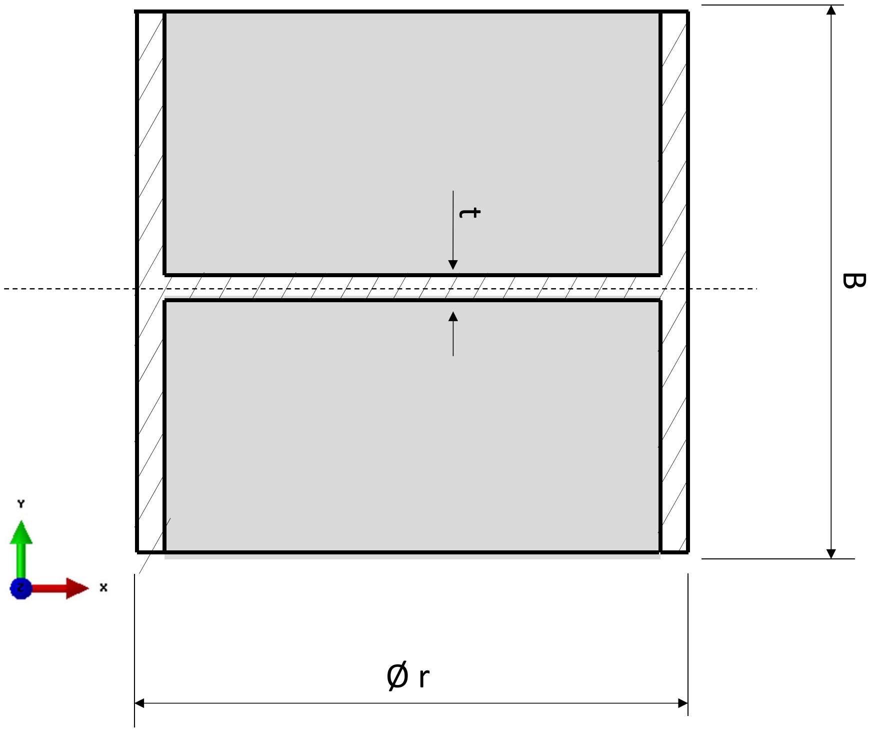

Figure 3.19: Internal parameters of the tyre part. The sketch shows a transversal cut to the part. The tyre is characterized by the radius r_{tyre}, the height B_{tyre} and the thickness t_{tyre}. All this parameters are set to be equal to the corresponding ones in the lattice nodes, therefore: $r_{\text{tyre}} = r_{\text{chi}}$, $B_{\text{tyre}} = B_{\text{chi}}$ and $t_{\text{tyre}} = t_{\text{chi}}$.

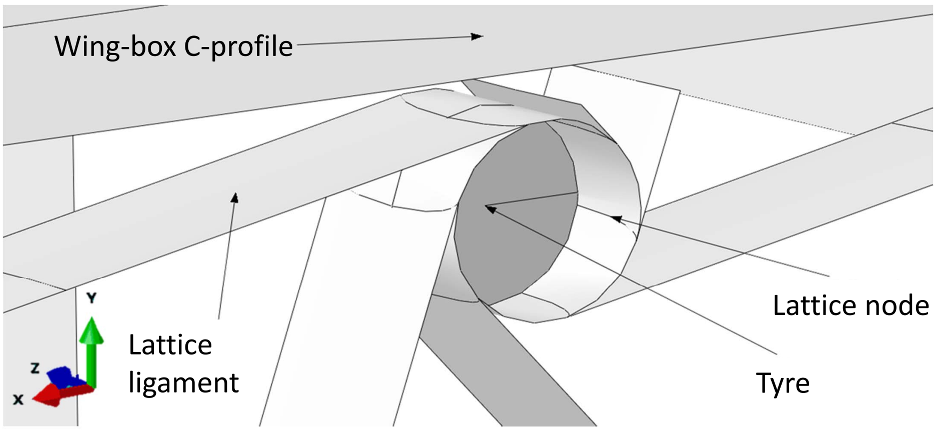

Figure 3.20: Overview of the connection between tyre and lattice node. The tyre will be embed inside the lattice node.

3.3.6 Connection between the wing-box skin and the chiral lattice

In the present subsection, the computational modeling of the connection between the lattice nodes and the wing-box skin is presented. This is an unavoidable transition from the lattice of chiral structures comprised of nodes and ligaments to the skin of the wing-box. Loads are transmitted to the lattice through this attachment points that is why its design results crucial. Three different configurations are studied:

Blocked translation and rotation The lattice nodes have all its degrees of freedom restricted. In this case, the lattice nodes are cut by half and are directly attach to the wing-box skin.

Blocked translation and free rotation The lattice nodes are free to rotate around its own axis. The translation displacement parallel to the skin is restricted. An sketch showing this type of connection can be viewed in Figure **??**. This configuration was the one chosen for the demonstrator built in the Figure **??**.

Free translation and rotation Now the lattice nodes are also allowed to translate parallel to the skin. This configuration is schematically represented in Figure **??**.

Figure 3.21: Detail of the connection between the lattice nodes and the skin. The picture shows the type of connection chosen for the manufactured demonstrator of the lattice. The lattice nodes is allowed to rotate around its own axis but cannot translate parallel to the skin. This photography was taken from the demonstrator built by [**?**].

Depending on the type of connection considered, it is necessary to leave a space gap between the chiral node and the wing-box skin. For the most restrictive case, in which the connection between the lattice structure and the wing-box is rigid, the lattice node was cut by half and directly attached to the

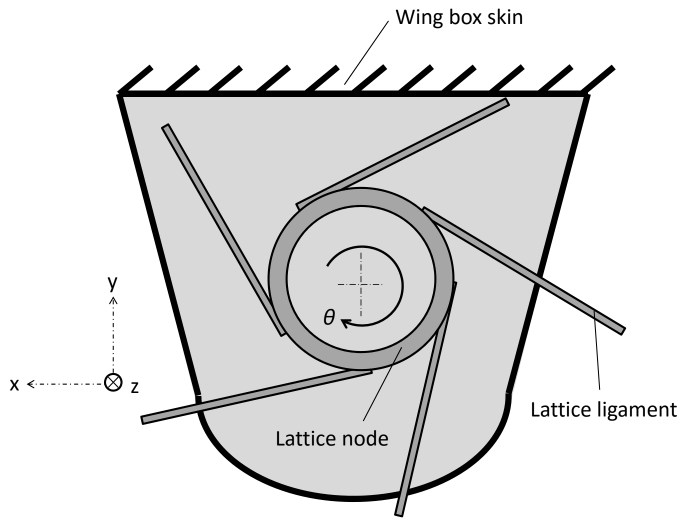

Figure 3.22: Blocked translation and free rotation connection between the lattice nodes and the skin. In this case, the only degree of freedom of the lattice node that it is not restricted is the rotation around its own axis, that is the rotational displacement θ around the direction z.

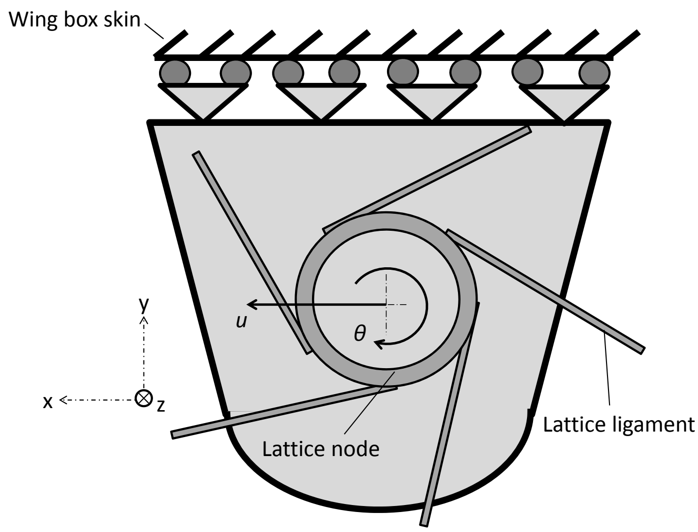

Figure 3.23: Free translation and rotation connection between the lattice nodes and the skin. For this case, the unrestricted degrees of freedom of the lattice nodes are the rotational displacement θ around its own axis, i.e.: the direction z; and the displacement u parallel to the wing-box wall, i.e.: along the direction x.

wing-box skin, as shown in Figure **??**. In this case, there is no gap between the two elements. However, when the allowance of the node rotation is implemented, it is necessary leave a gap between the elements. It becomes then necessary to use the interaction module provided by Abaqus CAE to model the different connections.

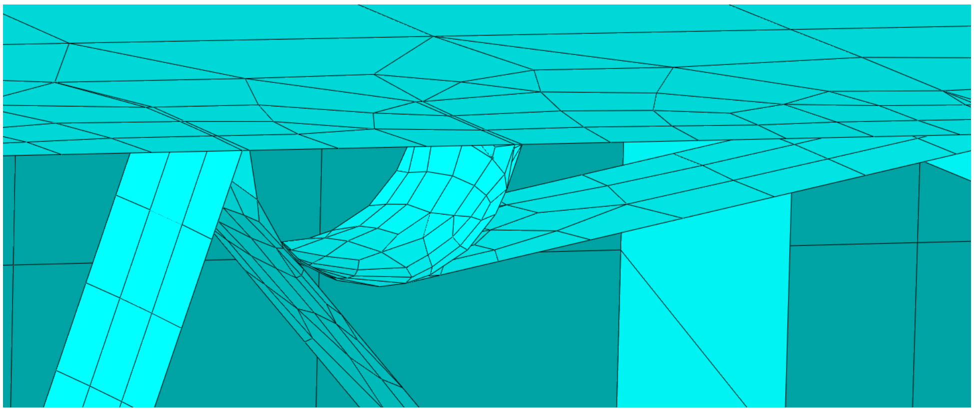

Figure 3.24: Simple rigid connection between the wing-box skin and the chiral node. In this case, none of the possible displacements of the chiral node are left unrestricted. Instead, a solid connection is established through the physical connection and the addition of a coupling condition between a reference point and the mesh nodes located on the lattice node face.

When modeling a type connection between the wing-box skin and the lattice node that allows the free rotation of this last element around its own axis, it is also necessary to preserve the rigid body behavior of the lattice node. For this reason, a tyre part as described in Subsection **??**, is implemented to model both the rigid body characteristics of the lattice node and the allowance of relative displacement between this element and the wing-box skin above it. Therefore, the tyre part is embedded at the centre of each of the lattice nodes located at the border of the lattice structure, as it is shown in Figure **??**. Then, a coupling constraint is established between a mesh node in the middle of the tyre that acts as slave node; and a mesh node located at the wing-box skin just above the tyre that acts as master node, as shown in Figure **??**.

The free rotation of the chiral node is allowed by not constraining the rotational displacement θ around the z direction in the coupling constraint definition. Finally, the last type of connection allowed the displacement of the lattice node parallel to the wing-box skin. For this case, the translational displacement u along the x direction is be left uncoupled.

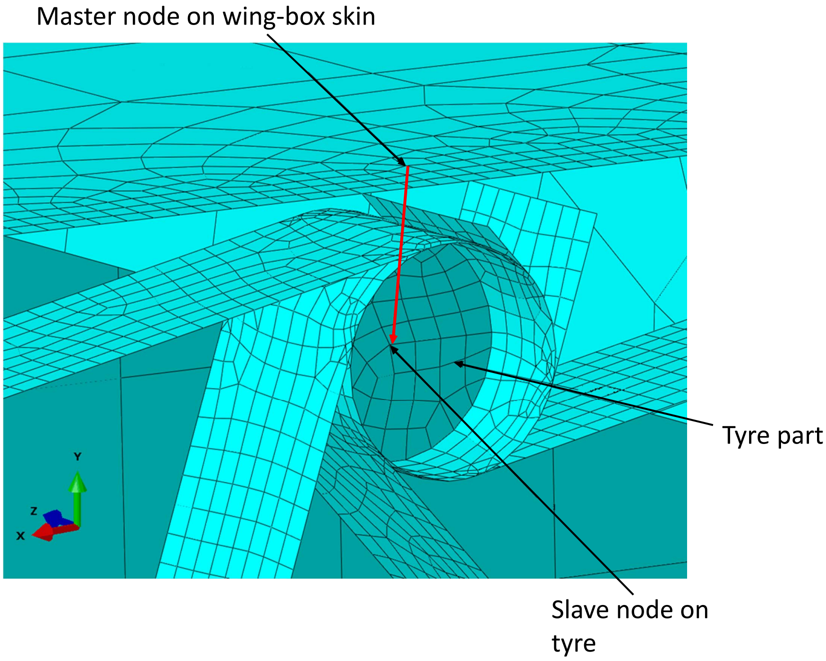

Figure 3.25: Coupling condition between the lattice node and the wing-box skin through tyre. The coupling condition is establish between a mesh node located in the wing-box skin that acts as a master node and a mesh node in the middle of the tyre that becomes the coupling or slave node.

3.3.7 Post-processing operations

The results obtained from the Abaqus simulations were analysed in two different ways. Firstly, qualitatively by means of the deformation plots that shown the corresponding Abaqus visualization module. And, secondly, extracting values of different magnitudes directly from the mesh nodes or elements located at certain positions of interest on the solution model.

As part of the execution of the parametric analysis program written using Python scripting, an additional module is used to perform the post-processing operations. The obtained values of the selected variables are written to an external files.

The calculation of the wing-box twist is done through the evaluation of the rotational displacement u around the x direction at a number of mesh elements located in different parts of the tip rib, as shown in Figure **??**.

Due to deformations occurring at the tip rib, the value of u extracted from each of the mesh nodes is going to differ. A magnitude of this discrepancy between the mean value and the single values of u is shown through the evaluation of the deviation from the mean. The calculated mean value and the maximum deviation are included in the tables that contain results from the simulations.

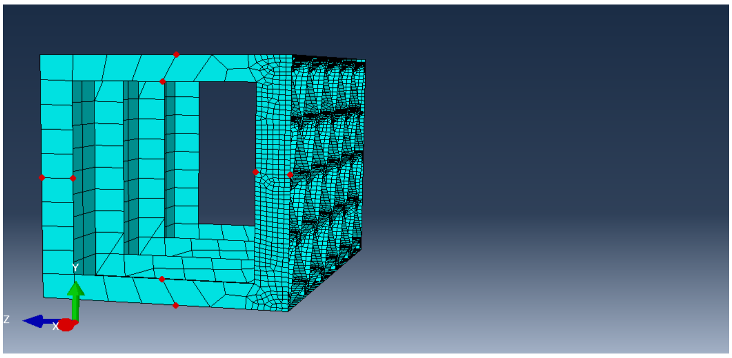

Figure 3.26: Location of the mesh nodes from which valued of the rotational displacement u is extracted. The final value for the twist is calculated from the mean value of u at the mesh nodes shown.

3.3.8 Parametric study method

The model described in the previous subsections is implemented in a Python program that is read by the FEM software, Abaqus CAE. The program is fully parametrized, enabling the possibility of executing simulations for different values of the parameters introduced previously. This procedure consists on a parametric study procedure that is initiated when executing the python file `mainAbaqusParametricStudy.py`. This piece of code reads the parameters that belong to the parametric study by executing the file `setUpParametricStudy` As part of the parametric study process, a computational model is built in Abaqus, submitted for analysis using Abaqus Standard and post-processed by the complementary program `mainBuildAndExecuteWingBox.py`.

The convergence of the simulation is controlled within the program `mainAbaqusParametricStudy.py` and it is able to re-run a simulation with slight variations in the mesh size and/or in artificial dissipation definition if convergence was not achieved.

An schematic characterization of the program execution is shown the flow chart represented in Figure **??**. The code written for this program can be found in Appendix **??**.

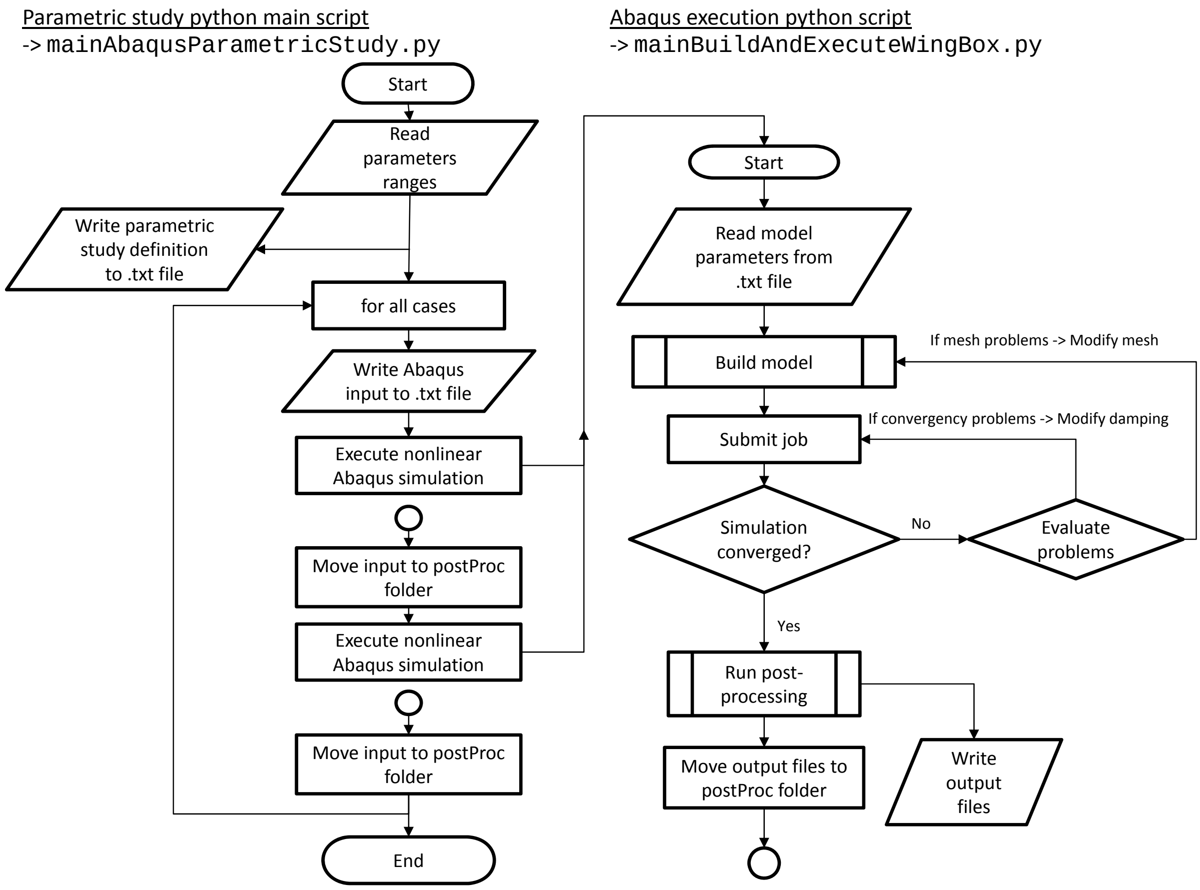

Figure 3.27: Flow chart showing the execution of the parametric study python code. The execution of the parametric study is controlled within the program `mainAbaqusParametricStudy.py`, responsible of the execution the program `mainBuildAndExecuteWingBox.py` that builds the model, submits the job for analysis and performs the post-processing operations on the solution model, for each of the cases considered in the parametric study definition.

Chapter 4

Model analysis

In the present chapter the general characterization of the model is presented. The first section includes an analysis of the analytical model. For this, a variation of the beam geometric parameters and the stiffness ratio E_1/E_2 is performed, and the consequent effect on the mechanical properties and the bending-twist coupling of the beam is evaluated. This analysis provides fast insight of how the different design parameters affect the final mechanical properties of the beam.

In the second section, the computational model is analysed in order to obtain the most suitable configuration that allows the validation of the proposed technology. In particular, discussions over the methods to model the rigid body behavior of the lattice nodes, the load introduction method, the mesh particularities, the ribs inclusion and the nonlinearities the response are presented.

4.1 Analytical model analysis

The analytical model of the wing-box was already presented in the Section **??**. For the results that are presented in the subsections below, the model parameters take the nominal values presented in Table **??**. These are taken from a similar analytical approach to the problem of a wing-box with a variable-stiffness web, presented in [**?**]. By doing this, verification of the results becomes possible.

Parameter	**Symbol**	**Units**	**Nominal value**
Dimensions			
Height of the cross section	H	mm	200
Wing-box length	L	mm	800
Width of the cross section	B	mm	80
Wing-box wall thickness	t_1, t_2	mm	1
Material (Aluminum)			
Young's modulus	E_1, E_2	N/mm^2	69000
Shear modulus	G_1, G_2	N/mm^2	26000

Table 4.1: Nominal value of the parameters used for the analytical model. The mechanical properties of the material used correspond to standard aluminum.

4.1.1 Bending and twisting coupling results and discussion

Here, the influence of the the stiffness ratio E_1/E_2 on the coupling between the bending and the twist deformations of the beam is presented. This is graphically shown in Figure **??** for a number of simulations performed for a load Q_z equal to 2000 N. In the plot, the twist deformation at the tip is shown with the solid line and it is represented using the variable ϕ_{tip}/Q while the bend deformation is shown with the dashed line and it is also represented as w_{tip}/Q.

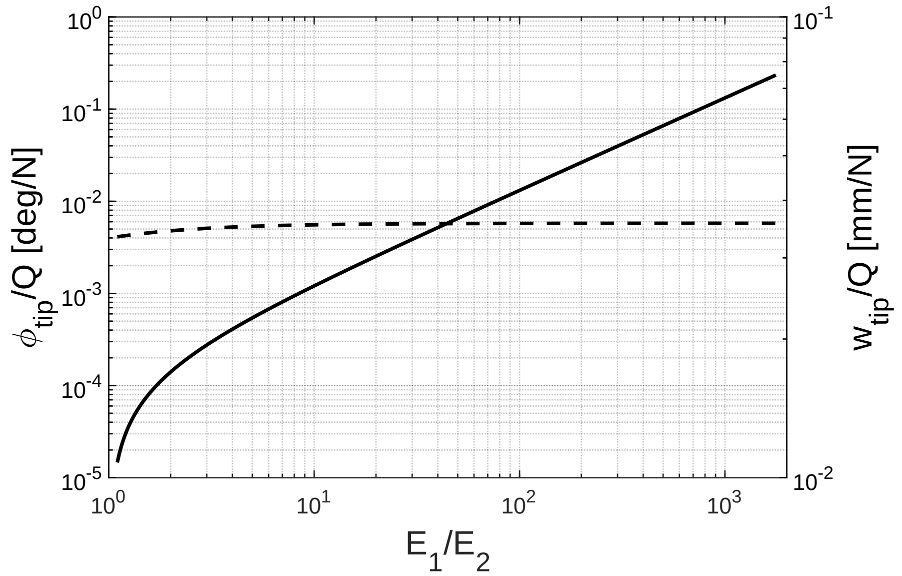

Figure 4.1: Influence of the stiffness ratio E_1/E_2 on the wing-box tip twist ϕ_{tip} and bend w_{tip}. The solid line is used to represent the twist ϕ_{tip} while the dashed line represents the bend w_{tip}. The two displacements correspond to values seen in the wing-box tip and are divided by the applied force magnitude Q_z.

In Figure **??**, the stiffness ratio E_1/E_2 is modified over a wide range such that $E_1/E_2 \in [10^0, 10^3]$. It can be seen that the variable ϕ_{tip}/Q_z is consequently increased by various orders of magnitude from $\phi_{\text{tip}}/Q_z = 10^{-4}$ deg/N to $\phi_{\text{tip}}/Q_z = 10^{-1}$ deg/N, as a consequence of the stiffness ratio variation. However, the variation in bend represented with the variable w_{tip}/Q_z is negligible in comparison. It can be seen that the bending displacement quickly increases for values of $E_1/E_2 > 1$ and it gets to an asymptote for values $E_1/E_2 \gg 1$. These results therefore show how the twist displacement, which gives information regarding the torsional stiffness of the structure, is much more affected by variations of the stiffness ratio E_1/E_2 than the bending stiffness is. Consequently, it is not expected to see large increments in bend displacement in comparison with twist displacement when the variable-stiffness mechanism is activated. This results are in compliance with those presented in [**?**].

For the proposed mechanism, it is expected that the ratio E_1/E_2, which is linked to the effective shear modulus G_{eff} of the real wing-box, is reduced in various orders of magnitude once the buckling phenomena is triggered. After this event, the results above show that the reduction in bending stiffness of the wing-box will be negligible in comparison with the reduction in torsional stiffness.

4.1.2 Parametric study results and discussion

In the present subsection, the variation of the beam mechanical properties for different geometric parameter values is shown. The beam geometry is characterized through the cross-sectional aspect ratio B/H, the thickness ratio t_2/t_1 and the slenderness ratio L/B. The effect of these parameters on the sectional properties, twist and bending stiffness, and flexural and twisting compliance are shown. Additionally, the variance of the stiffness ratio E_1/E_2 is also included in the analysis.

The influence of the cross-sectional aspect ratio B/H on the torsional stiffness GI_t, the shear centre position y_{SC} and the flexural stiffness EI_y is shown in Figures **??**, **??** and **??**, respectively. On its side, the effect of thickness ratio t_2/t_1 on the same three beam parameters is shown in Figures **??**, **??** and **??**.

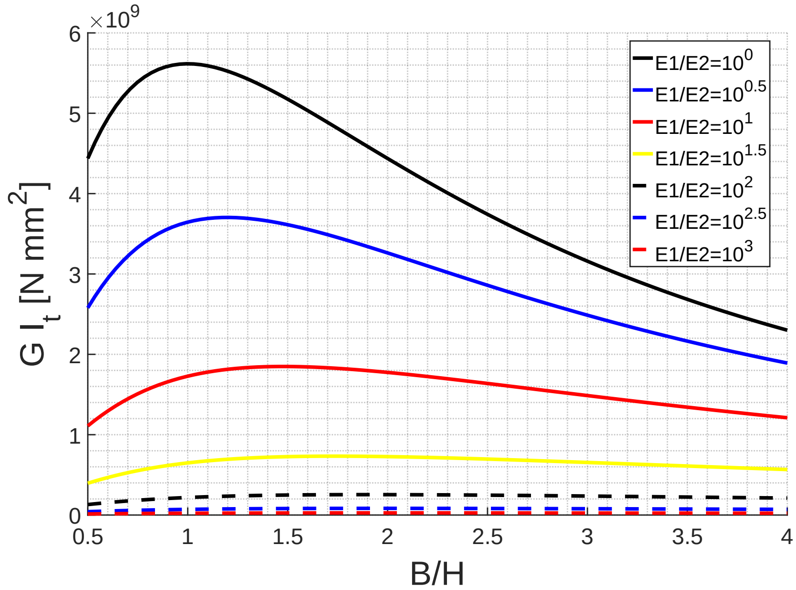

Figure 4.2: Influence of the cross-sectional aspect ratio B/H on the torsional stiffness GI_t, shown for various values of the stiffness ratio E_1/E_2 ranging from 10^0 to 10^3.

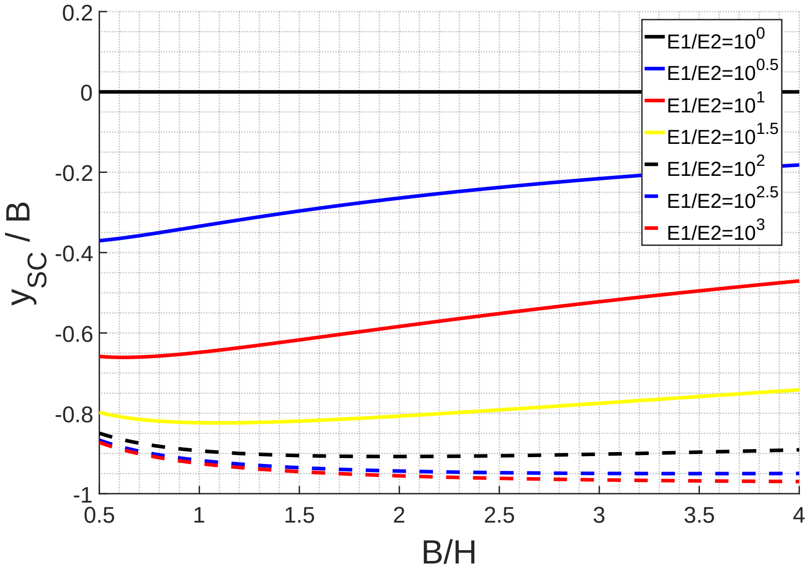

Figure 4.3: Influence of the cross-sectional aspect ratio B/H on the dimensionless shear centre position y_{SC}/B, shown for various values of the stiffness ratio E_1/E_2 ranging from 10^0 to 10^3.

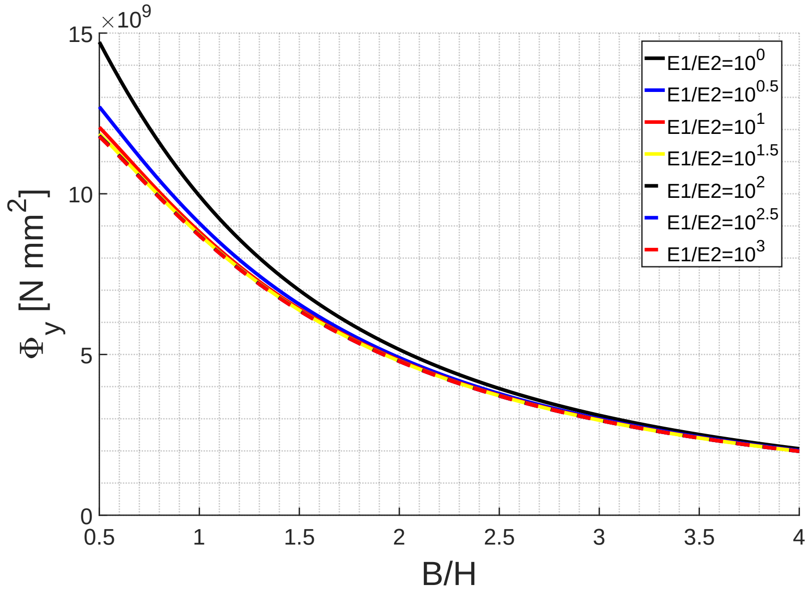

Figure 4.4: Influence of the cross-sectional aspect ratio B/H on the flexural stiffness $EI_y = \Phi_y$, shown for various values of the stiffness ratio E_1/E_2 ranging from 10^0 to 10^3.

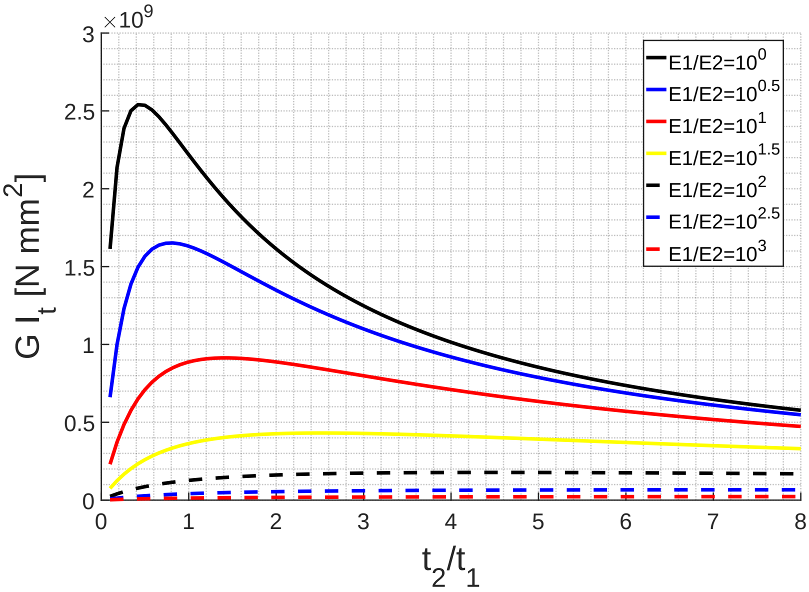

Figure 4.5: Influence of the wall thickness ratio t_2/t_1 on the torsional stiffness GI_t, shown for various values of the stiffness ratio E_1/E_2 ranging from 10^0 to 10^3.

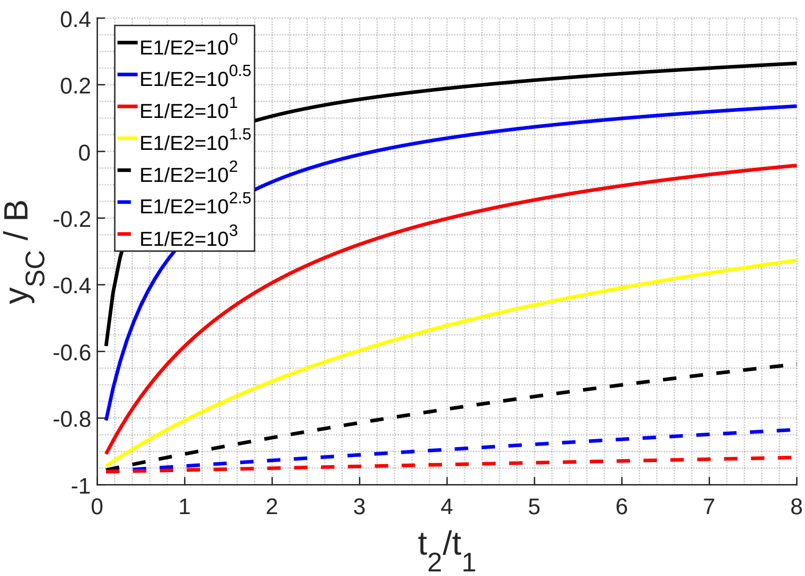

Figure 4.6: Influence of the wall thickness ratio t_2/t_1 on the dimensionless shear centre position y_{SC}/B, shown for various values of the stiffness ratio E_1/E_2 ranging from 10^0 to 10^3.

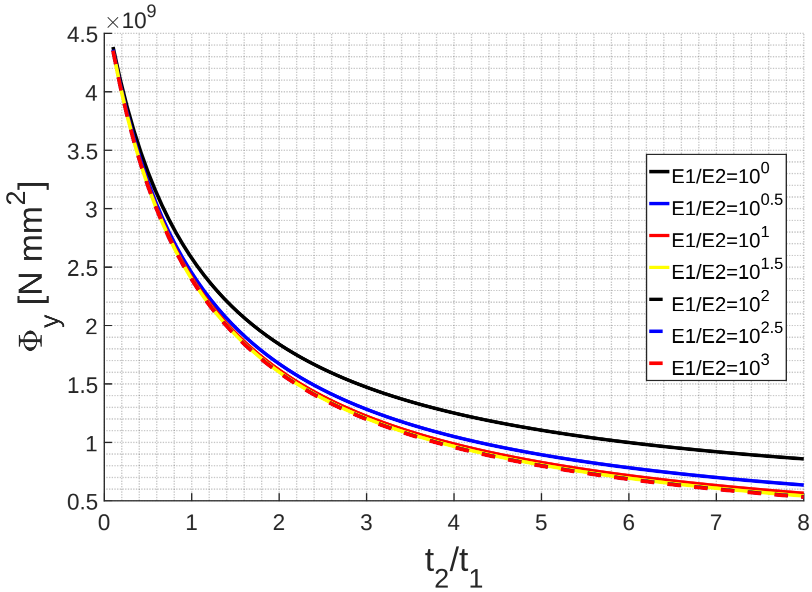

Figure 4.7: Influence of the wall thickness ratio t_2/t_1 on the flexural stiffness $EI_y = \Phi_y$, shown for various values of the stiffness ratio E_1/E_2 ranging from 10^0 to 10^3.

In Figure **??**, it can be seen that a maximum torsional stiffness appears for $B/H = 1$ when $E_1/E_2 = 1$. This can be explained because, as it is also shown in [**?**], the closer the torsional stiffness to the doubly symmetric case, the higher its torsional stiffness. However, when $E_1/E_2 > 10$, the maximum torsional stiffness is shown to appear for $B/H > 1$. A similar conclusion can be extract when analyzing the Figure **??**, that shows the influence of the thickness ratio t_2/t_1 on the torsional stiffness GI_t.

In Figure **??** shows that for values $E_2 \ll E_1$, the shear centre position y_{SC} is approximately constant for B/H variations. In this context, the beam approximates its behavior as if it has an open profile section. However, as the value of E_1/E_2 decreases, the influence of the ratio B/H increases showing a bigger influence of the web where the Young's modulus E_2 applies. On the other hand, Figure **??** shows that the bigger the thickness ratio t_2/t_1 is, the closer that the shear centre y_{SC} will be to the vertical axis of symmetry. However, for $E_2 \ll E_1$ the influence of the thickness ratio t_2/t_1 is reduced.

In Figure **??** it can be seen that the flexural stiffness EI_y decreases when the cross-sectional aspect ratio B/H increases. This is explained because the second moment of area I_y is reduced when B/H increases as the coordinate y of the points in the section is reduced as well. Similarly, it can be seen in Figure **??** that when the thickness ratio t_2/t_1 increases, the value of EI_y decreases. In both cases, the flexural stiffness EI_y is little affected by variations of the stiffness ratio E_1/E_2. This result matches what was already shown in Subsection **??**.

Additionally, the effect of the cross-sectional aspect ratio B/H on the deflection and torsional compliances is shown in Figures **??** and **??**, respectively. The corresponding plots when analyzing the effect of the thickness ratio t_2/t_1 on the deflection and torsional compliance are shown on Figures **??** and **??**, respectively. The beam torsional compliance is expressed as a fraction of the twist at the tip divided by the vertical force applied, that is $|\phi_{\text{tip}}|/Q$, while the beam flexural compliance is expressed as fraction of the maximum vertical displacement at the tip divided by the vertical force applied, that is $w_{0,\text{tip}}/Q$.

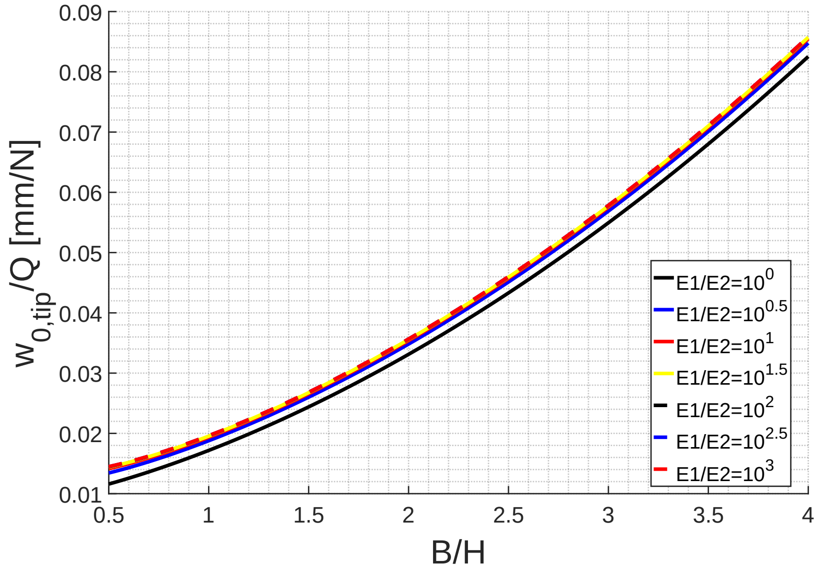

Figure 4.8: Influence of the cross-sectional aspect ratio B/H on the flexural compliance $w_{0,\text{tip}}/Q$, shown for various values of the stiffness ratio E_1/E_2 ranging from 10^0 to 10^3.

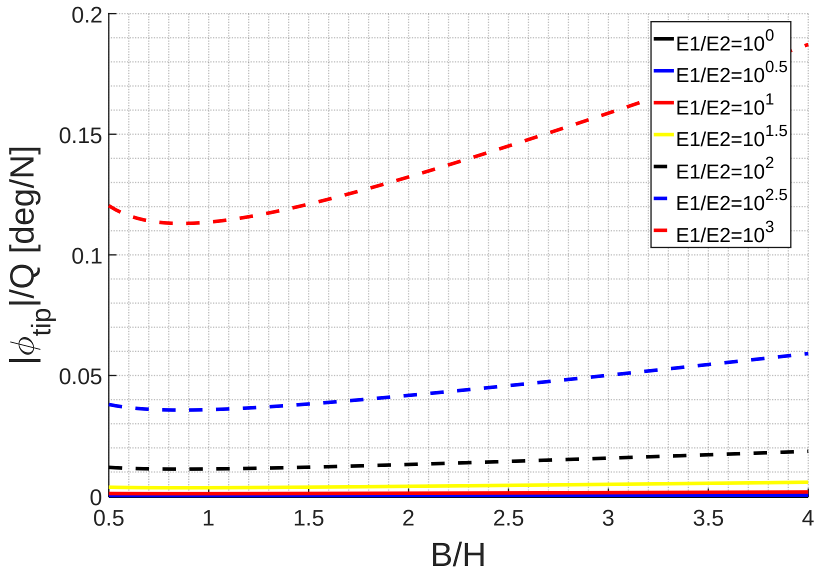

Figure 4.9: Influence of the cross-sectional aspect ratio B/H on the torsional compliance $|\phi_{\text{tip}}|/Q$, shown for various values of the stiffness ratio E_1/E_2 ranging from 10^0 to 10^3.

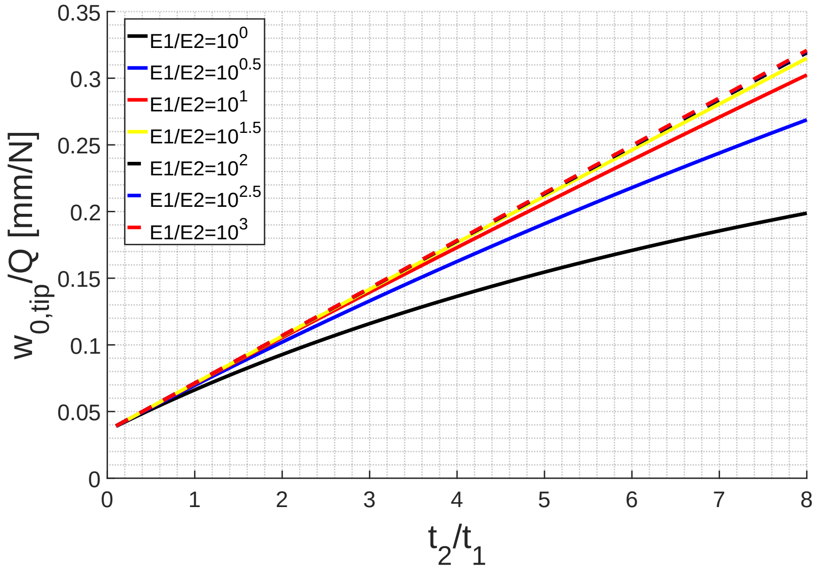

Figure 4.10: Influence of the thickness ratio $t2/t1$ on the flexural compliance $w_{0,\mathrm{tip}}/Q$, shown for various values of the stiffness ratio E_1/E_2 ranging from 10^0 to 10^3.

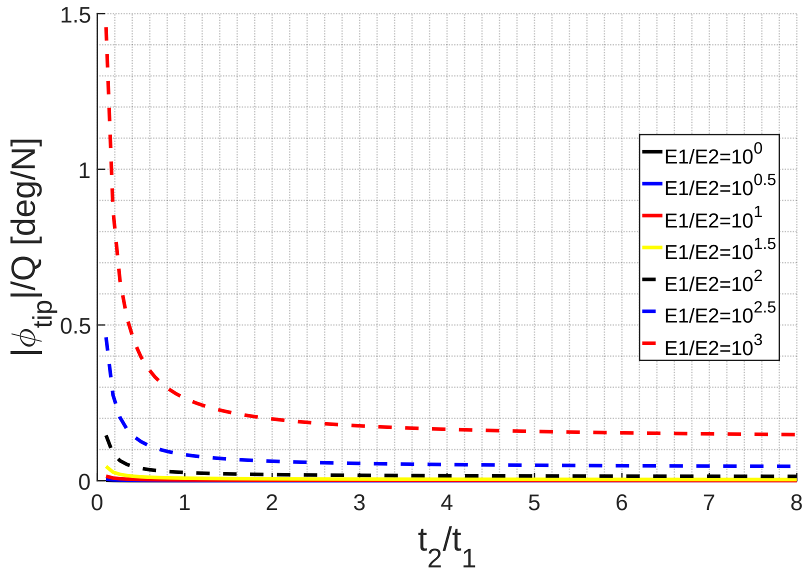

Figure 4.11: Influence of the thickness ratio $t2/t1$ on the torsional compliance $|\phi_{\mathrm{tip}}|/Q$, shown for various values of the stiffness ratio E_1/E_2 ranging from 10^0 to 10^3.

From the analysis of the torsional compliance $|\phi_{\text{tip}}|/Q$ as a function of the thickness ratio t_2/t_1 in Figure **??**, it can be seen that increments in t_2/t_1 amplifies the effects of variations of the stiffness ratio E_1/E_2 on the flexural compliance $w_{0,\text{tip}}/Q$. On the other hand, Figure **??** shows that the flexural compliance $w_{0,\text{tip}}/Q$ increases when the cross-sectional aspect ratio B/H increases and the value of B/H does not alter the magnitude of the effect of variations of E_1/E_2 in the flexural compliance, effect that remains small.

From Figure **??**, it can be understood that there is not variation in the torsional compliance for values of the thickness ratio $t_2/t_1 > 1$; but for $t_2/t_1 < 1$, the torsional compliance increases considerably. This result shows again something similar at what it was shown in Subsection **??**, how the modification of shear stiffness in the second web has a considerable effect on the torsional stiffness. On the other hand, Figure **??** shows small effect of the variation of the cross-sectional aspect ratio B/H on the torsional compliance.

The effect of the slenderness ratio L/B on the deflection and torsional compliances is shown in Figures **??** and **??**, respectively. These two figures show how the flexural and torsional compliance increase for increasing values of L/B. Also, Figure **??** shows again the small influence of the stiffness ratio E_1/E_2 in the flexural compliance while Figure **??** shows how the torsional compliance is considerably affected by variations of E_1/E_2.

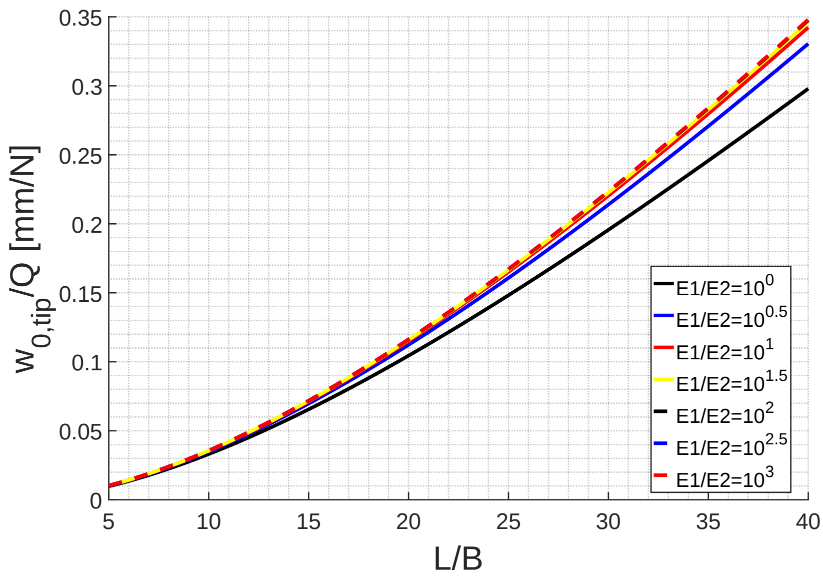

Figure 4.12: Influence of the slenderness ratio L/B on the flexural compliance $w_{0,\text{tip}}/Q$, shown for various values of the stiffness ratio E_1/E_2 ranging from 10^0 to 10^3.

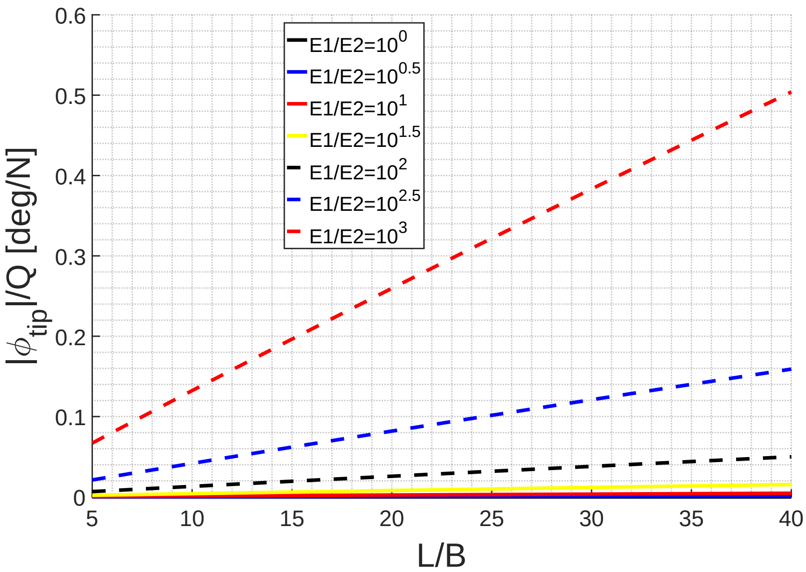

Figure 4.13: Influence of the slenderness ratio L/B on the torsional compliance $|\phi_{\text{tip}}|/Q$, shown for various values of the stiffness ratio E_1/E_2 ranging from 10^0 to 10^3.

4.2 Computational model analysis

In the present section, results from the analysis performed on the computational model are presented. Different aspects of the model are evaluated and design decisions are justified. The analysis is going to consider the modeling of the lattice nodes rigid behavior, the different load introduction strategies, the influence of the mesh in the simulation convergence, the ribs addition and the nonlinearities that appear in the problem.

For the proposed technology, it is expected to see the appearance of large deformations and elastic instabilities in the structure. This means that the structural stiffness of the model is going to be altered as the load applied increases. For this reason, it becomes necessary to execute nonlinear simulations in which the load applied is increased by small step increments. Each of these steps constitute a different frame that contains particular magnitudes values for each of the mesh nodes and elements.

Furthermore, linear simulations are also executed to provide information of the expected response of the structure considering its initial stiffness, before the onset of the elastic instabilities that alter the stiffness. The results obtained from the nonlinear simulations are compared to those obtained from the linear simulations. This comparison is done by means of the curve displacement-force that shows the achieved twist adaptation of the wing-box at each of the frames that build up the complete simulation window.

In addition to this general nonlinear/linear global response comparison, the performance of the structure is also analysed by means of the evaluation of the six possible displacements of the mesh nodes at different parts of the structure. The value of these magnitudes are shown in colour contours plots over the solution model.

4.2.1 Rigid body modeling

Two different approaches are followed to model the rigid body behavior of the lattice nodes, as it been already explained in Subsection **??**. The first modeling approach considers the creation of a coupling condition between a reference point positioned at the centre of the lattice node cylinder and mesh nodes located in the faces of the lattice node. The second approach consists on the introduction of an additional part that is placed in the middle of the cylinder to add stiffness to the element. In this section, the results obtained for each modeling approach are compared.

In Figure **??**, the displacement-force curve for the nonlinear and linear responses in wing-box twist obtained for each modeling approach are compared. It can be seen that when the tyre approach is used, the collapse of the structure occurred at a smaller load than if the approach with the coupling implementation is used.

Also, the analysis of the mesh nodes displacements on the solution model shows that, when the tyre rigid body behavior is modeled using the tyre part, the rotation of the lattice nodes around its own axis is approximately 20% higher than when the modeling is done using the coupling constraint. This rotation should be free and be only constrained by the connection to the ligaments. Therefore, it is concluded that the use of the tyre part is a more realistic approach to modeling the rigid body behavior of the lattice nodes.

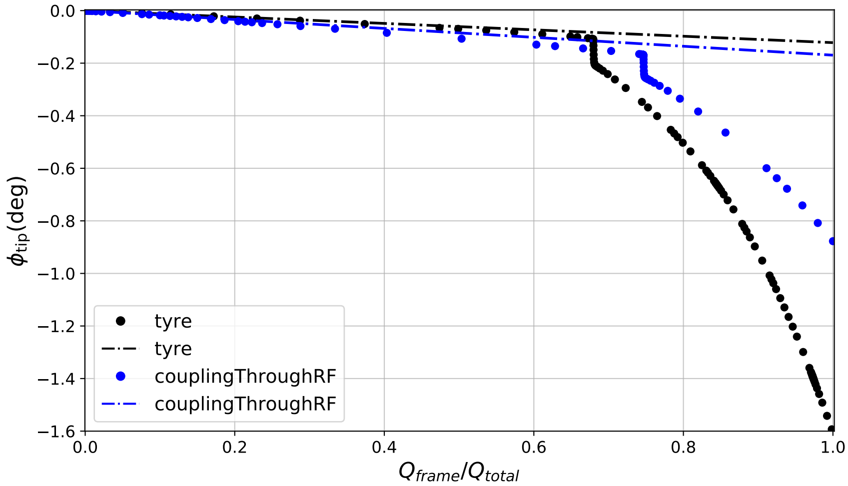

Figure 4.14: Displacement-force curve obtained using different approaches to model the rigid lattice node.

4.2.2 Load introduction method

As shown in Subsection **??**, there are multiple ways in which the load can be introduced into the structure. It was decided to locate the load introduction points at the upper flange of the ribs in an attempt of replicate how the load introduction would be done in a future manufactured demonstrator. In this subsection, the difference of results obtained when modifying the load introduction method are shown.

Firstly, the option of distributing the same load over the total number of ribs, three in the baseline configuration, is compared with the option of concentrating all the load on the upper flange of the tip rib. In Figure **??**, the curve displacement-force is shown for these two different cases. It can be seen how when the load is distributed over a number of points and it is not concentrated on a single point, a delay in the onset of the structure collapse occurs. This result is correlated with visual inspection of the displacement of the mesh nodes on the solution model in Abaqus. The corresponding colour contour of the rotational total displacement $\sqrt{\theta^2+\phi^2+\psi^2}$ for a distributed load is shown in Figure **??**. Here it can be seen how buckling has started to occur on the ligaments located close to the ribs, where the load is being introduced. In a further stage, if the load would increase, buckling would start to occur at the root of the wing-box.

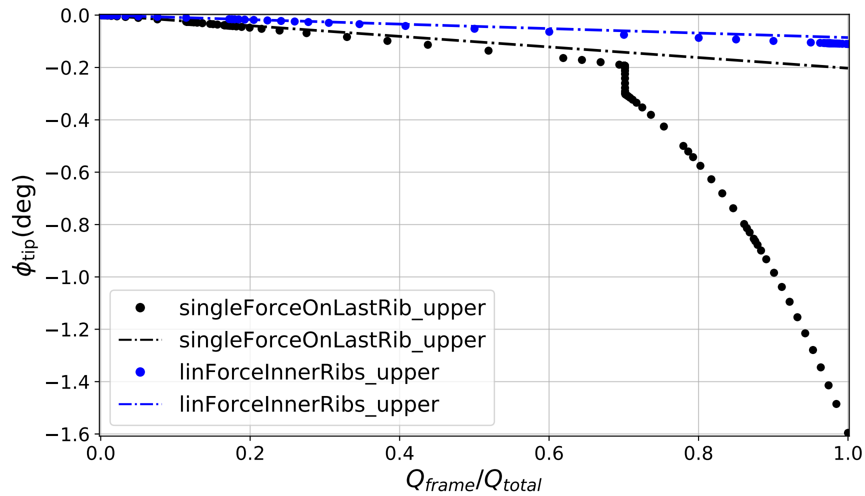

Figure 4.15: Displacement-force curve showing the model response using different load introduction methods. The label "singleForceOnLastRib_upper" corresponds to the case of using one single point for the load introduction. This point is located at the upper flange of the tip rib. The label "linForceInnerRibs_upper" corresponds to the case of introducing load on the upper flange of all the available ribs, which are three for the baseline configuration, two in the inner part of the wing-box and one at the tip. It can be see that the concentration of the load advances the onset of the structure collapse.

Secondly, in Figure **??** a comparison of the response for different load position points in the chordwise direction is shown. The plot shows the displacement-force curve for four values of the variable z/W_{box}. A smaller value of z/W_{box} represents a load introduction point located closer to the chiral lattice.

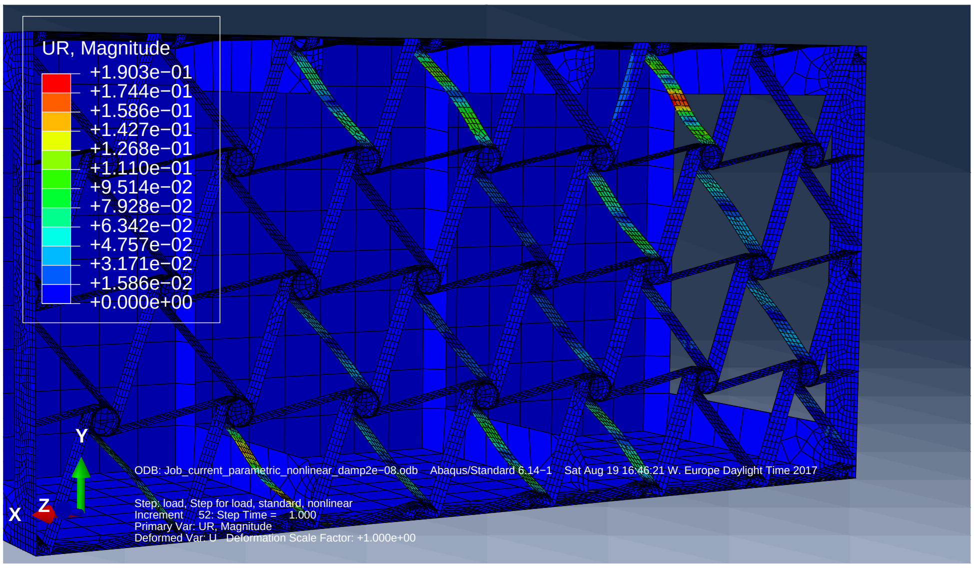

Figure 4.16: Deformed state of the model for a distributed load introduction method. It can be seen how since the buckling is starting to occur at the ligaments located close to the ribs, the onset of the elastic instabilities is delayed.

It can be seen that buckling is not triggered for values of z/W_{box} equal to 0.6 and 0.8. This is explains because the further the introduction point is from the chiral lattice, the less shear strain appears on the chiral lattice and the later that the onset of the elastic instabilities occurs.

Since the distribution of the load in more that one rib only delays the onset of the instabilities, it is decided to use a single load introduction point for the study performed on the baseline configuration, in a attempt to simplify the model. Also, it is decided to locate the load introduction point at $z/W_{\text{box}} = 0.5$ to keep the symmetry.

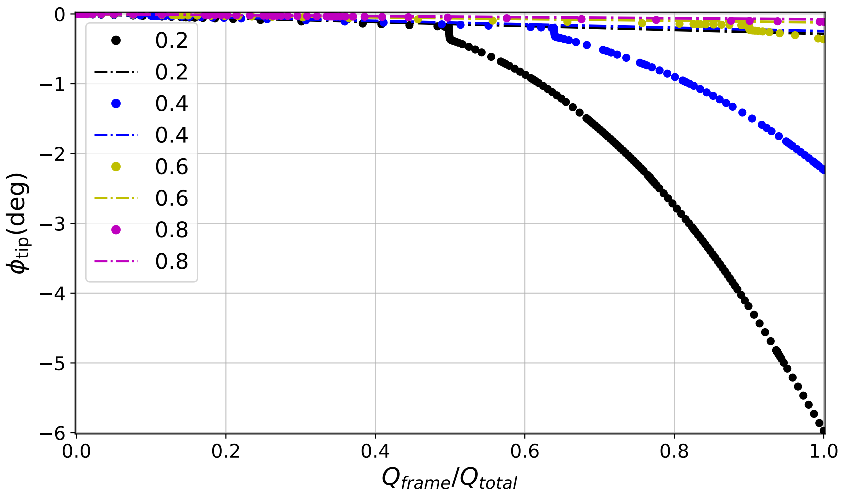

Figure 4.17: Displacement-force curve showing the model response for different load introduction points z/W_{box}. A smaller value of z/W_{box} represents a load introduction point located closer to the chiral lattice. The further the introduction point is from the chiral lattice, the less shear strain appears at the chiral lattice and the later that the onset of the elastic instabilities occurs.

4.2.3 Mesh

The model is build using cell shell elements as the fundamental constituting part. The thickness is assigned in the perpendicular direction, as it is shown in Figure **??**.

This type of element is a 2D element that it was used to build 3D structures. This kind of procedure may incur in distortions in the mesh elements due to shell elements intersecting in the same line at different angles.

For the designed model, this situation occurred at certain points of the chiral lattice. It can be seen in Figure **??** that the distorted elements appear at two different positions mainly. Firstly, at the plane where the two ligaments with different curvature join. At this point, the sharp angles that appear in between the part geometrical lines induce the appearance of tetrahedral distorted mesh elements. The second typical location for appearance of distorted elements is along the curve where the lattice nodes and the curved ligaments join.

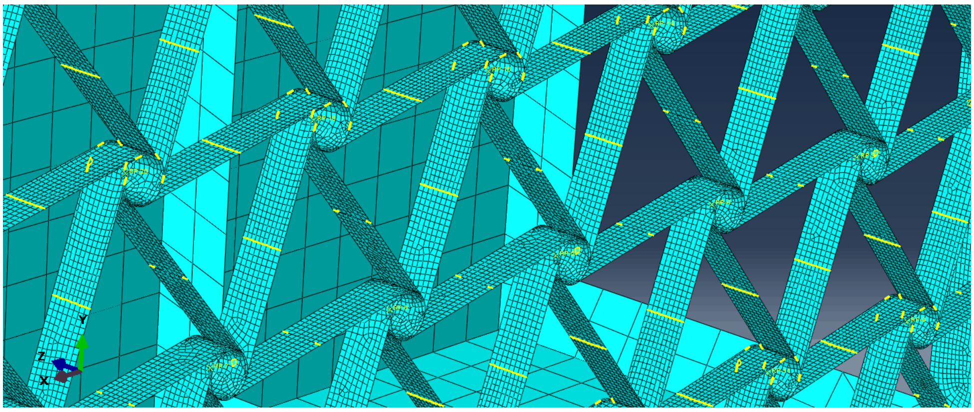

Figure 4.18: Distorted mesh elements in the model. The number of distorted elements was found to be crucial for the simulation convergence.

It was seen that the number of distorted elements had a significant effect in the simulation convergence evolution. For a high number of distorted elements, the simulation could not go further from the first step. No attempts to locally modify the mesh at the mentioned locations were made, instead, it was found that modifying the global mesh size gave enough control over the number of distorted elements to be able to overcome this limitation. The bigger the mesh size in the area, the less distorted elements appear after completing the meshing operations.

4.2.4 Nonlinear problem and automatic stabilization

For the case under study, nonlinear simulations will be carried out as is expected to find a nonlinear displacement-force curve as a result of the analysis. In Abaqus, to execute nonlinear simulation involves the following, as shown in [**?**]:

- a combination of incremental and iterative procedures;
- using the Newton method to solve the nonlinear equations;
- determining convergence;
- defining loads as a function of time; and
- choosing suitable time increments automatically.

Therefore, Abaqus breaks the step where the load is applied into increments. The software will automatically choose the size of each of the increments based on the convergence evolution of previous increments.

Also, nonlinear static problems may become unstable. One of the possible sources of such instabilities is buckling. A model where buckling appears locally may not be resoluble using general solution methods. For this kind of cases, it becomes necessary to either solve the problem dynamically or with the aid of artificial damping.

Since the above situation represents what it is expected to be found in the model response, a constant artificial damping factor is used throughout the whole step to account for the appearance of local instabilities.

Automatic stabilization with a constant damping factor implies that viscous forces of the form:

$$F_v = c\mathbf{M}v \tag{4.1}$$

are added to the global equilibrium equations:

$$P - I - F_v = 0, \tag{4.2}$$

where I represents the internal forces, P the external forces, $\mathbf{M}$ is the artificial mass matrix calculated with unity density, c is the defined damping factor, $v = \Delta u/\Delta t$ is the vector of nodal velocities, and Δt is the increment of simulation time.

The final value of c that is going to be used during the simulations is chosen after performing a small parametric study of the different possibilities. As a result, the plot shown in Figure **??** is produced. This plot represents the evolution of the twist at the tip as the load is increased step by step during the nonlinear simulation. As it will be explained in Section **??**, the use of automatic stabilization becomes

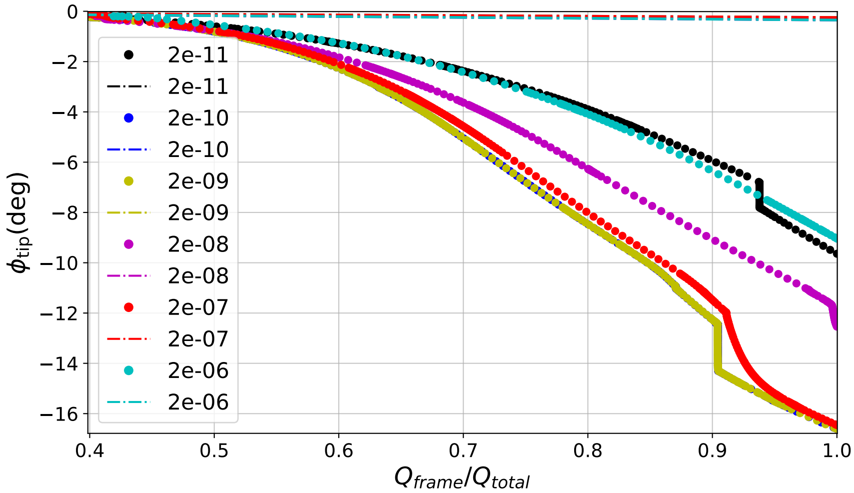

Figure 4.19: Displacement-force curve for various values of constant artificial damping factor.

necessary to capture the dynamics that involve buckling on the chiral ligaments and the ultimate collapse of the structure.

As it can be seen in the mentioned figure, all the different values of the damping factors success to capture the rapidly change in tip twist that occurs for fractions of load applied $> 60\%$. However, special care needs to be taken in order to ensure that the inclusion of artificial damping factor is not leading to inaccurate results due to over-damping of the structure. This can be done by comparing the fraction of the static energy that it is dissipated compared with the external work that its put into the system. This is done for a values of $c = 2 \times 10^{-5}$, $c = 2 \times 10^{-8}$ and $c = 2 \times 10^{-9}$ in Figures **??**, **??** and **??**, respectively. In these plots, the moment where the structure collapses due to the buckling phenomena occurring on the chiral ligaments can be seen as a sudden change in the slope of both curves. Here it can be seen that for the case of $c = 2 \times 10^{-5}$, the slope of the curve showing the energy dissipated through artificial stabilization is positive after the onset of buckling, which is a sign of over-damping in this region. On the other hand, for the case of $c = 2 \times 10^{-8}$, the slope remains of the curve remains zero. Finally, for the case of $c = 2 \times 10^{-9}$, the slope also remains zero and the final value for the energy dissipated is smaller than for $c = 2 \times 10^{-8}$.

Finally, since the objective is to capture the dynamics that involve buckling on the chiral ligaments and the ultimate collapse of the structure, keeping the energy dissipated a small as possible fraction of the external work, it is decided to use constant damping factor $c = 2 \times 10^{-9}$ for the simulations perform ahead.

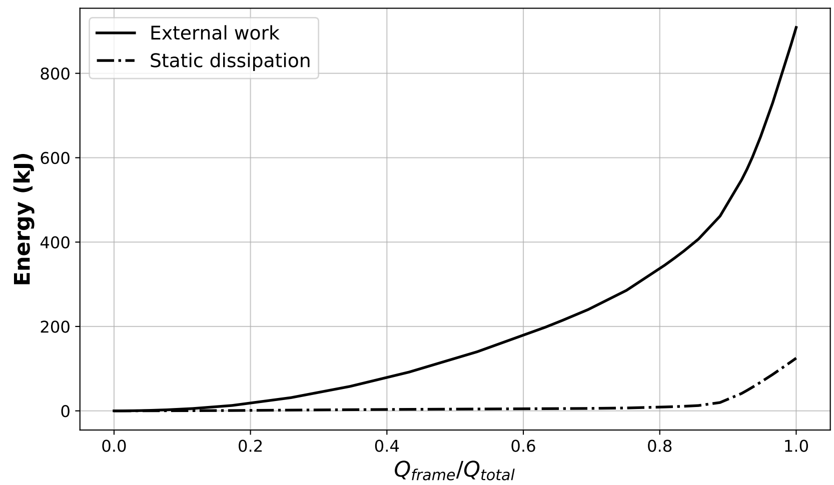

Figure 4.20: External work and static dissipation for a damping factor equal to 2×10^{-5}. The positive slope of the curve showing the energy used in the static dissipation is a sign of over-damping.

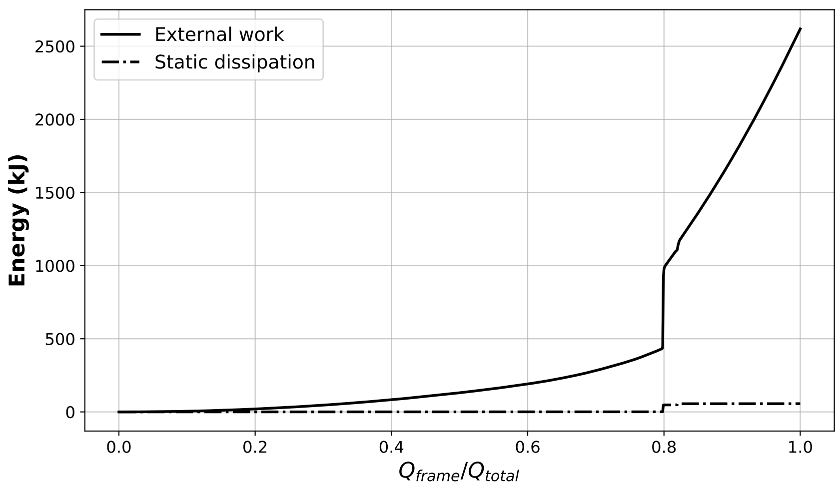

Figure 4.21: External work and static dissipation for a damping factor equal to 2×10^{-8}. After the structure collapse the static dissipation energy remains constant and small compared with the external work introduced into the system.

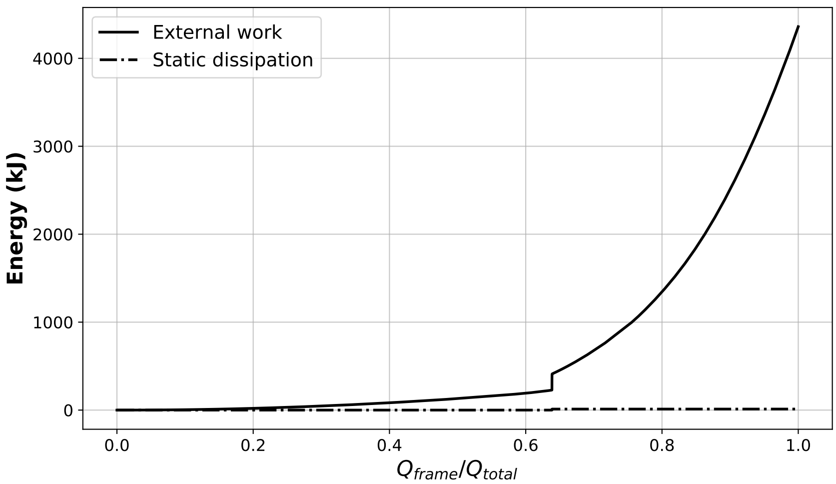

Figure 4.22: External work and static dissipation for a damping factor equal to 2×10^{-9}. After the structure collapse the static dissipation energy remains constant and negligible compared with the external work introduced into the system.

4.2.5 Ribs

As explained in Subsection **??**, two different designs were developed for the rib, one consisted in a open profile and the other one was a closed profile. A first set of simulations were executed for the option of one open section at the rib at the tip. In Figure **??**, it can be seen an example of the response seen for this type of configuration after a prescribed load of 800 N has been applied. It can be seen that, under the prescribed load, the rib is closing its profile and the upper flange shows a bigger displacement v compared with the lower flange.

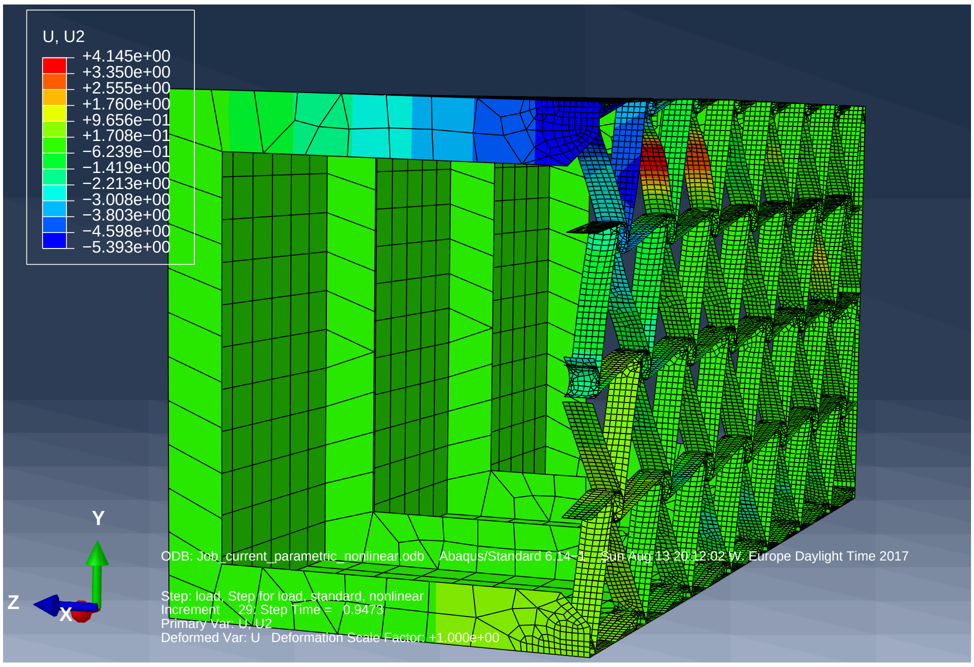

Figure 4.23: Vertical displacement v at the tip rib. The colour contour shows those mesh nodes located on the upper flange of the rib have a higher v, therefore showing how the rib is closing under the prescribed load (800 N)

In an attempt to avoid a deformation in the rib that causes the rib to close, it was decided to use ribs with a close profile. The simulations then provided a solution like the one shown in Figure **??**. For this case, the initial buckling occurs in ligaments located far from the root. The twist of the beam, measured as the rotational displacement u around the x axis is of approximately 0.3 deg. The prescribed load was -800 N and the simulation converged to the 0.95% of the prescribed load.

In order to investigate further deformations of the ligaments, it was decided to carry out simulations that incorporate automation stabilization through artificial damping artificial damping factor, as it was explained in Subsection **??**. After this, the results showed a deformation like the one shown in Figure **??**. This figure shows how big local deformations appear on the wing-box upper skin for this case. Also, it can be seen that the buckling phenomena has moved backwards to the ligaments close to the root.

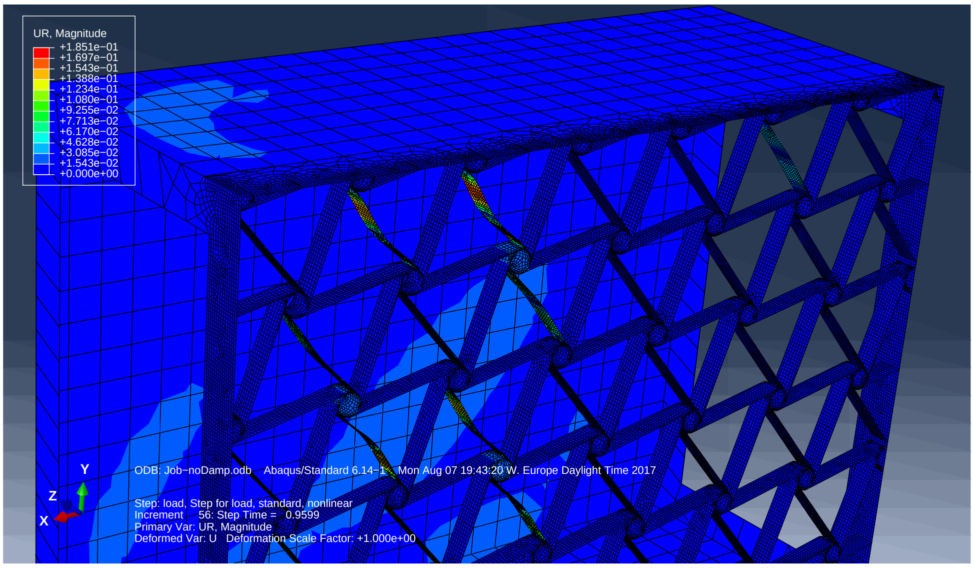

Figure 4.24: Model response without the use of inner ribs nor automatic stabilization.

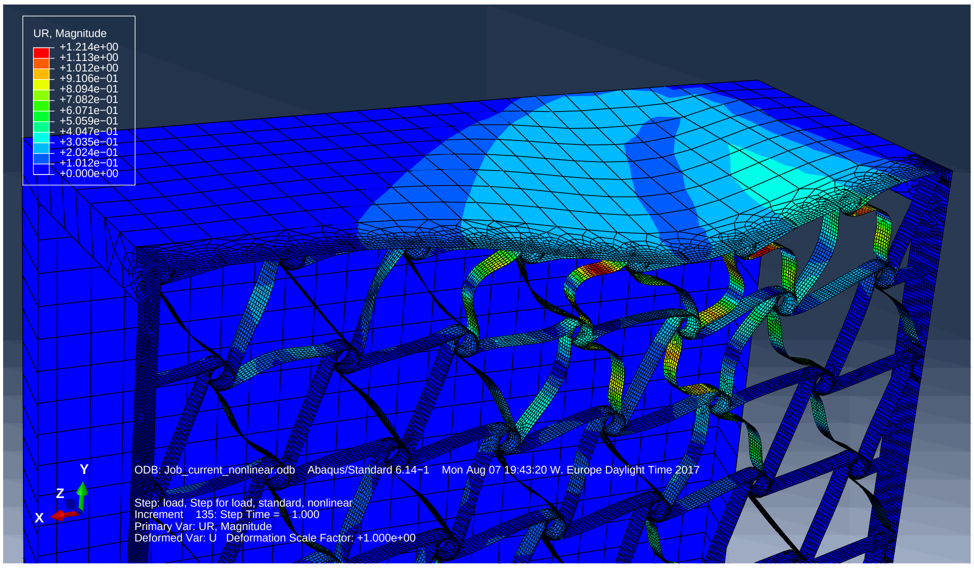

Figure 4.25: Model response without the use of inner ribs and with automatic stabilization.

In order to reduce the local deformations occurring on the wing-box, a pair of inner ribs as described in Subsection **??** were added to the model. This element added stiffness to the structure in bending. Now, the response of the model was shown to be like the one represented in Figure **??**. Here it can be seen that the ligaments that start to buckle are located at the same position as they were in the response of the model that did not incorporate inner ribs seen in Figure **??**. However, now the degree of deformation has decreased due to the stiffness added to the structure as a result of the inner ribs addition.

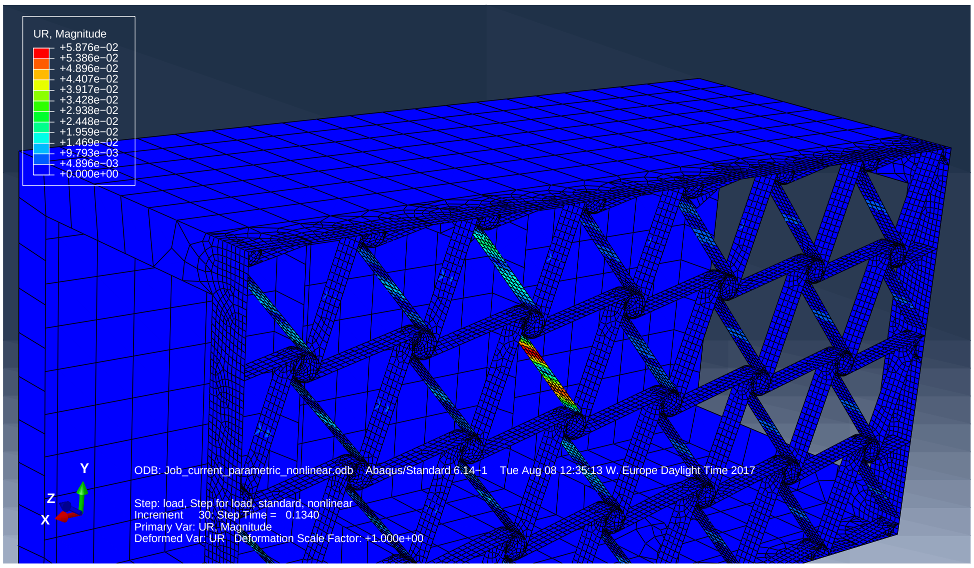

Figure 4.26: Model response incorporating inner ribs and without automatic stabilization

However, for this last case, the simulation was only able to converge up to 13% of the prescribed load. In other to progress further in the analysis, the use of automatic stabilization becomes necessary again. For this reason, in the final configuration, automatic stabilization through constant damping factor will be used together with the inner ribs. A description of the response of the structure for this last case is presented on next chapter.

Chapter 5

Simulations results

In the present chapter, the results obtained from the simulations completed in Abaqus CAE are presented. Firstly, the general response of the structure is characterized for the baseline configuration. A description of the elastic instability that the chiral ligaments undergo is included. Also, the nonlinear response in twist angle of the structure is shown.

Secondly, the results obtained from the parametric study performed are presented. Here, the influence of each of the parameters on the nonlinear response in twist of the structure and the buckling phenomena are shown.

5.1 General response characterization

In this section, the general response of the model is characterized. For the wing-box, the nominal value of its characteristic parameters are those shown in Table **??**, while Tables **??** and **??** contain the nominal values of the main parameters for the chiral lattice and the ribs, respectively. Also, the baseline configuration will incorporate a pair of inner ribs and the load will be applied on a single mesh node on the upper flange of the tip rib, as described in Subsection **??**.

In the simulations, automatic stabilization artificial through constant damping factor is included. For this case, the response of the structure when 47% of the prescribed load has been applied is the one shown in Figure **??**. It can be seen that buckling starts at the tip region of the lattice. Several lattice have started to buckle as an initial response to the load. However, in a further load increment, buckling phenomena moves backwards and those ligaments located close to the root and at a higher y coordinate, start to deform even more severely. At this point, when 47% of the prescribed load has been applied, the structure collapses and the twist increases for smaller increments in the applied load. This can be seen in Figure **??**.

This is the point at which the local instabilities are such that there is need of adding artificial damping

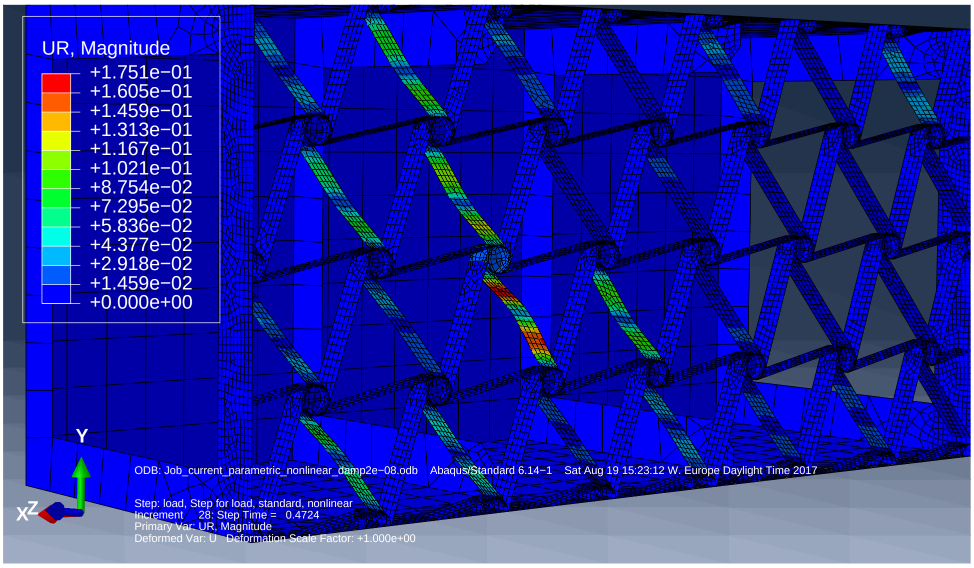

Figure 5.1: Baseline model response when the fraction of load applied equals to 47% of the prescribed load (700 N). Buckling has appeared at the tip of the wing-box due as an initial response to the load that it is being introduced.

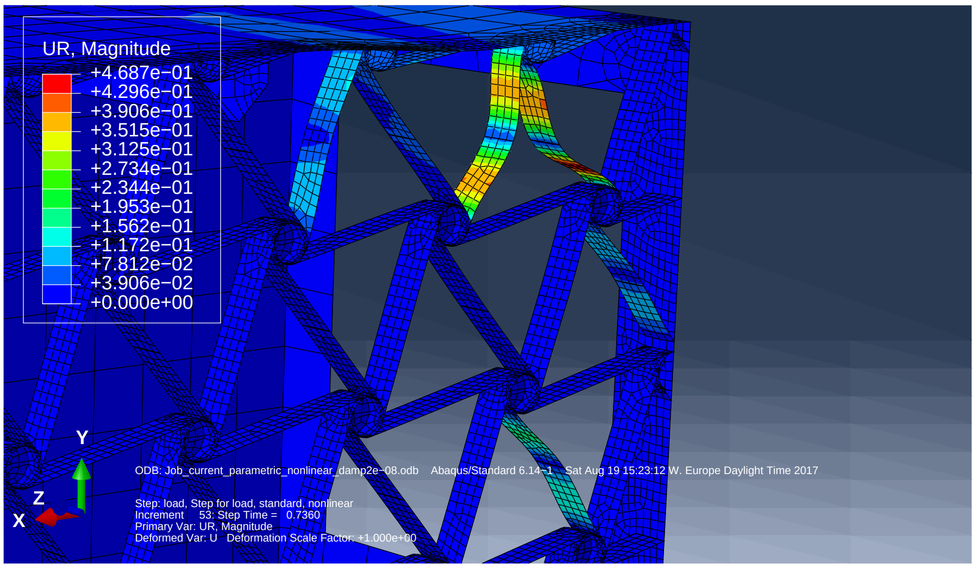

Figure 5.2: Baseline model response when the fraction of load applied equals to 73% of the prescribed load (700 N). Severe buckling deformation appears in those chiral ligaments located at the root and with a higher y coordinate. This is the point when the structure collapses and the twist increases for smaller increments in the applied load.

factor in order to capture the structure dynamics. After this point, the artificial damping allows the simulation to continue. As it was explained in Subsection **??**, special care needs to be taken to ensure that the inclusion of artificial damping factor is not leading to inaccurate results due to over-damping of the structure. This can be done by comparing the fraction of the static energy that it is dissipated with to the external work that its put into the system. The Figure **??** makes this comparison possible. It can be seen that effectively, the static dissipation through automatic stabilization is negligible in comparison with the external work. This figure also shows the abrupt increment in external work at the point where the structure collapses due to sudden buckling of the chiral ligaments.

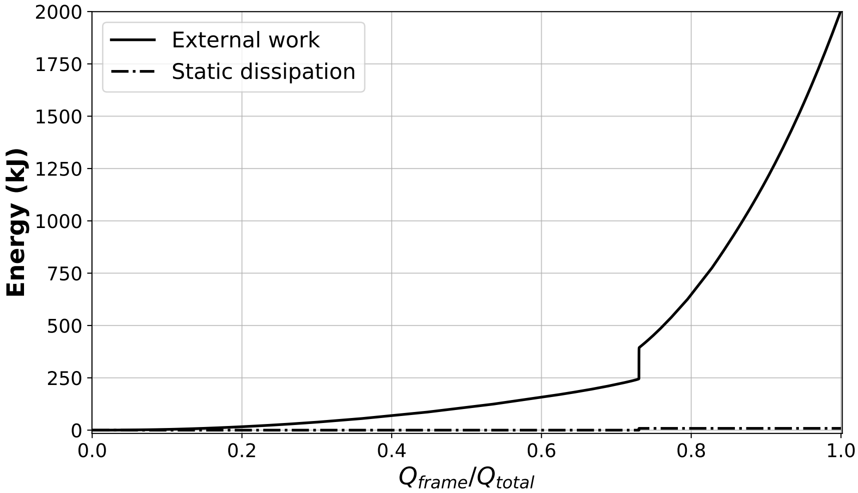

Figure 5.3: External work and static dissipation for a simulation of the baseline configuration. It can be seen that the static dissipation through automatic stabilization is negligible in comparison with the external work showing that the inclusion of artificial damping factor is unluckily to be leading to inaccurate results. The abrupt change in the external work shows the point where structure collapses due to sudden buckling of the chiral ligaments.

In order to see the overall system response as load increases, a displacement-force curve can be plotted. The Figure **??** shows the typical twist variation as the load is increased. On this plot, the results from the nonlinear simulations are shown as the set of scatter points while the dotted line represents the forecast final twist from the linear simulation. In the case shown, the linear simulation arises a twist at the tip ϕ_{tip} equal to -0.196 degrees while the nonlinear simulation predicts a final twist of -1.248 degrees. This shows how the problem under study is highly nonlinear.

The nonlinear response also shows the point where the structure collapses that its located at the point where approximately 73% of the load has been applied. The deformation state of the structure at this point was the one shown in Figure **??**. In a further stage of the simulation, the structure enters the post-buckling regime and the instabilities propagate to other parts of the lattice chiral structure, as it can be seen in Figure **??**. Here it can be seen that the instabilities are more generalized and buckling appears in more ligaments apart from those at the root. Under certain conditions, this generalized state can produce a second sudden variation in the slope of the displacement-force curve, showing a third effective stiffness.

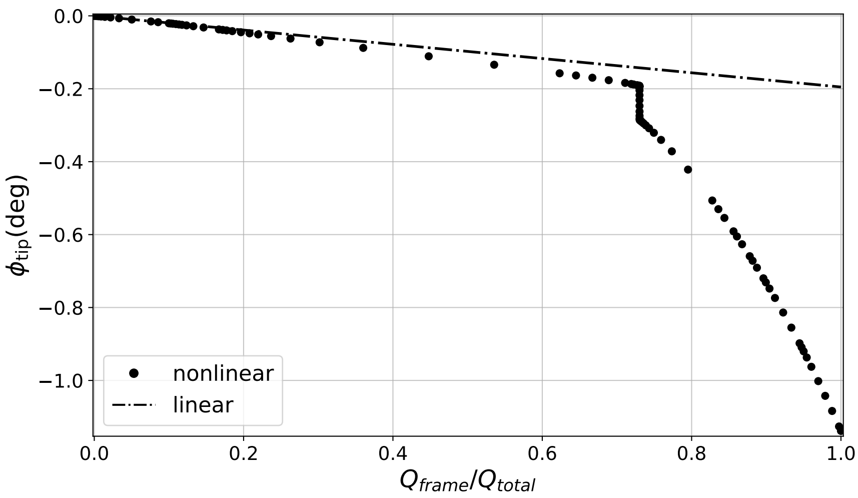

Figure 5.4: Displacement-force curve for the baseline configuration. Two breakdowns for the buckling deformation are shown in the plot. The first one is located at the point where the fraction of applied load equals to 73% and the second one at the point where the fraction is 96%.

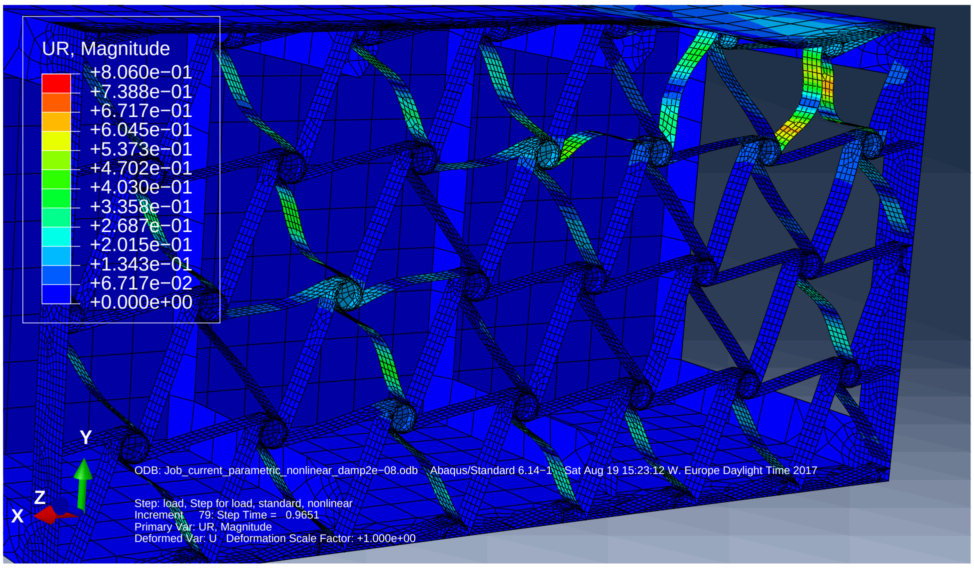

Figure 5.5: Baseline model response when the fraction of load applied equals to 96% of the prescribed load (700 N). In this case, not only the ligaments located at the root show severe buckling but also, other located at different points of the chiral lattice has started to buckle at the same time, inducing rapidly growing deformation for small increments in load.

5.2 Parametric study on the computational model

The aim of this section is to show the effect of each parameter on the nonlinear response of the structure. The parameters that will be included in the analysis are the following:

- Wing-box thickness t_{box}
- Number of unit cells in the transversal direction M
- Number of unit cells in the spanwise direction N
- Chiral node depth B_{chi}
- Chiral node radius r_{chi}
- Chiral lattice thickness t_{chi}
- Chiral ligament half length L_{chi}
- Dimensionless ligament eccentricity ε_{chi}

5.2.1 Wing-box thickness

In the present subsection the effect of different values for the wing-box thickness t_{box} on the structure response is investigated. The geometric representation of the wing-box thickness t_{box} can be seen in Figure **??**.

The results from the simulations carried out can be seen in Table **??**. In the table, the twist at the tip of the wing-box for the Abaqus nonlinear simulation ϕ_{tip} and for the linear simulation $\tilde{\phi}_{\text{tip}}$ are shown. This result is obtained by evaluating the value of the angular deformation u at a number of mesh elements located in different parts of the beam, as explained in the Subsection **??**. Therefore, the maximum deviation from the calculated mean twist has also been included. Finally, the Table **??** also shows the maximum vertical displacement found in the nodes located on the upper wing-box skin.

The evolution of the twist as a function of the load applied can be seen in Figure **??** for each of the values of t_{box} studied. It can be seen that the structure collapses for the cases of t_{box} = 0.6 mm, t_{box} = 0.8 mm and t_{box} = 1.0 mm, when the load applied reaches 40%, 64% and 97% of the total applied load, respectively. This result already shows the relevance of the wing-box thickness t_{box} in the triggering of the collapsing buckling. A detailed view of the nonlinear response of the structure for the different analysed cases is shown in Figure **??**. Here, the difference between the linear and the nonlinear is represented and it can be seen that the gap between the two responses increases as the value of t_{box} decreases. In the Table **??**, comparing the values of ϕ_{tip} and $\tilde{\phi}_{\text{tip}}$ provides information of the huge difference in the final value of the twist between the nonlinear and the linear response when the buckling occurs and it is captured in

t_{box} (mm)	ϕ_{tip} (deg)	$e(\phi_{\text{tip}})(\%)$	$\tilde{\phi}_{\text{tip}}$ (deg)	$e(\tilde{\phi}_{\text{tip}})(\%)$	v_{max}	$\hat{z}_{v_{\text{max}}}$	$\hat{x}_{v_{\text{max}}}$	
0.6	-14.331	11.13	-0.27	-14.259	0.121	-85.506	1	0.971
0.8	-1.934	11.43	-0.223	-15.178	0.546	-15.915	1	0.334
1	-0.403	14.651	-0.2	-19.923	0.546	-4.741	1	0.334
1.2	-0.221	15.031	-0.178	-21.074	0.121	-1.246	1	0.971

Table 5.1: Results from parametric study on the wing-box thickness t_{box}. The results show the mean twist at the tip of the wing-box for the Abaqus nonlinear simulation ϕ_{tip} and for the linear simulation $\tilde{\phi}_{\text{tip}}$. The maximum relative error of the mean calculation, expressed as percentage, for these two magnitudes is $e(\phi_{\text{tip}})$ and $e(\tilde{\phi}_{\text{tip}})$, respectively. The table also shows the maximum vertical displacement v_{max} among all the mesh nodes located on the upper skin of the wing-box and the dimensionless position in the spanwise direction $\hat{x}_{v_{\text{max}}}$ and in the chordwise direction $\hat{z}_{v_{\text{max}}}$ of the node that shows $v = v_{\text{max}}$.

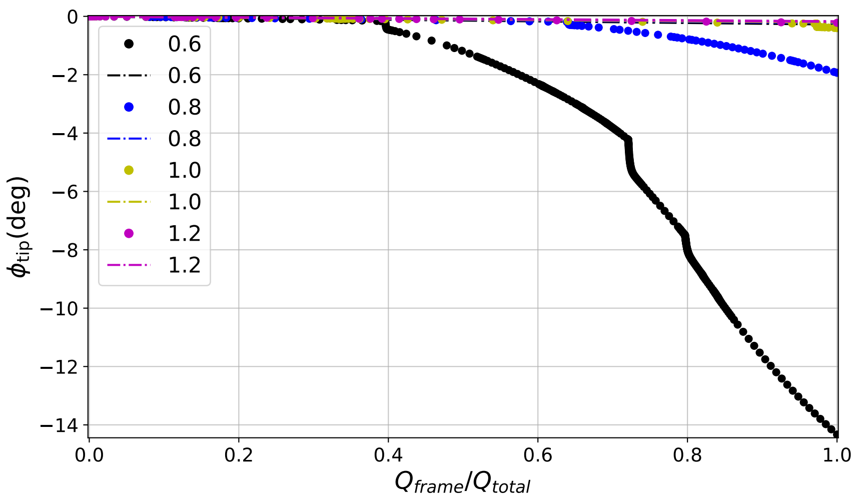

Figure 5.6: Displacement-force curve for various values of the wing-box thickness t_{box}. For all the cases shown, the force applied was located on the upper flange of the tip rib and its magnitude was equal to -800 N.

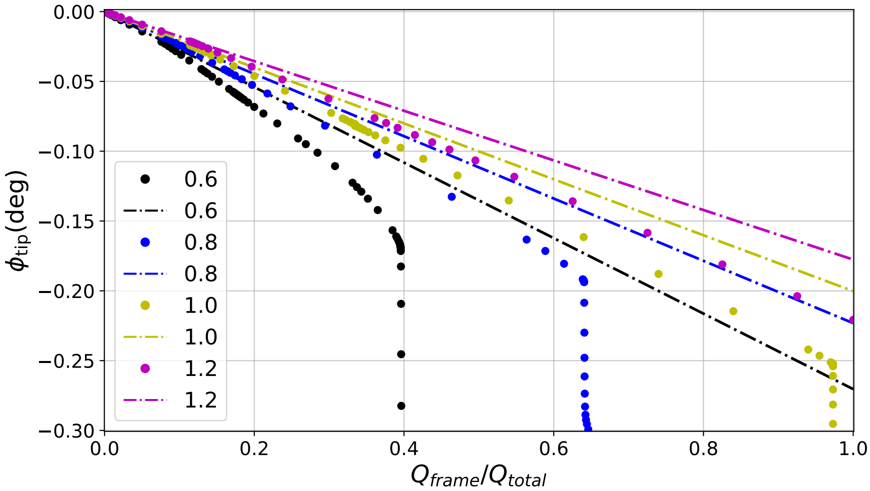

Figure 5.7: Detail of the displacement-force curve for various values of the wing-box thickness t_{box}. For all the cases shown, the force applied was located on the upper flange of the tip rib and its magnitude was equal to -800 N.

the simulation. For example, for $t_{\text{box}} = 0.8$ mm, the value of the tip twist from the linear simulation $\tilde{\phi}_{\text{tip}}$ is a 12% of the value estimated from the nonlinear simulation ϕ_{tip}.

The differences in response for the different cases are also visually evaluated using colour contour plots provided by Abaqus visualization module. The deformation in the ligaments for $t_{\text{box}} = 1.2$ mm when buckling occurs is shown in Figure **??** that shows the total rotational displacement of the mesh elements on the colour contour. It can be seen that buckling does not propagate to other parts of the lattice and it stays where it had appeared on first place, at the first ligaments after the inner rib located further from the root. In this case, the value of $t_{\text{box}} = 1.2$ mm makes the structure really stiff in bending and therefore, buckling does not appear at the root causing the structure collapse.

On the other hand, in Figure **??** the same plot is shown for a value of wing-box thickness of $t_{\text{box}} = 0.8$ mm, after all the prescribed load (800 N) has been applied. This figure shows how severe deformation due to buckling are occurring in the ligaments at the root. It is possible to see that some local deformation has been induced into the upper skin of the wing-box in between the root and the first inner rib. As shown in Table **??**, for the case $t_{\text{box}} = 0.8$ mm, the point with the maximum vertical is shown to appear close to the root, where $\hat{x}_{v_{\max}} = 0.334$.

Finally, for the case of $t_{\text{box}} = 0.6$ mm, it can be seen that the collapse of the structure occurs when just 40% of the prescribed load has been applied. Then, in Figure **??**, a second change in the slope of the force-displacement curve occurs when approximately 72% of the prescribed load has been applied. This second stage of the collapse of the structure appears when the elastic instabilities propagate from the ligaments at the root to other ligaments located closer to the tip of the structure. In Figure **??**, this generalized buckling can be seen at the moment when the second change in the slope of the force-deformation curve occurs. All those ligaments that have just started to deform cause the structure to sudden increase the twist deformation for the second time.

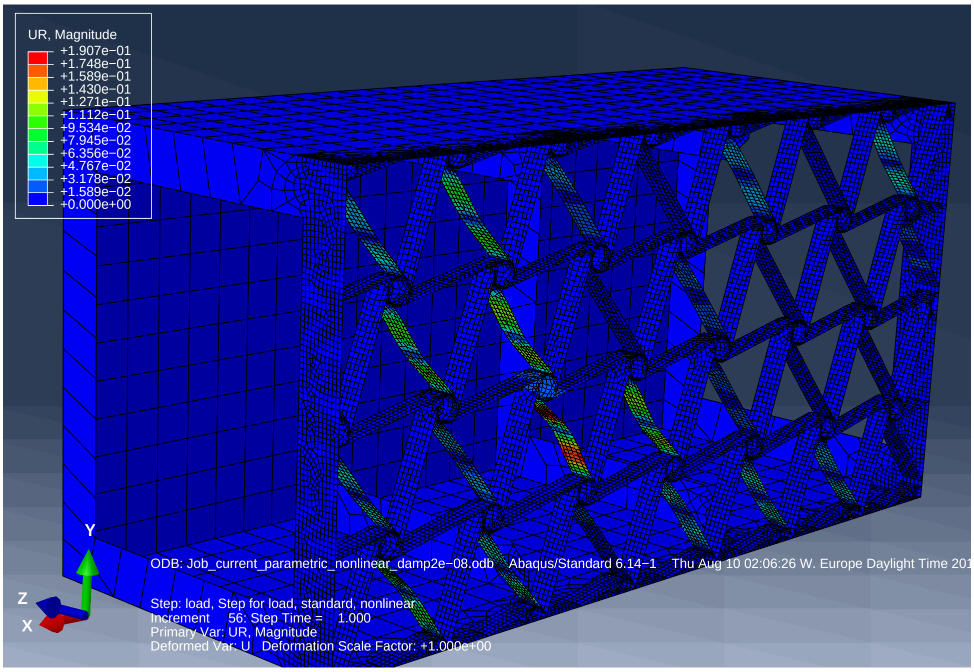

Figure 5.8: Color contour representation of the total angular displacement of the mesh elements on the deformed structure for $t_{\text{box}} = 1.2$ mm. This case is shown after all the prescribed load (800 N) has been applied. The elastic instabilities had appeared at the wing tip and they have not propagated to the rot causing the structure collapse.

A further study was performed in order to see the relationship between the wing-box thickness and the value of the force applied that induces the structure to collapse. As a result, the plot shown in Figure **??** was produced. It can be seen that relatively small variations in t_{box} produce considerable increment in the load required to trigger the buckling-induced twist morphing of the wing-box, as it has been already mentioned. For example, for $t_{\text{box}} = 0.6$ mm, 300 N for force are needed while for $t_{\text{box}} = 0.8$ mm the magnitude of the force required raises up to 525 N.

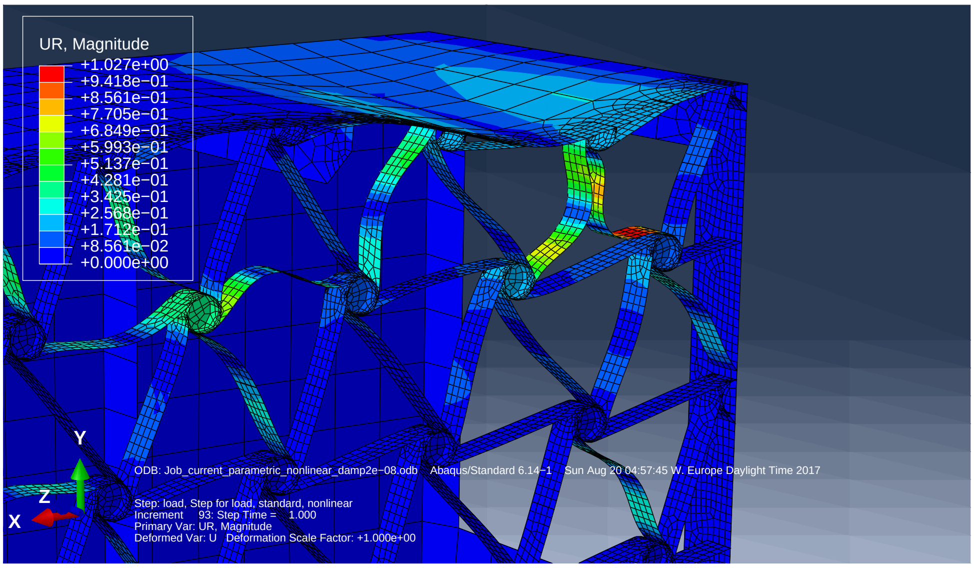

Figure 5.9: Color contour representation of the total angular displacement of the mesh elements on the deformed structure for $t_{\text{box}} = 0.8$ mm. This case is shown after all the prescribed load (800 N) has been applied. The appearance of elastic instabilities at the ligaments at the root has induced the structure collapse and local deformation on the wing-box skin.

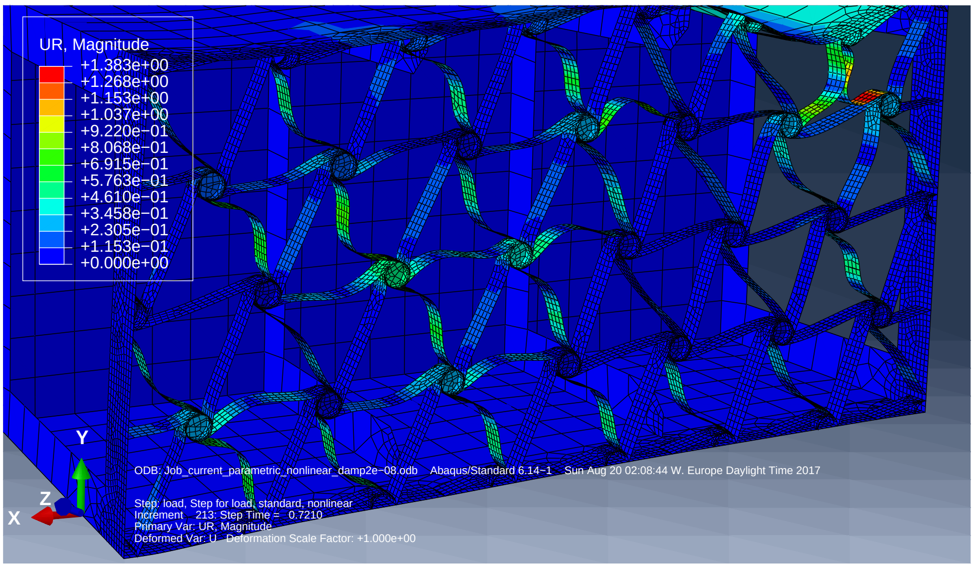

Figure 5.10: Color contour representation of the total angular displacement of the mesh elements on the deformed structure for $t_{\text{box}} = 0.6$ mm. This case is shown when 72% of the prescribed load (800 N) has been applied. The figure shows how the elastic instabilities have extended to the majority of the ligaments in the chiral lattice.

Figure 5.11: Force that induces the structure to collapse as a function of the wing-box thickness t_{box}.

5.2.2 Number of unit cells in the chiral lattice

Now the effect of the number of units cells in the transversal direction M and in the spanwise direction N on the structural response is investigated. These two parameters are responsible of the height and the length of the wing-box, respectively. The division of the chiral lattice in in M units cells in the transversal direction and in N units cells in the spanwise direction can be seen in Figure **??**.

Firstly, the number of unit cells in the transversal direction M is varied. This parameter modifies the height of the model. Similarly as it was done for the study of the wing-box thickness t_{box} influence in the structure response, the results from the different simulations are shown in Table **??**. Also, the displacement-force curve is shown in Figure **??**. It can be seen from the results that increasing M resulted on a decrement of the structure sensitivity to buckling. In order to be able to onset the elastic instabilities for $M > 3$, the simulations are executed for a prescribed load of 1200 N.

M	ϕ_{tip} (deg)	$e(\phi_{\text{tip}})(\%)$	$\tilde{\phi}_{\text{tip}}$ (deg)	$e(\tilde{\phi}_{\text{tip}})(\%)$	v_{max}	$\hat{z}_{v_{\text{max}}}$	$\hat{x}_{v_{\text{max}}}$
3	-9.672	11.43	-0.335	-15.177	-55.962	1	0.971
4	-1.221	18.13	-0.289	-24.409	-11.467	1	0.546
5	-0.385	15.3	-0.267	-21.211	-1.747	0.9	0.971

Table 5.2: Results from parametric study on the number of unit cells in the transversal direction M. The results show the mean twist at the tip of the wing-box for the Abaqus nonlinear simulation ϕ_{tip} and for the linear simulation $\tilde{\phi}_{\text{tip}}$. The maximum relative error of the mean calculation, expressed as percentage, for these two magnitudes is $e(\phi_{\text{tip}})$ and $e(\tilde{\phi}_{\text{tip}})$, respectively. The table also shows the maximum vertical displacement v_{max} among all the mesh nodes located on the upper skin of the wing-box and the dimensionless position in the spanwise direction $\hat{x}_{v_{\text{max}}}$ and in the chordwise direction $\hat{z}_{v_{\text{max}}}$ of the node that shows $v = v_{\text{max}}$.

From the results shown in Table **??** it can be seen how for the case of $M = 3$, the point that shows $v = v_{\text{max}}$ is located at the wing-box tip where $\hat{x}_{v_{\text{max}}} = 0.971$, due to the high twist of the structure. However, for $M = 4$, the location of the point with $v = v_{\text{max}}$ is at $\hat{x}_{v_{\text{max}}} = 0.546$ showing local deformation at this position. The value of the twist at the tip ϕ_{tip} has been reduced in 12% of what it was for $M = 3$. This shows that the structure increases its shear stiffness as the height of the wing-box increases. For $M = 5$, the structure is so stiff that v_{max} appears approximately at the point where the load is applied and the collapse of the structure does not occur. This shows that deformation is only achieved in the vicinity of the load introduction point due to the high stiffness in shear of the structure.

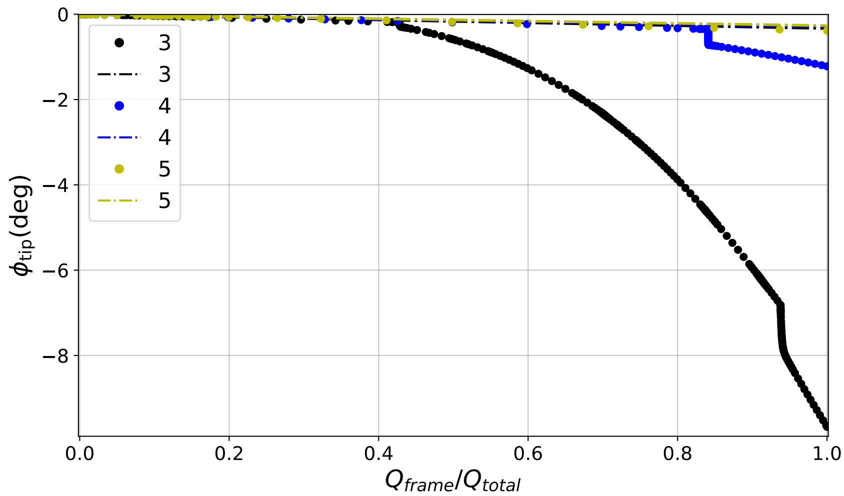

Figure 5.12: Displacement-force curve for various values of the number of unit cells in the transversal direction M. For all the cases shown, the load introduction point was located in the middle of the upper flange of the tip rib and its magnitude was equal to -1200 N.

The effects of the variation of the number of unit cells in the spanwise direction N, parameter responsible of the wing-box length, are investigated next. The results from the parametric study carried out are shown in Table **??**. The displacement-force curve for the simulations carried out is shown in Figure **??**. It can be seen that the bigger the wing-box length, the earlier that the buckling of the lattices cause the collapse of the structure.

In the last plot introduced it can be seen a second change in the slope of the curve for the cases of $N = 10$ and $N = 11$. This happens when, as explained in Section **??**, the buckling phenomena progresses from the ligaments at the root to be more generalized in other parts of the structure. This characteristic can be seen in Figure **??**, where the response of the structure for the case of $N = 10$ and load fraction of 81% is shown.

When plotting the force that makes the structure to collapse against the corresponding wing-box length, the Figure **??** is produced. In this graphic that for example, a force of 300 N is required to induce the collapse of a wing-box with length equal to 1000 mm.

N	ϕ_{tip} (deg)	$e(\phi_{\text{tip}})(\%)$	$\tilde{\phi}_{\text{tip}}$ (deg)	$e(\tilde{\phi}_{\text{tip}})(\%)$	$v_{\max}$	$\hat{z}_{v_{\max}}$	$\hat{x}_{v_{\max}}$
7	-0.215	13.74	-0.165	-18.212	-1.182	1	0.971
8	-1.596	14.222	-0.203	-18.444	-14.267	1	0.334
9	-3.419	9.419	-0.231	-12.654	-20.361	1	0.324
10	-10.516	7.756	-0.27	-10.353	-61.202	1	0.971
11	-22.16	6.466	-0.321	-8.819	-138.196	1	0.971
12	-31.558	5.316	-0.374	-7.222	-207.335	1	0.971

Table 5.3: Results from parametric study on the number of unit cells in the spanwise direction M. The results show the mean twist at the tip of the wing-box for the Abaqus nonlinear simulation ϕ_{tip} and for the linear simulation $\tilde{\phi}_{\text{tip}}$. The maximum relative error of the mean calculation, expressed as percentage, for these two magnitudes is $e(\phi_{\text{tip}})$ and $e(\tilde{\phi}_{\text{tip}})$, respectively. The table also shows the maximum vertical displacement $v_{\max}$ among all the mesh nodes located on the upper skin of the wing-box and the dimensionless position in the spanwise direction $\hat{x}_{v_{\max}}$ and in the chordwise direction $\hat{z}_{v_{\max}}$ of the node that shows $v = v_{\max}$.

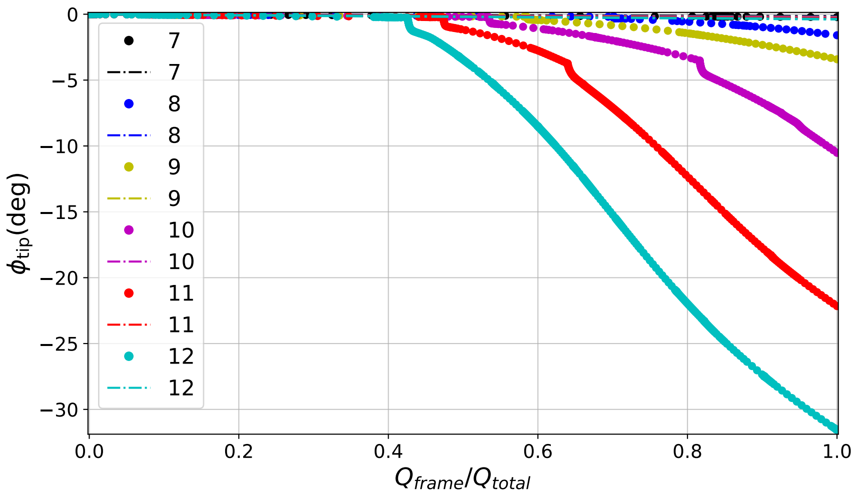

Figure 5.13: Displacement-force curve for various values of the number of unit cells in the spanwise direction N. For all the cases shown, the load introduction point was located in the middle of the upper flange of the tip rib and its magnitude was equal to -700 N.

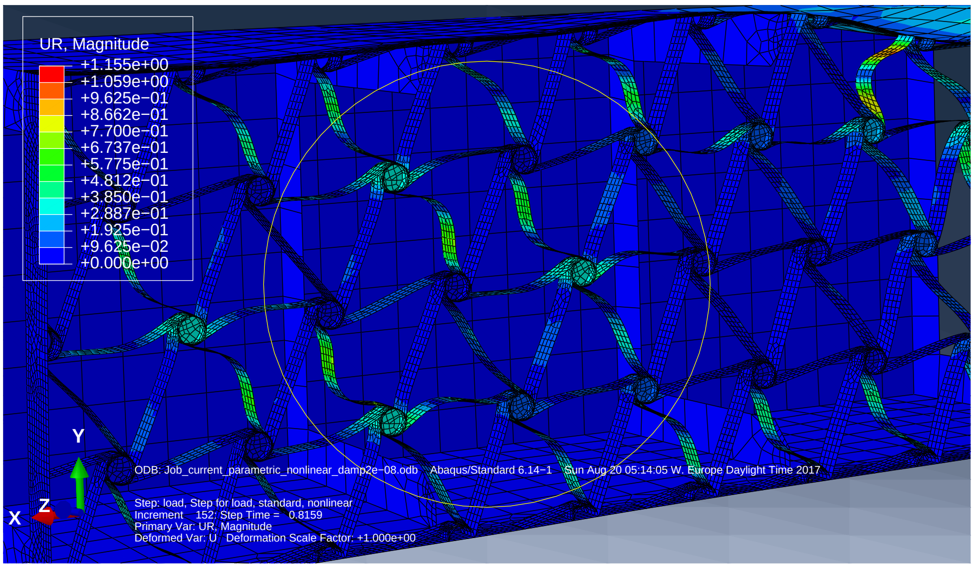

Figure 5.14: Model response when the fraction of load applied equals to 81% of the prescribed load (700 N) and $N = 10$. The plot shows how the buckling phenomena is generalized for the whole chiral structure.

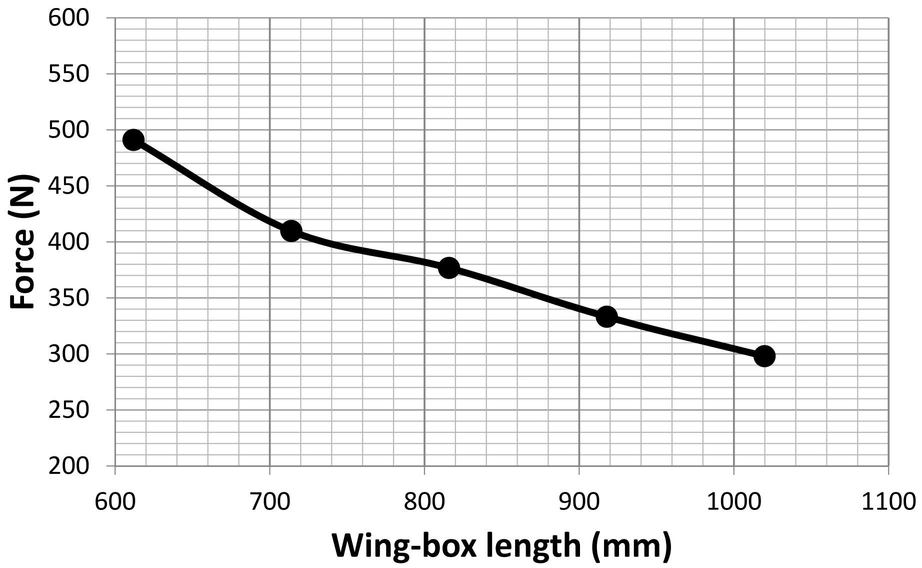

Figure 5.15: Force that induces the structure to collapse as a function of the wing-box length.

5.2.3 Chiral lattice parameters

In the present subsection, the following parameters of the chiral lattice structure are varied and its effect of the system response is shown:

- Chiral node depth B_{chi}
- Chiral node radius r_{chi}
- Chiral lattice thickness t_{chi}
- Chiral ligament half length L_{chi}
- Dimensionless ligament eccentricity $\varepsilon_{\mathrm{chi}}$

Dimensionless chiral ligament eccentricity $\varepsilon_{\mathrm{chi}}$

The first of the chiral parameter that is going to be studied is the ligament eccentricity e_{chi}, in its dimensionless form $\varepsilon_{\mathrm{chi}}$. The geometrical meaning of this parameter can be seen in the sketch shown in Figure **??**. The numeric results from the simulations carried out can be seen in Table **??**.

The force-deformation curve for the range of simulations carried out can be seen in Figure **??**. Here it can be seen that the collapse of the structure occurs for all the cases except for $\varepsilon_{\mathrm{chi}} = 0.1$. The deformation state of the structure for this case can be seen in Figure **??** that shows how the excessive eccentricity of the ligaments keep them from buckling and causing the structure collapse.

$\varepsilon_{\mathrm{chi}}$	ϕ_{tip} (deg)	$e(\phi_{\mathrm{tip}})(\%)$	$\tilde{\phi}_{\mathrm{tip}}$ (deg)	$e(\tilde{\phi}_{\mathrm{tip}})(\%)$	v_{max}	$\hat{z}_{v_{\mathrm{max}}}$	$\hat{x}_{v_{\mathrm{max}}}$
0	-0.372	12.092	-0.182	-13.82	-4.147	1	0.546
0.001	-1.194	11.467	-0.191	-15.24	-11.731	1	0.334
0.0015	-0.703	15.571	-0.16	-10.22	-7.122	1	0.546
0.01	-1.596	14.222	-0.203	-18.44	-14.267	1	0.334
0.05	-1.275	14.18	-0.223	-18.27	-12.298	1	0.334
0.1	-0.282	14.065	-0.229	-18.3	-2.044	1	0.334

Table 5.4: Results from parametric study on chiral ligament eccentricity $\varepsilon_{\mathrm{chi}}$. The results show the mean twist at the tip of the wing-box for the Abaqus nonlinear simulation ϕ_{tip} and for the linear simulation $\tilde{\phi}_{\mathrm{tip}}$. The maximum relative error of the mean calculation, expressed as percentage, for these two magnitudes is $e(\phi_{\mathrm{tip}})$ and $e(\tilde{\phi}_{\mathrm{tip}})$, respectively. The table also shows the maximum vertical displacement v_{max} among all the mesh nodes located on the upper skin of the wing-box and the dimensionless position in the spanwise direction $\hat{x}_{v_{\mathrm{max}}}$ and in the chordwise direction $\hat{z}_{v_{\mathrm{max}}}$ of the node that shows $v = v_{\mathrm{max}}$.

The Figure **??** also shows that the case of $\varepsilon_{\mathrm{chi}} = 0.0$, that is when the ligaments are flat, is not the case that shows a earlier onset of the instabilities, as it would be expected. Instead, for $\varepsilon_{\mathrm{chi}} = 0.0$, the structure shows the later onset of the instabilities, when the applied load is 96% of the prescribed load. On the

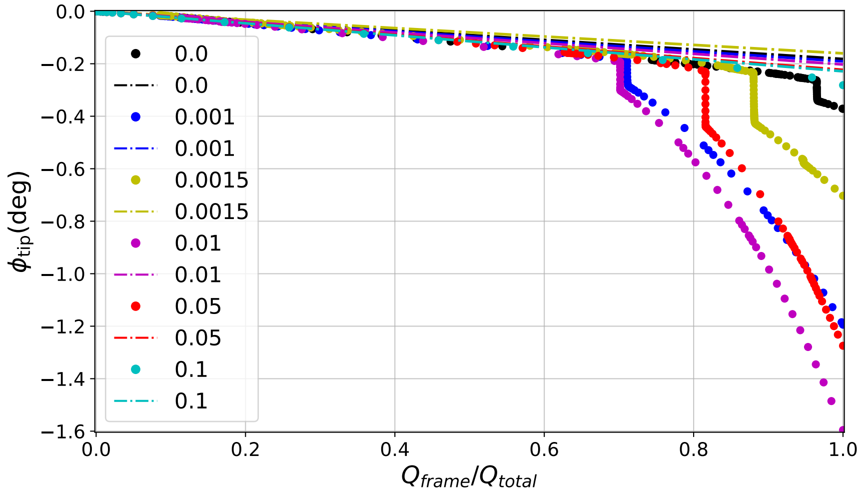

Figure 5.16: Displacement-force curve for various values of the dimensionless chiral ligament eccentricity ε_{chi}. The plot shows how the collapse of the structure occurs for all the cases except for $\varepsilon_{chi} = 0.1$..

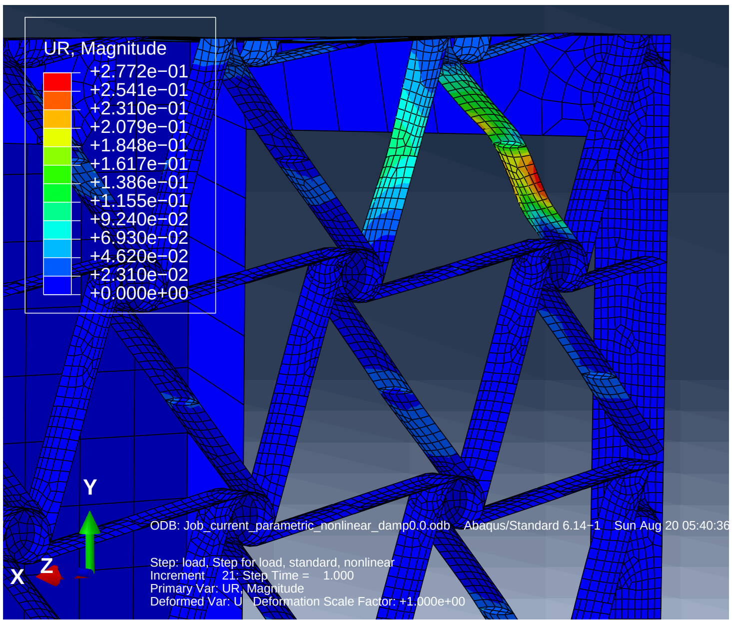

Figure 5.17: Model response when the fraction of load applied equals to 100% of the prescribed load (700 N) and $\varepsilon_{chi} = 0.1$. For this case, the excessive ligament eccentricity at the end of the simulation keeps it from buckling and causing the structure collapse.

other hand, the collapse of the structure is triggered when the applied load is 68% of the prescribed load for the case of $\varepsilon_{\mathrm{chi}} = 0.001$. This particular behavior is investigated by looking at the deformed plots on the Abaqus visualization module. In Figures **??** and **??** the deformed state of the ligaments at the point when collapse of the structure occurs is shown for the cases of $\varepsilon_{\mathrm{chi}} = 0.0$ and $\varepsilon_{\mathrm{chi}} = 0.001$, respectively. It can be seen that the buckling mechanism in the ligaments changes from case to case. In particular, it can be seen that for $\varepsilon_{\mathrm{chi}} = 0.0$ the onset of the instabilities induces some rotation to the lattice nodes located on the upper part. The particular geometry of the model is believed to be the reason behind this differences in the appearance of buckling at the ligaments at the root.

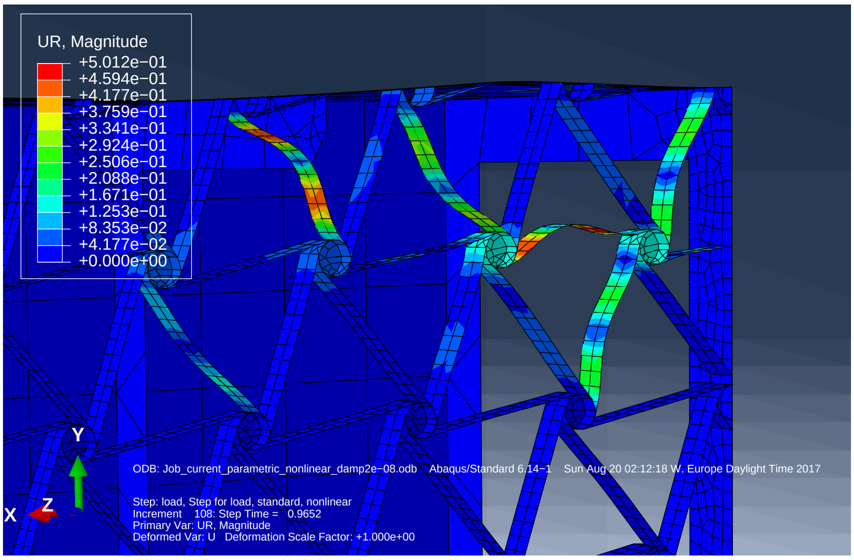

Figure 5.18: Model response when the fraction of load applied equals to 96% of the prescribed load (700 N) and $\varepsilon_{\mathrm{chi}} = 0.0$. In this case, the onset of the instabilities affect the rotation of the lattice nodes, in particular. There are two ligaments on the upper part that remain undeformed.

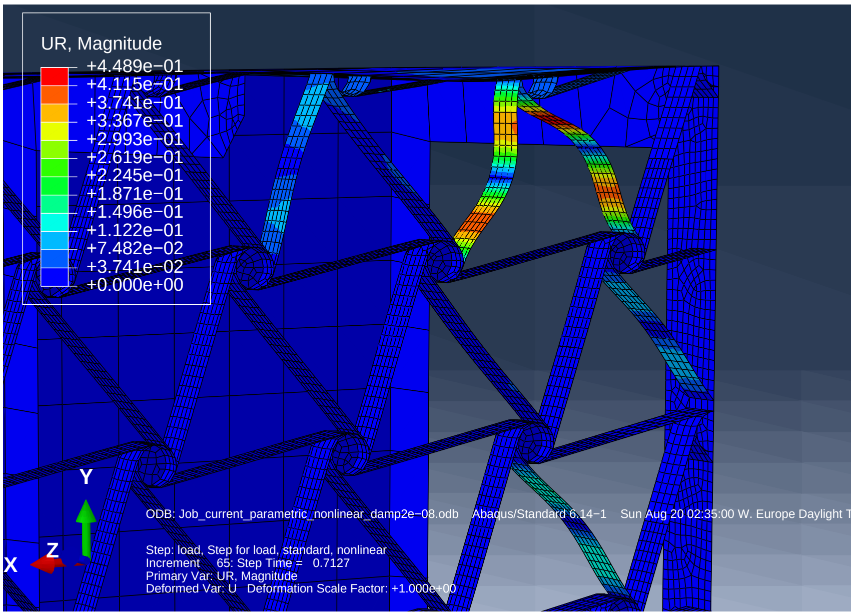

Figure 5.19: Model response when the fraction of load applied equals to 71% of the prescribed load (700 N) and $\varepsilon_{\mathrm{chi}} = 0.001$.

Chiral node depth B_{chi}

The numeric results from the parametric analysis on the chiral node depth B_{chi} can be seen in Table **??**. The geometrical meaning of this parameter can be seen in the sketch shown in Figure **??**. The displacement-force curve can be seen in Figure **??** for various values of B. This plot shows how the bigger B_{chi} is, the more abrupt the collapse is, showing a bigger sudden increment on the measured twist at the tip ϕ_{tip}.

The Figure **??** shows a colour contour plot representing the rotation u around the x direction of the mesh elements located on the upper skin of the wing-box and close to the root. This is represented for the case of $B_{\text{chi}} = 30$ mm, at the moment when collapse of the structure occurs which is at 86% of the prescribed load and in the area where local deformation of the skin takes place. Examination of the plot arises that the value of u in this area is approximately double to that corresponding to $B_{\text{chi}} = 10$ mm which can be seen in Figure **??**. This shows that the bigger B_{chi} is, the more area is affected by the ligaments deformation when buckling occurs and the greater the local deformation will be.

When plotting the force that makes the structure to collapse against the corresponding value of chiral node depth depth B_{chi}, the Figure **??** was produced.

B_{chi}	ϕ_{tip} (deg)	$e(\phi_{\text{tip}})(\%)$	$\tilde{\phi}_{\text{tip}}$ (deg)	$e(\tilde{\phi}_{\text{tip}})(\%)$	v_{max}	$\hat{z}_{v_{\text{max}}}$	$\hat{x}_{v_{\text{max}}}$
10	-1.399	11.421	-0.217	-15.359	-12.735	1	0.334
20	-1.596	14.222	-0.203	-18.444	-14.267	1	0.334
30	-0.707	16.454	-0.216	-24.477	-7.975	1	0.334

Table 5.5: Results from parametric study on chiral node depth B_{chi}. The results show the mean twist at the tip of the wing-box for the Abaqus nonlinear simulation ϕ_{tip} and for the linear simulation $\tilde{\phi}_{\text{tip}}$. The maximum relative error of the mean calculation, expressed as percentage, for these two magnitudes is $e(\phi_{\text{tip}})$ and $e(\tilde{\phi}_{\text{tip}})$, respectively. The table also shows the maximum vertical displacement v_{max} among all the mesh nodes located on the upper skin of the wing-box and the dimensionless position in the spanwise direction $\hat{x}_{v_{\text{max}}}$ and in the chordwise direction $\hat{z}_{v_{\text{max}}}$ of the node that shows $v = v_{\text{max}}$.

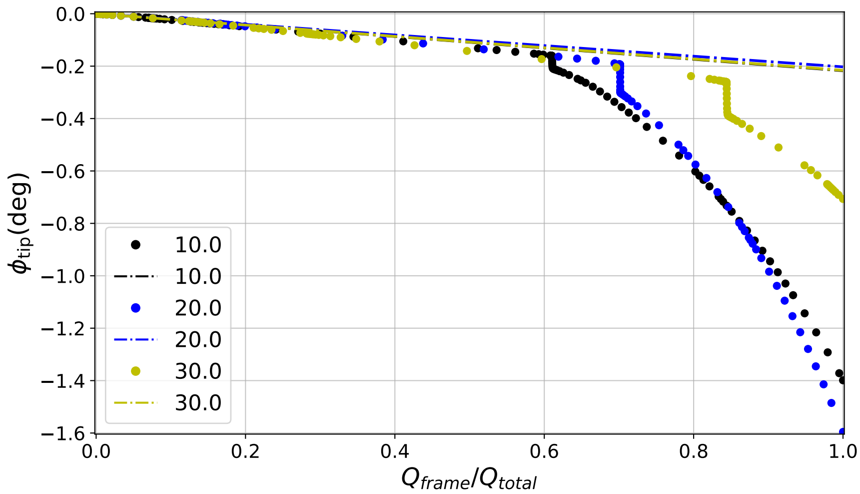

Figure 5.20: Displacement-force curve for various values of the dimensionless chiral node depth B_{chi}. Results show how the bigger the node depth B_{chi} is, the later the collapse of the structure occurs but the more abrupt is its.

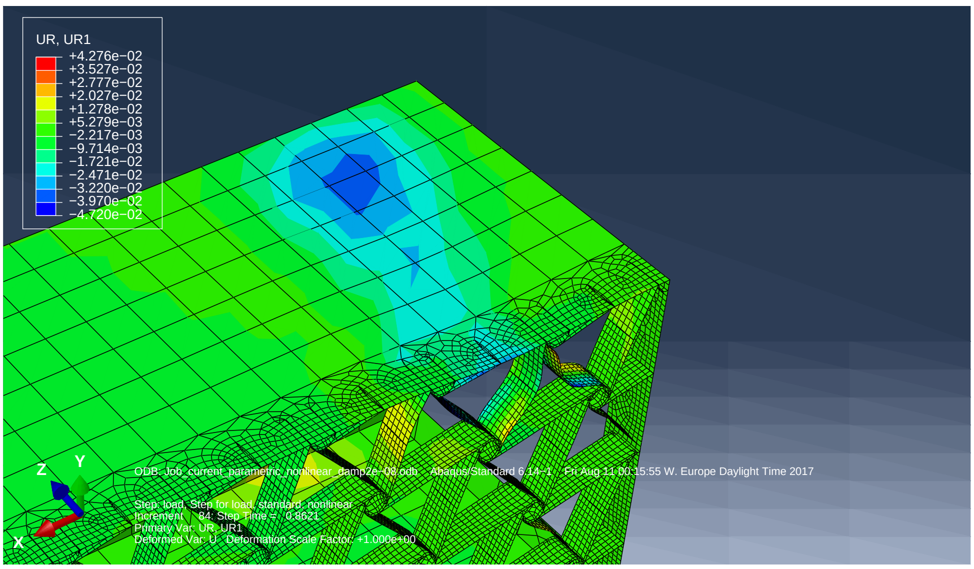

Figure 5.21: Model response when the fraction of load applied equals to 86% of the prescribed load (700 N) and $B_{\text{chi}} = 30$ mm. The plot shows a colour contour with the value of the rotational displacement u around the x direction at the moment in which the structure collapses. In the area where the local deformation occurs, the value of u is approximately equal to -0.033 rad.

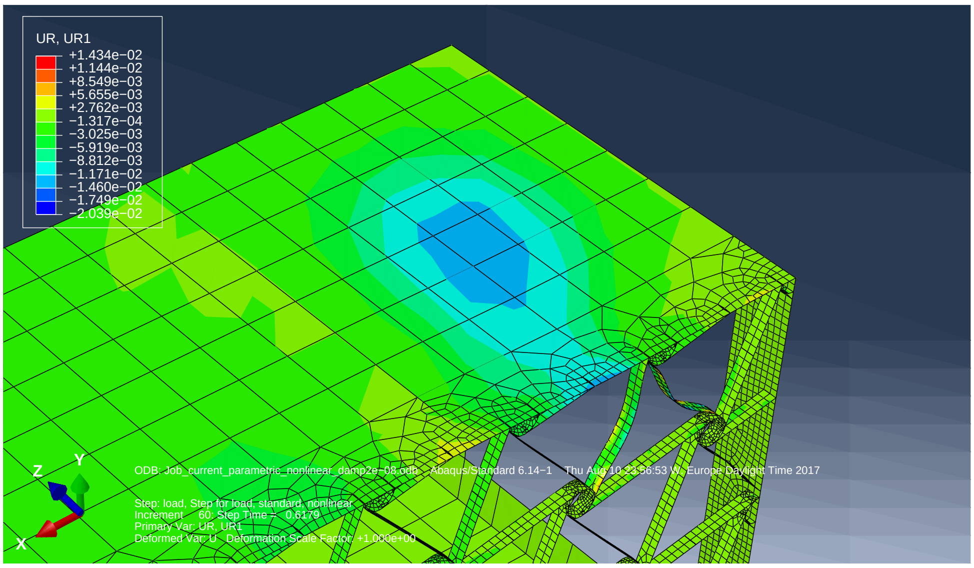

Figure 5.22: Model response when the fraction of load applied equals to 62% of the prescribed load (700 N) and $B_{\mathrm{chi}} = 10$ mm. The plot shows a colour contour with the value of the rotational displacement u around the x direction at the moment in which the structure collapses. In the area where the local deformation occurs, the value of u is approximately equal to -0.015 rad.

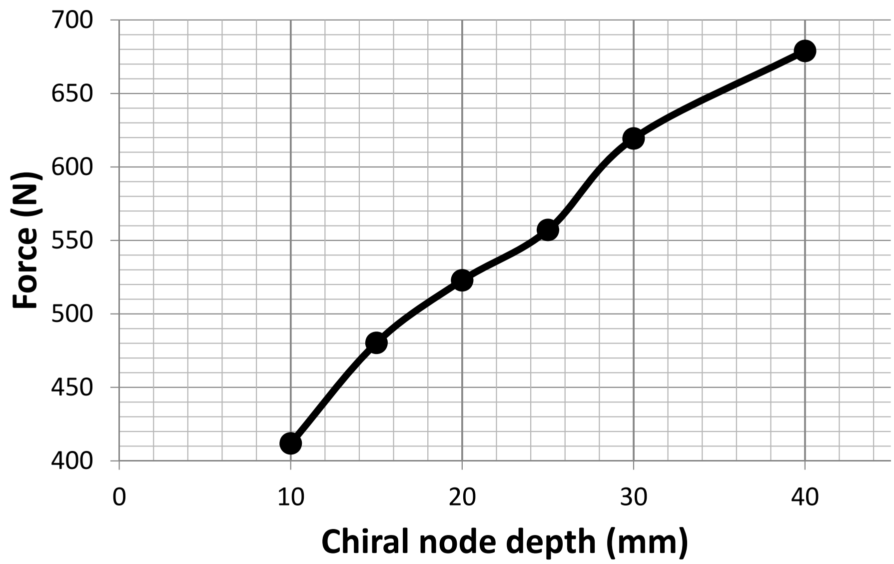

Figure 5.23: Force that induces the structure to collapse as a function of the chiral node depth B_{chi}.

Chiral node radius r_{chi}

A parametric study on different values of the chiral node radius r_{chi} is presented next. The geometrical meaning of this parameter can be seen in the sketch shown in Figure **??**. The possible values of r_{chi} are limited by the geometry of the chiral lattice. For values $r_{\text{chi}} \leq 5$ mm, it is not possible to build the mode due to interferences between the different ligaments that joined at each of the nodes. The numeric results from the simulations are presented in Table **??**.

The displacement-force curve obtained from the simulations is shown in Figure **??**. This curve shows how the structure collapses for analysed cases except for $r_{\text{chi}} = 17.5$ mm and $r_{\text{chi}} = 20$ mm. However, for the case of $r_{\text{chi}} = 17.5$mm, buckling do not occur on the ligaments located at the root but in those located just after the inner rib located closer to the root, with smaller x. This can be seen in Figure **??**. Then, the chiral node radius r_{chi} value shifts the position of the buckling ligaments that origin the collapse of the structure.

The variation of the force that makes the structure to collapse as a function of the chiral node radius r_{chi} can be seen in Figure **??**. It can be seen that, the smaller the chiral node radius r_{chi} is, the earlier the structure collapse occurs.

r_{chi}	ϕ_{tip} (deg)	$e(\phi_{\text{tip}})(\%)$	$\tilde{\phi}_{\text{tip}}$ (deg)	$e(\tilde{\phi}_{\text{tip}})(\%)$	v_{max}	$\hat{z}_{v_{\text{max}}}$	$\hat{x}_{v_{\text{max}}}$
7.5	-1.184	13.64	-0.171	-10.046	-11.586	1	0.331
10	-0.877	9.525	-0.17	-10.196	-9.831	1	0.334
12.5	-0.886	9.596	-0.17	-10.247	-10.051	1	0.337
15	-1.121	13.638	-0.173	-10.134	-11.677	1	0.342
17.5	-0.273	9.481	-0.171	-10.215	-4.169	1	0.568
20	-0.229	12.686	-0.171	-8.848	-1.433	1	1.026

Table 5.6: Results from parametric study on chiral node radius r_{chi}. The results show the mean twist at the tip of the wing-box for the Abaqus nonlinear simulation ϕ_{tip} and for the linear simulation $\tilde{\phi}_{\text{tip}}$. The maximum relative error of the mean calculation, expressed as percentage, for these two magnitudes is $e(\phi_{\text{tip}})$ and $e(\tilde{\phi}_{\text{tip}})$, respectively. The table also shows the maximum vertical displacement v_{max} among all the mesh nodes located on the upper skin of the wing-box and the dimensionless position in the spanwise direction $\hat{x}_{v_{\text{max}}}$ and in the chordwise direction $\hat{z}_{v_{\text{max}}}$ of the node that shows $v = v_{\text{max}}$.

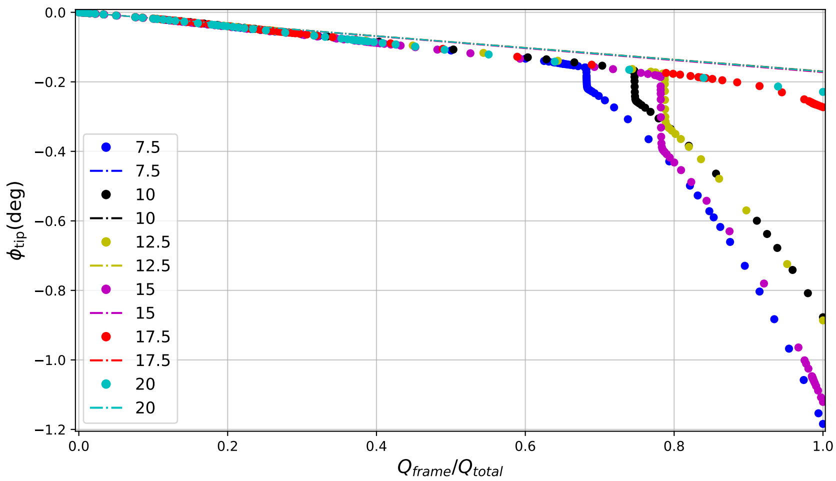

Figure 5.24: Displacement-force curve for various values of the chiral node radius r_{chi}.

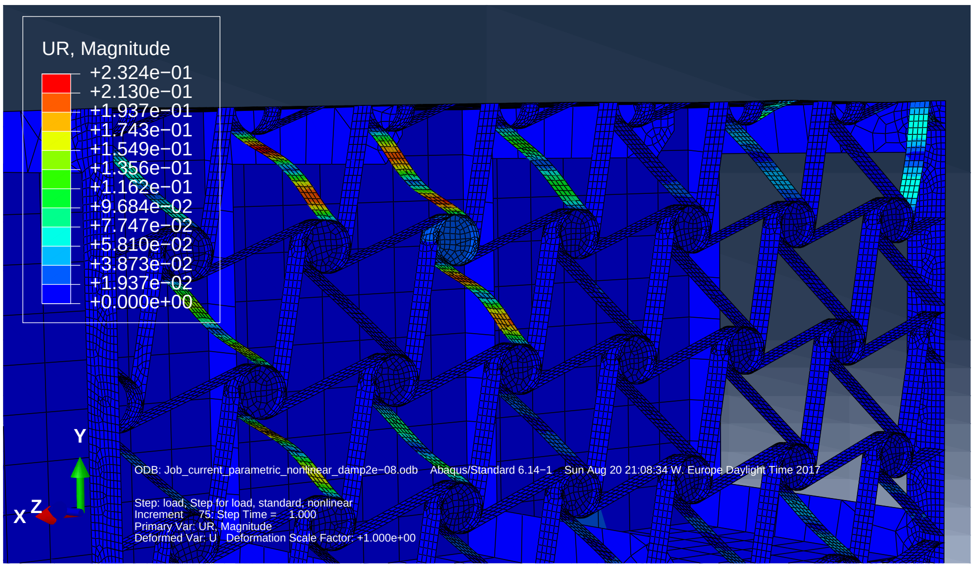

Figure 5.25: Model response when the fraction of load applied equals to 100% of the prescribed load (700 N) and $r_{\mathrm{chi}} = 17.5$ mm. Here, the excessive value of the chiral node radius r_{chi} makes that the buckled region is moved towards increasing values of x.

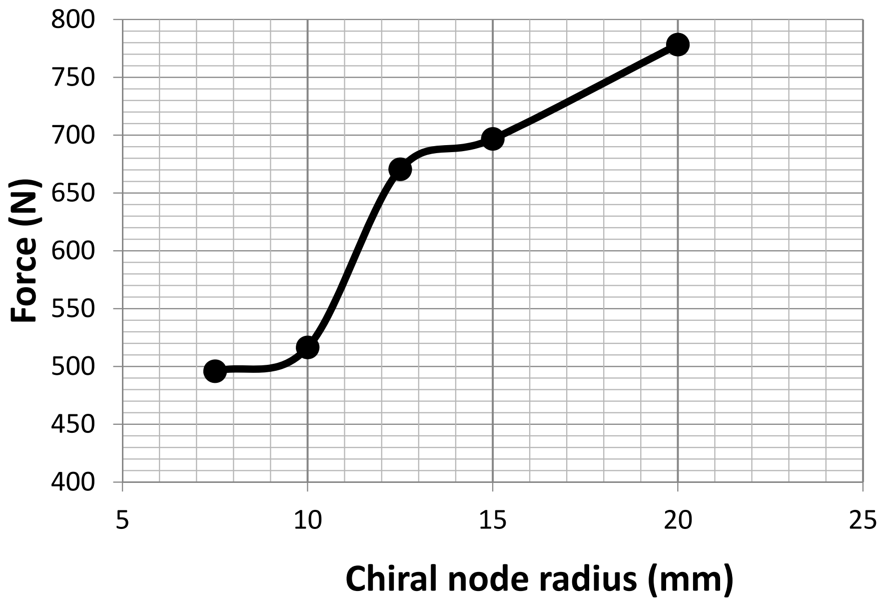

Figure 5.26: Force that induces the structure to collapse as a function of the chiral node radius r_{chi}.

Chiral ligament half length L_{chi}

The numeric results obtained for the parametric study on the chiral ligament half length L_{chi} are shown in Table **??**. The geometrical meaning of this parameter can be seen in the sketch shown in Figure **??**. The displacement-force curve for the set of values analysed is shown in Figure **??**. This plot shows that the bigger the ligament half length is, the earlier that the structure will collapse after severe buckling of the ligaments at the root. For the case of $L_{\text{chi}} = 30$, the structure does not collapse as the structure has become very stiff.

Again, in a further step, the force that causes the structure to collapse for a given value of the half length L_{chi} parameter was investigated. The resulting plot is shown in Figure **??**.

L_{chi}	ϕ_{tip} (deg)	$e(\phi_{\text{tip}})(\%)$	$\tilde{\phi}_{\text{tip}}$ (deg)	$e(\tilde{\phi}_{\text{tip}})(\%)$	v_{max}	$\hat{z}_{v_{\text{max}}}$	$\hat{x}_{v_{\text{max}}}$
30	-0.181	13.106	-0.131	-8.951	-1.101	1	0.602
50	-1.596	14.222	-0.203	-18.444	-14.267	1	0.334
70	-3.252	13.574	-0.204	-8.297	-24.022	1	0.463

Table 5.7: Results from parametric study on chiral ligament half length r_{chi}. The results show the mean twist at the tip of the wing-box for the Abaqus nonlinear simulation ϕ_{tip} and for the linear simulation $\tilde{\phi}_{\text{tip}}$. The maximum relative error of the mean calculation, expressed as percentage, for these two magnitudes is $e(\phi_{\text{tip}})$ and $e(\tilde{\phi}_{\text{tip}})$, respectively. The table also shows the maximum vertical displacement v_{max} among all the mesh nodes located on the upper skin of the wing-box and the dimensionless position in the spanwise direction $\hat{x}_{v_{\text{max}}}$ and in the chordwise direction $\hat{z}_{v_{\text{max}}}$ of the node that shows $v = v_{\text{max}}$.

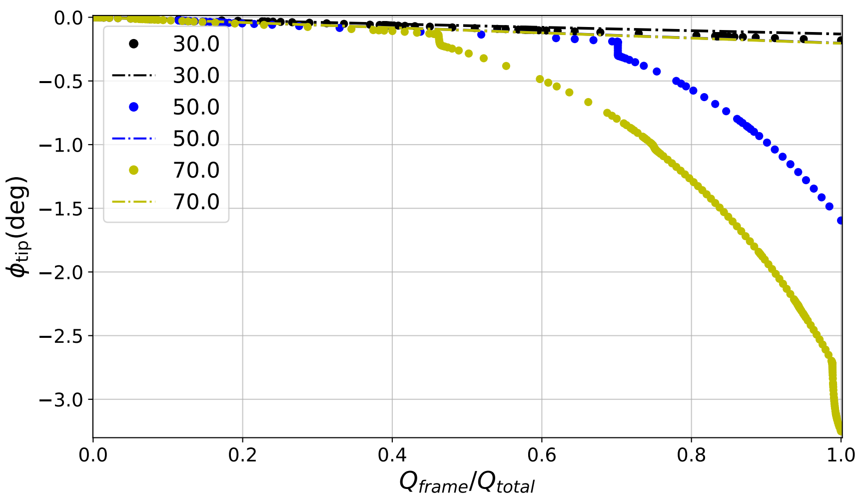

Figure 5.27: Displacement-force curve for various values of the chiral ligament half length L_{chi}. The bigger the ligament half length is, the earlier that the structure will collapse after severe buckling of the ligaments at the root.

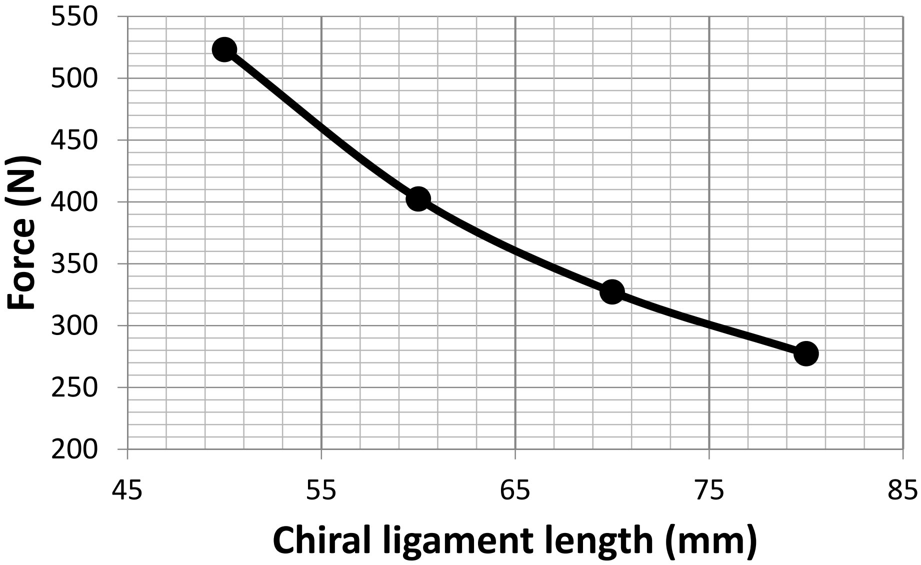

Figure 5.28: Force that induces the structure to collapse as a function of the chiral ligament half length L_{chi}.

Chiral structure thickness t_{chi}

The results for the parametric study performed on the chiral structure thickness t_{chi} are shown in Table **??**. This parameter represents the wall thickness assigned to all the shell elements that form the lattice part, shown in Figure **??**. The displacement-force curve is shown in Figure **??**. Here it can be seen that a thicker chiral structure delays the structure collapse. Similarly as it occurred for the chiral node depth B_{chi}, the more bigger the thickness t_{chi} is, the more abrupt is the decrement in tip twist is.

Finally, the required force to induce the structure to collapse was plot against the corresponding value of the chiral structure thickness t_{chi}, resulting on the curve shown in Figure **??**.

t_{chi}	ϕ_{tip} (deg)	$e(\phi_{\text{tip}})(\%)$	$\tilde{\phi}_{\text{tip}}$ (deg)	$e(\tilde{\phi}_{\text{tip}})(\%)$	v_{max}	$\hat{z}_{v_{\text{max}}}$	$\hat{x}_{v_{\text{max}}}$
0.2	-1.413	11.363	-0.233	-15.24	-10.646	1	0.546
0.4	-1.331	11.406	-0.206	-15.187	-12.654	1	0.334
0.6	-0.699	14.276	-0.193	-18.502	-7.311	1	0.546
0.8	-0.186	6.856	-0.125	-12.046	-2.039	1	0.546

Table 5.8: Results from parametric study on chiral structure thickness t_{chi}. The results show the mean twist at the tip of the wing-box for the Abaqus nonlinear simulation ϕ_{tip} and for the linear simulation $\tilde{\phi}_{\text{tip}}$. The maximum relative error of the mean calculation, expressed as percentage, for these two magnitudes is $e(\phi_{\text{tip}})$ and $e(\tilde{\phi}_{\text{tip}})$, respectively. The table also shows the maximum vertical displacement v_{max} among all the mesh nodes located on the upper skin of the wing-box and the dimensionless position in the spanwise direction $\hat{x}_{v_{\text{max}}}$ and in the chordwise direction $\hat{z}_{v_{\text{max}}}$ of the node that shows $v = v_{\text{max}}$.

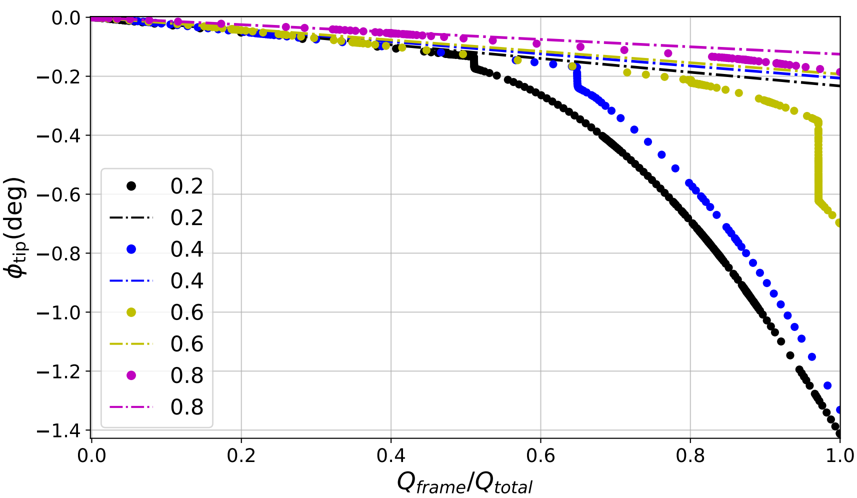

Figure 5.29: Displacement-force curve for various values of the chiral structure thickness t_{chi}. The bigger the ligament half length is, the earlier that the structure will collapse after severe buckling of the ligaments at the root.

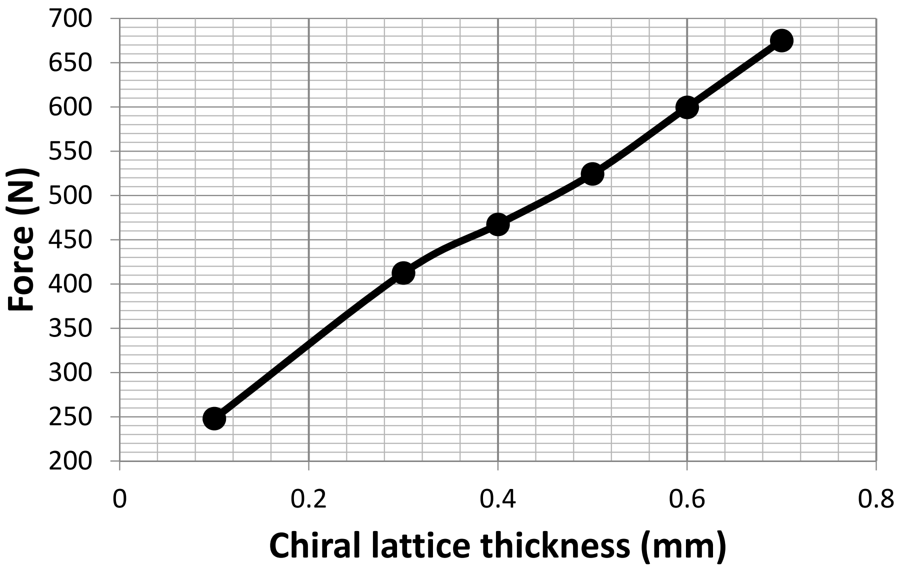

Figure 5.30: Force that induces the structure to collapse as a function of the chiral structure thickness t_{chi}.

Chapter 6

Conclusion and Outlook

This thesis presents a novel passive mechanism of wing twist morphing achieved through the control of the bending-twist coupling of the wing-box. The system incorporates a variable-stiffness spar in the wing-box that comprises a lattice of chiral elements. In the ligaments of these elements, elastic instabilities are intentionally induced and thus the effective shear modulus of the adaptive spar is modified. This adaptation provokes the wing-box section shear centre shifting and the consequent modification in wing-box torsional stiffness. This, ultimately induces a twist deformation in wing-box that has been passively activated exploiting local elastic instabilities.

An analytical model of the wing-box is developed using an ideal beam configuration with variable shear modulus in one of the webs. The effect of variations of this magnitude on the torsional stiffness, the flexural stiffness, the shear centre position and the bending and twisting deformations of the wing-box are studied. Also, the effect of variations of the geometry in these magnitudes is analysed. Results anticipate that, once th buckling-induced reduction in shear modulus in the spar is activated, the reduction in flexural stiffness for the wing-box is negligible compared with the reduction in torsional stiffness.

A computational model of the whole assembly is built next. It is designed in a fully parameterized format using Python scripting. This model is constituted of a wing-box in C-profile, a lattice of chiral elements and a tunable number of ribs that provide additional transversal stiffness and avoid local deformations in the wing-box skin. Different design options are considered, such as variations in the geometry, the load, the mesh and the number of ribs. An analysis of this model is performed in order to obtain a baseline configuration to posteriorly execute parametric studies. One of the aspects considered is this analysis is the modeling of the lattice nodes rigid body behavior. Results shows that the best modeling approach is to add an additional rigid part to provide supplementary stiffness. The addition of ribs in the middle of wing-box length is considered necessary to provide additional stiffness in the transversal direction and avoid undesired local deformations in the wing-box skin. Another consideration is the appearance of sources of instabilities such as buckling that require the inclusion of artificial damping factor into the simulation.

Nonlinear simulations are carried out using this model and incorporating artificial dissipation through constant damping factor. Special attention needs to be taken so that the inclusion of artificial damping factor is not leading to inaccurate results due to over-damping of the structure. The onset of the buckling phenomena and its evolution in the chiral lattice is characterized next. Results show that the collapse of the structure occurs when severe buckling appears on the ligaments of the chiral elements located at the root of the wing-box. This event produces a sudden reduction on the torsional stiffness of the structure and an increase in the twist deformation observed at the wing-box tip. A second and more generalized buckling in the chiral lattice is observed to origin a second modification of the torsional stiffness for certain cases. For the baseline configuration of the model, the twist morphing of the wing-box is obtained to be equal to -1.25 degrees for the nonlinear simulation while the predicted twist for the linear simulation is -0.19 degrees.

Furthermore, a parametric study is performed on the computational model. Results show that considerable tailorability can be achieved through modifications of selected parameters. The parameter that shows to have a bigger influence in the onset and evolution of the elastic instabilities is the wing-box thickness. Increasing the wing-box thickness by 0.1 mm, provokes that the required force to induce the appearance of buckling at the root increases by 100 N.

In further studies of this technology, it would be necessary to numerically analyse the system response for more realistic aerodynamic loads and also manufacture a demonstrator that could be used to experimentally test the feasibility of the proposed concept. The analysis of the time-bounded response of this mechanism is beyond the scope of this preliminary work, but such a investigation would be a crucial prior implementation of the system on a real lift generating structure.

The proposed morphing has been shown to be capable of inducing global twist morphing of a wing-box exploiting local elastic instabilities. It has shown to be promising to be applied on realistic wing structures for which the torsional response is dominated by the wing-box. Possible applications may include load alleviation purposes on structures with high aspect ratio.

Appendix A

Python code generated

All the code code generated for this project can be downloaded from the following Github repository: `https://github.com/AlejandroValverde/abaqus.git`.